Thermal characterisation of miniature hotplates used in gas sensing technology

Prakash Pandey

A thesis submitted to

De Montfort University

For the degree of

Doctor of Philosophy

Faculty of Computing, Engineering and Media

Electronic Engineering

De Montfort University

Leicester, UK

January 2020

Dedication:

I would like to dedicate this work in memory of my beloved late mother ***Mrs. Tara Devi Pandey*** *who sacrificed own happiness for my success but sadly she could not be there when it is happening!!!*

Acknowledgements:

This project would not have been possible without the help and support of others. I must start by thanking my primary supervisor, **Dr. Chris Oxley**, for all of his support, guidance and enormous encouragement. I am deeply indebted to him for the continual invaluable guidance and for reviewing my thesis even after his retirement.

I would also like to express my deepest gratitude to my supervisor, **Professor Alistair Duffy**, for his persistent support and encouragement. I am deeply indebted to him for proofreading the draft of my thesis. His suggestions and criticism were most helpful. I am also grateful to **Dr. Richard Cross** for his secondary supervision work. His wise advice and constructive criticism during the work helped me to develop life-long research skills. I am also thankful to **Dr. James Glover** for his help and continued encouragement.

I would also like to thank ams sensors Ltd. Cambridge, UK, for the supply of the miniature IR micro-emitters, especially **Dr. Richard H. Hopper** and **Dr. Syed Zeeshan Ali** for their support during the period of this research work.

My sincere appreciation also goes to Manbir Sambhi, Ashok Karavadra, and Prakash Patel for their technical and equipment assistance.

I am very grateful to the faculty of computing, engineering and media of the De Montfort University for their financial support.

At last but not least, I deeply thank to my beautiful family and friends for their continued support throughout my studies, and in particular my father, **Krishna Prasad Pandey**, who provided much needed love and support. This work would not have been possible without the incredible support and patience of my wife **Mrs. Mamata Khanal Pandey**, a special thanks to her. I would like also to remember my sister **Pabitra Pandey** for her love and always being there to support and encourage me.

Abstract:

The reliability of micro-electronic devices depends on the device operating temperature and therefore self-heating can have an adverse effect on the performance and reliability of these devices. Hence, thermal measurement is crucial including accurate maximum operating temperature measurements to ensure optimum reliability and good electrical performance. In the research presented in this thesis, the high temperature thermal characterisation of novel micro-electro-mechanical systems (MEMS) infra-red (IR) emitter chips for use in gas sensing technology for stable long-term operation were studied, using both IR and a novel thermo-incandescence microscopy.

The IR emitters were fabricated using complementary-metal-oxide semiconductor (CMOS) based processing technology and consisted of a miniature micro-heater, fabricated using tungsten metallisation. There is a commercial drive to include MEMS micro-heaters in portable electronic applications including gas sensors and miniaturised IR spectrometers where low power consumption is required.

IR thermal microscopy was used to thermally characterise these miniature MEMS micro-heaters to temperatures approaching 700 °C. The research work has also enabled further development of novel thermal measurement techniques, using carbon microparticle infra-red sensors (MPIRS) with the IR thermal microscopy. These microparticle sensors, for the first time, have been used to make more accurate high temperature (approaching 700 °C) spot measurements on the IR transparent semiconductor membrane of the micro-heater.

To substantially extend the temperature measurement range of the IR thermal microscope, and to obtain the thermal profiles at elevated temperatures (> 700 °C), a novel thermal measurement approach has been developed by calibrating emitted incandescence radiation in the optical region as a function of temperature. The calibration was carried out using the known melting point (MP) of metal microparticles. The method has been utilised to obtain the high temperature thermo-optical characterisation of the MEMS micro-heaters to temperatures in excess of 1200 °C. The measured temperature results using thermo-incandescence microscopy were compared with calculated electrical temperature results. The results indicated the thermo-incandescence measurements are in reasonable agreement (± 3.5 %) with the electrical temperature approach. Thus, the measurement technique using optical incandescent radiation extends the range of conventional IR microscopy and shows a great potential for making very high temperature spot measurements on electronic devices.

The high power (> 500mW) electrical characterisation of the MEMS micro-heaters were also analysed to assess the reliability. The electrical performance results on the MEMS micro-heaters indicated failures at temperatures greater than 1300 °C and Scanning Electron Microscope (SEM) was used to analyse the failure modes.

Nomenclature

ε	Surface emissivity
μ	Microns
λ	Wavelength
Φ	Thermal impedance
ρ	Resistivity
σ	Stefan – Boltzmann constant
°C	Degree Celsius
c	Speed of light in vacuum
C_{TR}	Thermo-reflectance coefficient
h	Plank's constant
I	Current
K	Kelvin
k_B	Boltzmann's constant
q	Charge of an electron
R_0	Level of background IR radiation
R_b	Emitted IR radiation by an ideal black body
R_p	Emitted IR radiation by a carbon microparticle
R_s	Emitted IR radiation
T	Temperature
V	Voltage

Material abbreviations

Ag	Silver
Al	Aluminium
AlGaN	Aluminium gallium nitride
Au	Gold
CH_4	Methane
CO	Carbon monoxide
CO_2	Carbon dioxide
Cr_2O_3	Chromium oxide
Cu	Copper
GaAs	Gallium arsenide
GaN	Gallium nitride
Ge	Germanium
H_2S	Hydrogen sulphide
InSb	Indium antimony
KOH	Potassium hydroxide
Mn	Manganese
Mn_3O_4	Manganese oxide
NH_3	Ammonia
Ni	Nickel
NO_2	Nitrogen dioxide
RhB	Rhodamine B
Si	Silicon
SiC	Silicon carbide
SiGe	Silicon germanium
Si_3N_4	Silicon nitride

SiO_2	Silicon dioxide
SnO_2	Tin dioxide
SO_2	Sulphur dioxide
TiN	Titanium nitride
WO_3	Tungsten oxide
ZnO	Zinc oxide

Key acronyms

2D	Two dimensional
AFM	Atomic force microscopy
CMOS	Complementary-metal-oxide-semiconductor
CNTs	Carbon nanotubes
CW	Continuous wave
DC	Direct current
DRIE	Deep reactive-ion etching
DUT	Device under test
FET	Field-effect-transistor
HBT	Hetero-structures bipolar transistor
HEMT	High electron mobility transistor
HFET	Heterojunction-field-effect-transistor
IC	Integrated circuit
IGBT	Insulated gate bipolar transistor
IR	Infra-red
IV	Current-voltage
LED	Light emitting diode

LEL	Lower explosive limit
MEMS	Micro-Electro-Mechanical Systems
MMIC	Monolithic microwave integrated circuit
MOSFET	Metal-oxide-semiconductor field effect transistor
MP	Melting point
MPIRS	Microparticle infra-red sensor
NDIR	Non-dispersive infra-red
RF	Radio frequency
RFICs	Radio frequency integrated circuits
RTIL	Room temperature ionic liquid
SEM	Scanning electron microscope
TSP	Temperature-sensitive-parameter
UV	Ultraviolet
VOCs	Volatile organic compounds
QCM	Quartz crystal microbalance
QFI	Quantum Focus Instruments

Table of Contents

Table of Figures

Chapter 1

Introduction:

1.1. Background and motivation:

Gas sensors are significantly important in different fields of advanced technology including scientific, environmental and industrial safety, medical, commercial and domestic applications [1], [2]. Over the past few decades, the need for reliable low cost, low power gas sensors is increasing, and with the emerging trend in miniaturisation, various possibilities are expected for gas sensors, for example, integration into automobiles, mobile devices and other battery operated electronic medical devices [3]. Micro-electro-mechanical systems (MEMS) technology is key to meeting these requirements with the design and fabrication of such miniaturised integrated modern sensors. One of the key components of a modern gas sensor is the MEMS micro-heater, which is required to heat the sensing material (e.g., metal oxides, polymers etc.) for better sensitivity, selectivity and fast response/recovery time. Additionally, MEMS micro-heaters can also be used as an IR source in a non-dispersive (NDIR) gas sensors. Thus, thermal analysis including thermal uniformity and accurate peak operating temperature of the MEMS micro-heater is important to ensure reliable operation of the gas sensors [4]. This thesis reports on the thermal characterisation of novel MEMS micro-heaters [5], based on tungsten metallisation, which can also be used as a mid and near field infra-red (IR) source [6], [7].

In recent years, miniature mid and short wave IR emitters are of interest, for use in NDIR gas sensing and spectroscopy applications [8]. At present many of these applications use a glass micro-bulb as a broadband IR source. The micro-bulb manufacturing costs are low but it suffers from a number of disadvantages, which include; high DC power consumption (typically several 100mW) [6], large form factor compared to most silicon based IR sources, slow transient response time and limited emission in the mid to long IR wavelengths due to optical absorption by the glass envelope. Different methods have been used for the fabrication of miniature silicon based IR sources [9], [10], many based on propriety MEMS processing technologies. The complementary-metal-oxide-semiconductor (CMOS) based IR source, studied in this work, is based on tungsten metallisation technology, which can be heated to high operating temperatures [11]. Tungsten has been used as an interconnect metal because of its high melting point (> 3400 °C) and resistant to electromigration induced failure, when compared to aluminium or poly-silicon [12]. The use of tungsten enables the design and fabrication of an IR thermal source with long-term stability, having all the advantages of CMOS technology including low manufacturing cost, excellent device reproducibility, and the possibility of integration with a wide range of electronic circuitry. The device typically operates at temperatures around 500 °C [11] to thermally generate optical emission for mid-IR spectroscopy applications, including optical gas sensing [6]. A future requirement is to operate the CMOS based IR source at higher operating temperatures (> 800 °C) for spectral sensing applications in the short-wave region of the IR spectrum (1.4 µm – 2.5 µm) where many molecules have absorption lines [7], [13]. A chip scale source has the advantage of a smaller

physical envelope, compared to the micro-bulb based IR source, and can also be assembled in a surface mount package.

It is important to maximise thermal uniformity across the micro-heater to ensure consistent IR emission and to minimise the localised hotspots, which could induce thermal stress leading to premature failure. There are several thermal characterisation techniques that can be used to thermally profile micro-scale semiconductor devices [14]. Optical methods have been widely used to characterise the thermal behaviour of micro-electronic devices, because of their major benefits of being non-contact and non-invasive. In addition, optical method can be used to image different regions enabling the identification of hot areas within a device [15].

IR thermal microscopy is an established optical technique and has been extensively used in this work to thermally characterise the temperature distribution across the IR source [5], which showed excellent thermal uniformity for temperatures approaching 700 °C. To enable thermal characterisation of the IR source, at elevated temperature (> 700 °C), a passive optical approach is presented in which, uniform thermally emitted incandescent radiation is used. The development of high temperature measurements using the combination of IR and thermo-incandescence microscopy will enable other high operating temperature micro-electronic devices to be explored.

1.2. Outline of the work:

Self-heating in RF and microwave based micro-electronic devices can adversely affect the RF performance (power and frequency), and if the operating temperature becomes sufficiently high, may result in complete device failure. The focus of the research presented in this thesis was to investigate the high temperature thermal characterisation of CMOS compatible miniature infra-red emitters for stable long-term operation, for use in gas sensing technology. A review of different thermal characterisation techniques to thermally profile micro-scale semiconductor electronic devices was undertaken resulting in the use of IR thermal microscopy to study the thermal performance of novel IR emitter chips. The method utilises naturally emitted IR radiation from the device under test (DUT), resulting in a real-time two-dimensional (2D) thermal images. The accuracy of temperature measurements using IR thermal microscopy is dependent on the accurate determination of the surface emissivity of the device being measured. It is challenging to accurately measure the surface emissivity of optically transparent semiconductor materials, which allow IR radiation from underlying layers to be collected by the microscope. To overcome some of the limitations, a novel IR thermal point measurement using a carbon based microparticle sensor technology has been developed at DMU [16]. Work was undertaken to further improve the microparticle measurement technique which included a more effective and reliable micro-manipulation of the microparticle sensor. In addition, the effect of the microparticle diameter on the temperature measurement has also been investigated. The revised technique was used to make improved high temperature measurements on the miniature IR emitter chip to temperatures of approximately 700 °C.

To obtain further improvements to temperature uniformity and operation at higher temperatures the IR thermal emitter chip was re-designed to have a higher surface emissivity by ams Sensors Cambridge, Ltd. The chip was fabricated in ams Sensors facilities. IR microscopy was used to characterise the thermal behaviour of these improved design IR

emitters. Preliminary thermal measurements were also made on the IR emitters using a thermo-reflectance technique at Quantum Focus Instruments (QFI) Bristol (UK), facility to compare with IR temperature measurement results. The thermo-reflectance measurements was not practical on these devices due to the challenges posed by multiple internal reflections and small mechanical fluctuation of the thin heater membrane.

A novel thermal measurement approach based on thermo-incandescence microscopy was developed in this research work which enabled thermo-optical characterisation of these IR thermal emitters to temperature in excess of 1200 °C. As the technique is optical, it also has the potential of identifying hotspots, similar to IR microscopy. The measurement technique could also be used to perform high temperature measurements on other micro-scale electronic devices.

1.3. Thesis outline:

The research work has been divided into eight chapters and the summary of each chapter is given below:

Chapter-1: The chapter describes the research motivation, background to the CMOS based IR sources and outlines the work undertaken. The chapter also highlights the novelty in this research work.

Chapter-2: The chapter describes the different types of available thermal measurement techniques for performing the temperature measurements on micro-electronic devices and undertakes a review of them.

Chapter-3: The conventional IR thermal measurement technique is described in detail and critical analysis of methods used in this research, which includes instrumentation and experimental design and setup.

Chapter-4: The chapter provides a detailed description of the IR thermal measurements, using the microparticle infra-red sensor (MPIRS) technology, which can be used to obtain an improved accuracy of IR temperature measurements made on low emissivity/ highly reflective, and uncoated semiconductor devices. The radiance calibration as a function of temperature and the effect of the background surface radiation on the emissivity measurement of the MPIRS is discussed. In addition, a reliable micro-manipulation method to pick individual microparticles and place onto the surface of the DUT is discussed.

Chapter-5: The chapter provides an overview of gas sensor technology including the MEMS micro-heater technology sensors, gasses which can be detected, the principle of operation and applications.

Chapter-6: The chapter reports the work undertaken to assess the electrical and thermal performance of the MEMS micro-heaters used in IR emitter chips, based on CMOS technology. These include IV characterisation and analysis of thermal uniformity across the micro-heater structure using conventional IR thermal microscopy. The thermal characterisation of the micro-heater is also described using electrical, and for the first time, using the MPIRS technology to

temperatures approaching 700 °C. The chapter also includes the temperature measurement results made on the improved design IR emitters using IR thermal microscopy and comparison with electrical temperature results.

Chapter-7: The chapter describes the development of a high temperature thermal measurement approach based on thermo-incandescence microscopy, which can be integrated with IR microscope. To calibrate the emitted incandescent radiation with temperature a novel approach using metal microparticles with a known melting point was developed. To the author's knowledge the temperature measurement method is novel and enables the thermal characterisation of the MEMS micro-heaters to temperatures in excess of 1200 °C.

Chapter-8: The chapter concludes the main findings from this research work, and also describes future work.

1.4. Novelty in the research work:

The areas of novelty reported in this research work are listed below:

- Improvements to the novel carbon MPIRS thermal measurement technique which was first developed at De Montfort University [16]. These include showing that the MPIRS with more than >10μm in diameter will provide a more accurate temperature measurement (note there may have to be a compromise to the thermal spatial resolution). The work also suggests the microparticle sensor would be best adopted for making temperature measurements on materials with very low surface emissivity, for example gold, where the background surface radiation is very low. To make temperature measurements utilising the MPIRS technique on IR transparent semiconductor materials (for example GaAs), the real surface emissivity of the MPIRS needs to be measured independent of the DUT and must be higher than the DUT.

- The use of the MPIRS, for the first time, utilising IR thermal microscopy for measuring the thermal profiles of the MEMS based IR micro-emitters to temperatures approaching 700 °C [5]. The MPIRS technique was also used, for the first time, for measuring the improved thermal profiles on the semi-packaged MEMS micro heater of an IR emitter chip.

- The development of a novel thermal measurement technique which was based on measuring the emitted optical incandescent radiation as a function of operating temperature. The high temperature thermal performance of MEMS micro-heaters based on tungsten CMOS technology, have been measured for the first time using a combination of IR and optical incandescence thermography to temperatures in excess of 1200 °C. The high power electrical performance of the MEMS micro-heater was analysed and the reliability of the chip at the high temperatures was assessed.

1.5. List of publications:

1. **P. Pandey,** C. Oxley, R. Hopper, Z. Ali, and A. Duffy, “Infra-red thermal measurement on a low-power infra-red emitter in CMOS technology,” *IET Science, Measurement & Technology*, vol. 13, no. 1, pp. 25–28, Aug. 2018, doi: 10.1049/iet-smt.2018.5427.

2. **P. Pandey,** C. Oxley, R. H. Hopper, F. Udrea, and S. Z. Ali, “High temperature characterization of a CMOS based infra-red source using thermal-incandescence microscopy,” *Solid-State Electron.*, vol. 166, p. 107773, Apr. 2020, doi: 10.1016/j.sse.2020.107773.

3. Y. Dai, S.Z. Ali, R. Hopper, C. Falco, **P. Pandey**, C. Oxley, D. Popa and F. Udrea, “Crosstalk Analysis of a CMOS Single Membrane Thermopile Detector Array,” *Sensors*, vol. 20, no. 9, p. 2573, Apr. 2020, doi: 10.3390/s20092573.

1.6. References:

[1] D. Popa and F. Udrea, "Towards Integrated Mid-Infrared Gas Sensors," *Sensors*, vol. 19, no. 9, p. 2076, Jan. 2019, doi: 10.3390/s19092076.

[2] A. Mirzaei, S. S. Kim, and H. W. Kim, "Resistance-based H2S gas sensors using metal oxide nanostructures: A review of recent advances," *Journal of Hazardous Materials*, vol. 357, pp. 314–331, Sep. 2018, doi: 10.1016/j.jhazmat.2018.06.015.

[3] M. Deluca *et al.*, "In-Situ Temperature Measurement on CMOS Integrated Micro-Hotplates for Gas Sensing Devices," *Sensors*, vol. 19, no. 3, p. 672, Jan. 2019, doi: 10.3390/s19030672.

[4] V. Balasubramanian, V. S. Selvakumar, L. Sujatha, M. Revathi, and C. V. Gayathri, "Electro Thermal Effects of Geometrically Modified MEMS-Based Micro Heater for Gas Sensing Applications," *American Scientific Publishers*, vol. 17, no. 9, pp. 725–732, Sep. 2019, doi: info:doi/10.1166/sl.2019.4141.

[5] P. Pandey, C. Oxley, R. Hopper, Z. Ali, and A. Duffy, "Infra-red thermal measurement on a low-power infra-red emitter in CMOS technology," *IET Science, Measurement & Technology*, vol. 13, no. 1, pp. 25–28, Aug. 2018, doi: 10.1049/iet-smt.2018.5427.

[6] S. Z. Ali, A. D. Luca, R. Hopper, S. Boual, J. Gardner, and F. Udrea, "A Low-Power, Low-Cost Infra-Red Emitter in CMOS Technology," *IEEE Sensors Journal*, vol. 15, no. 12, pp. 6775–6782, Dec. 2015, doi: 10.1109/JSEN.2015.2464693.

[7] M. Yu, Y. Okawachi, A. G. Griffith, N. Picqué, M. Lipson, and A. L. Gaeta, "Silicon-chip-based mid-infrared dual-comb spectroscopy," *Nature Communications*, vol. 9, no. 1, p. 1869, May 2018, doi: 10.1038/s41467-018-04350-1.

[8] R. Hopper *et al.*, "A CMOS-MEMS Thermopile with an Integrated Temperature Sensing Diode for Mid-IR Thermometry," *Procedia Engineering*, vol. 87, pp. 1127–1130, Jan. 2014, doi: 10.1016/j.proeng.2014.11.363.

[9] D. Bauer, M. Heeger, M. Gebhard, and W. Benecke, "Design and fabrication of a thermal infrared emitter," *Sensors and Actuators A: Physical*, vol. 55, no. 1, pp. 57–63, Jul. 1996, doi: 10.1016/S0924-4247(96)01250-2.

[10] M. Weber, P. Lerch, and P. Renaud, "Improved design for fast modulating IR sources," *J. Micromech. Microeng.*, vol. 7, no. 3, p. 210, 1997, doi: 10.1088/0960-1317/7/3/034.

[11] S. Z. Ali, F. Udrea, W. I. Milne, and J. W. Gardner, "Tungsten-Based SOI Microhotplates for Smart Gas Sensors," *Journal of Microelectromechanical Systems*, vol. 17, no. 6, pp. 1408–1417, Dec. 2008, doi: 10.1109/JMEMS.2008.2007228.

[12] A. D. Luca, S. Z. Ali, and F. Udrea, "On the reproducibility of CMOS plasmonic mid-IR thermal emitters," in *2017 International Semiconductor Conference (CAS)*, 2017, pp. 101–104, doi: 10.1109/SMICND.2017.8101168.

[13] I. E. Gordon *et al.*, "The HITRAN2016 molecular spectroscopic database," *Journal of Quantitative Spectroscopy and Radiative Transfer*, vol. 203, pp. 3–69, Dec. 2017, doi: 10.1016/j.jqsrt.2017.06.038.

[14] D. Pierścińska, "Thermoreflectance spectroscopy—Analysis of thermal processes in semiconductor lasers," *Journal of Physics D: Applied Physics*, vol. 51, no. 1, p. 013001, Jan. 2018, doi: 10.1088/1361-6463/aa9812.

[15] C. H. Oxley, R. H. Hopper, G. Hill, and G. A. Evans, "Improved infrared (IR) microscope measurements and theory for the micro-electronics industry," *Solid-State Electronics*, vol. 54, no. 1, pp. 63–66, Jan. 2010, doi: 10.1016/j.sse.2009.09.022.

[16] R. H. Hopper, I. Haneef, S. Z. Ali, F. Udrea, and C. H. Oxley, "Use of carbon micro-particles for improved infrared temperature measurement of CMOS MEMS devices," *Measurement, Science and Technology*, vol. 21, no. 4, p. 045107, Mar. 2010, doi:10.1088/0957-0233/21/4/045107

Chapter 2

A review of temperature measurement techniques:

2.1. Introduction:

Thermal measurement techniques have been developed over many years to measure the operating temperature of electronic devices [1]. The operating temperature has significant consequences on the overall performance and reliability of electronic devices [2]. For example, the maximum operating frequency or speed of a microprocessor usually decreases when the operating temperature increases [3]. Similarly, the current gain cut-off frequency or transconductance of field effect transistors (FET), for example, aluminium gallium nitride (AlGaN/GaN) HEMTs decreases with an increase in operating temperature [4]. Thermal simulation models [5] can be used to predict electronic device operating temperatures, but it is often difficult to compute them accurately because of uncertainty of the thermal properties of complex semiconductors layers [6]. Therefore, highly specialised experimental temperature measurement techniques are required to help understand the overall thermal performance of a particular device type.

There has been the development of a wide range of techniques for measuring the operating temperature of electronic devices. The thermal measurement techniques can be broadly categorised into two classifications; (1) contact methods and (2) non-contact methods [3], [7]. In the contact methods, a temperature measuring sensor, is in direct physical contact with the device and is used to monitor the temperature of the device. Electric thermocouples and Atomic Force Microscopy (AFM) are some of the common examples of contact temperature measurement techniques. The non-contact thermal measurement techniques depend on the device's electrical or optical properties, which change with temperature and are monitored to use as a thermometer. A review of the measurement methods for measuring the temperature performance of electronic devices and their respective advantages and weakness will be fully discussed in this chapter.

2.2. Contact thermal measurement techniques:

Temperature measurement depends on the transfer of heat energy from the surface of device under test (DUT) to an object which acts as temperature sensor, for example, mercury or alcohol based thermometers as used in a domestic applications. Temperature sensitive liquid crystals and thermocouple probes are also included in this category. In this method the temperature of a material or sensor which is in thermal contact with the DUT is monitored. A single point or a 2D matrix of thermal measurements is possible with this temperature measurement technique, by moving the point contact in the X and Y directions. For example: thermocouples can be used to take a reading of a single point temperature or to create a matrix of temperature measurements, and atomic force microscopy (AFM) can be used to scan a thermal probe across the surface of the DUT to create a 2D thermal map [8], [9]. In the physical contact method, spatial resolution is limited by the physical size of the contacting probe, for example, the contact size of the thermocouple, or AFM probe diameter [3]. A resolution of ~50nm has been demonstrated for scanning AFM thermal probes [10], [11]. The benefit of

contact methods is the potential for high resolution (however, care must be taken in interpreting the results because of the loading effect of the measurement method as heat is always lost to the measurement probe, thereby reducing thermal spatial resolution). Further limitations include the surface of the DUT must be available for physical contacts and the temperature response relies on the thermal response of the contacting probe [3]. Some of the physical contacting methods for temperature measurement are described below:

2.2.1. Liquid crystals:

Liquid crystals are identified as organic compounds with a known temperature dependent phase between two states, solid and an isotropic liquid. In this method, the transition temperature is used as temperature-sensing parameter [3]. The transition temperature is defined as the temperature point at which a phase transformation of liquid crystals occurs from an aligned state to a random state. The incident light scatters selectively by wavelength in liquid crystal, with the selectivity being temperature dependant [12].

Although the technique offers a high accuracy with temperature resolutions approaching 0.1 °C [13], the disadvantage include, with each type of liquid crystal only one transition temperature point can be established. Liquid crystals are available to measure the temperatures from 30 °C to 120 °C [3]. A spatial resolution of ~1µm has been demonstrated [3]. The liquid crystals technique has been used to make temperature measurements on light emitting diodes (LEDs) [14] and AlGaN/GaN heterojunction-field-effect-transistors (HFETs) [15].

2.2.2. Thermocouples:

The thermocouple is a simple and widely used electrical sensor for measuring temperature. It consists of two different metals combined together to form a point junction. A temperature dependant voltage will be generated at the junction when heated as a result of the thermoelectric effect, and the magnitude of this voltage can be calibrated against temperature [16]. Thermocouples can be used for measuring the temperature range between -270 °C to 3000°C (dependent on junction metals) [17]. High temperature range, low cost, robustness, rapid thermal response and no self-heating within the thermocouple junction are some of the advantages of this type of sensor [18]. Although this technique is relatively simple for measuring temperature, the limitations include, poor spatial resolution (dependent on the physical size of the junction), susceptibility to corrosion and need of good physical contact between probe and DUT. They are mainly appropriate for measuring the temperature on large size (typically several mm) electronic devices, for example, high power MOSFETs [19].

The selection of different thermocouple metal combinations is dependent on cost, availability, chemical stability, maximum and minimum working temperature and material compatibility. The most common general purpose thermocouple is the type-K (Chromel – Alumel) Nickel-alloy thermocouple [16], which can be used in an oxidizing atmosphere. These thermocouples are low cost and a wide variety of probes are available to cover –250 °C to +1100 °C temperature range, however above 800 °C, oxidation may cause drift in calibration [17], which can result in errors of several degrees during temperature measurement. They are readily commercially available but are limited to typically a spatial resolution of ~20µm with

an accuracy of ~0.1 °C [7], [20]. In recent years, a MEMS technique has been used to develop thin film thermocouples [21], [22] with very high spatial resolution (in nanoscale). They are relatively expensive to fabricate and not readily available for commercial applications.

2.2.3. Atomic force microscopy:

Atomic force microscopy (AFM) uses micro-machined (MEMS) thermal sensors that are integrated in a force sensing cantilever with a nanoscale probe tip and can be used for the thermal analysis of semiconductor devices [23].

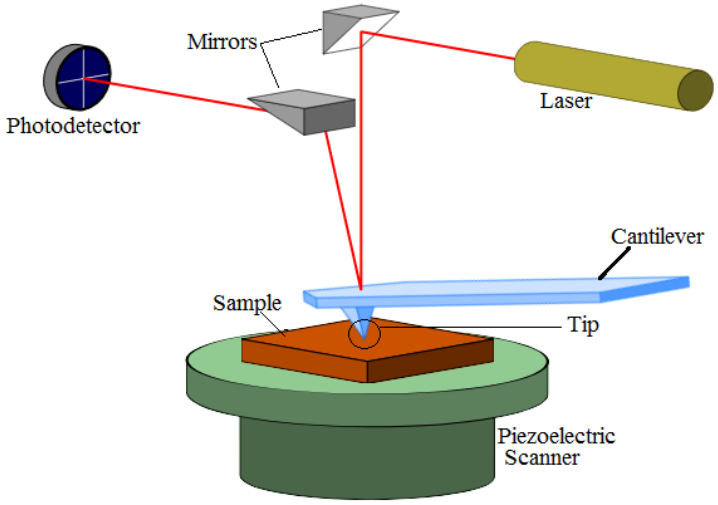

Figure 2.1: Schematic of AFM and the experimental set-up for thermal measurements [24].

This method offers potentially high spatial resolution (<1µm) with the probe-tip manufactured using nano-tubes [8] and can be used to scan the thermal profile across the surface of electronic devices. In this method, it is possible to create a matrix of temperature measurements and develop a 2D thermal map but is not in real time. The spatial resolution, unlike optical techniques (will be discussed in section **2.3.2**), is not limited by the diffraction factor. However, performance limiting factors include the diameter of thermal probe, which determines the spatial resolution, and temperature errors due to the heat transfer between surface of the DUT and the probe [25]. This technique is available for temperature measurements on electronic devices with a claimed thermal resolution of the order of 0.1 °C [20]. The temperature measurements on AlGaN/GaN HEMTs devices [26] and ultra-thin nano-sheets [27] has been made using this technique.

2.2.4. Other physically contacting techniques:

There are other physical contact techniques which are available for surface temperature measurements of semiconductor devices. For example, a thermographic phosphorous technique. This technique uses the thermal dependence of phosphor fluorescence as the temperature sensing parameter. To make the temperature measurement, the florescent material is usually deposited on a surface of DUT and the level of optical radiation emitted due to excitement from an external optical source (for example, LED or laser) as a function of temperature is measured. Advantages of this technique include a wide temperature measurement range up to 1800 °C with a temperature resolution of approximately 0.1 °C [28],

low cost and it can be used in harsh environments involving fast moving components such as jet turbine engines. However, the destructive nature of depositing the florescent material directly onto the DUT surface limits the use of this technique. Heat sensitive paints are another example of physically contacting techniques [29]. The use of non-reversible heat sensitive crystalline solid paints can be used [17] for a device which only requires an indication of the maximum operating temperatures. At a known temperature these paints melt, indicating the device surface temperature. Thermal paints are generally available for temperature measurements up to 400 °C with a temperature resolution of approximately 5 °C. The spatial resolution of this method is limited to ~ 40μm. These techniques have been used for estimating the temperatures on gas turbine blades [17].

2.3. Non-contact thermal measurement techniques:

In non-contact thermal measurement technique, no physical probe is in contact with the device surface being measured and thus avoids heat transfer which gives rise to the heat spreading problem. These techniques use either electrical or optical properties of the DUT as function of temperature. Non-contact thermal measurement techniques have been divided into the following two subcategories; (1) electrical thermal measurement techniques and (2) Optical thermal measurement techniques.

2.3.1. Electrical thermal measurement techniques:

Many electrical properties of electronic devices are a function of temperature [2], [3]. This makes it possible to utilise the temperature sensitive parameters such as the forward voltage of a PN junction; or threshold voltage [30], reverse leakage current or even device gain [3] of a transistor to monitor its average junction temperature. To make the electrical temperature measurement, the temperature sensitive parameter is initially calibrated against temperature. During calibration, the unbiased device is heated to known temperatures by a thermally controlled oven or hotplate and the temperature sensitive parameter is measured. To make the temperature measurement, the device is biased and has to be momentarily switched back into the same electrical state used to calibrate the temperature sensitive parameter. The time of switching has to be sufficiently quick to limit any reduction in the device operating temperature [7].

The electrical thermal measurement technique requires no special sample preparation because all the necessary electrical connections are available as needed for normal device operation. Thus, electrical methods are considered as a non-contact temperature measurement technique as no additional instrument is required to make physical contact with the device, all the electrical contacts required are those already needed to bias for device operation. A further advantage of this thermal measurement technique; it can be used on fully packaged devices to determine the operating temperature of the die and therefore the thermal impedance (ϕ) of the chip and package combination at different bias settings. Thermal impedance (ϕ) is defined as the maximum temperature rise divided by power dissipated in watts. However, electrical thermal measurements can only provide an average junction temperature, and will be unable to identify hot areas in the structure or the junction temperature of individual die or identify a poor die in a package containing multiple die. As shown in Figure 2.2, the average temperature

is measured for a device, where inhomogeneous thermal distribution may exist if there are physical or electrical difference between the individual die.

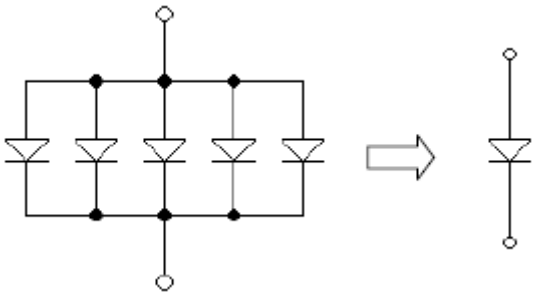

Figure 2.2: Multi-junction bipolar transistor structure looking like a single lumped element when measured using an electrical approach [19].

Some of the electrical parameters that have been used to measure the device average operating temperature are discussed below:

2.3.1.1. P-N Junction forward voltage:

Forward voltage (V_{pn}) of a P-N junction is a strong function of a temperature, and therefore can be used as a temperature-sensitive-parameter (TSP). The V_{pn} decreases with an increase in temperature due to the enhancement of thermal generation of charge carriers [30]. Therefore, the V_{pn} is possibly the most common electrical parameter used to measure the temperature of an electronic device which utilises a P-N junction [2], [31]. The IDEAL diode equation [31] shows the relationship between the current flowing through a P-N junction and temperature of the junction.

$$I_{pn} = I_s \left[\exp\left(\frac{qV_{pn}}{k_B T}\right) - 1\right] \quad \textbf{(2.1)}$$

Where,

I_{pn} is the current through the PN junction, V_{pn} is the voltage across PN junction, I_s is the reverse saturation current, k_B is Boltzmann's constant (1.381 x 10 $^{-23}$ J/K), q is charge of an electron (1.6 x 10^{-19}C) and T is junction temperature measured in Kelvin. Equation **(2.1)** can be rearranged as shown in equation **(2.2)**;

$$V_{pn} = \frac{k_B T}{q}\left[\ln\left(\frac{I_{pn}}{I_s}\right) + 1\right] \quad \textbf{(2.2)}$$

The relationship shown in equation **(2.2)** can be used to determine the junction temperature of a semiconductor device in response to power dissipation in the junction region by utilising the forward voltage drop when a small magnitude of constant forward biased current I_{pn} is applied.

Some examples where the temperature dependant forward Shockley junction voltage has been used as thermometer are; emitter-base junction of gallium arsenide hetero-junction bipolar transistors [32], [33], GaN HEMTs [34] and laser diodes [35].

2.3.1.2. Electrical resistivity:

The resistivity ρ of a semiconductor is a strong function of temperature and is given by equation **(2.3)**.

$$\rho = \frac{1}{nq\mu(T)} \qquad \textbf{(2.3)}$$

Where, n is the carrier density, q is the electronic charge of each particle and μ is the carrier mobility. The mobility of a semiconductor characterises how quickly the electrons or holes can move under the influence of an electric field. In a semiconductor device, the carrier mobility decreases due to phonon scattering with increase in temperature [36]. The carrier density is also temperature dependant but the change of mobility with temperature will dominate, and thus the resistivity of semiconductor devices increases with increasing temperature. Temperature of the AlGaN/GaN HEMT device has been measured using the temperature dependant mobility of carriers in GaN [37]. In another instance, the temperature of GaAs MESFETs [38] has been measured using the temperature dependence of the gate metal resistivity [39].

2.3.1.3. Other electrical methods:

There are number of other electrical parameters that have been used for the temperature measurements of semiconductor electronic devices. The threshold voltage (V_{th}) has been used to evaluate the temperature of the MOSFET [2], [40]. The current gain (β) of bipolar transistors is usually a strong function of temperature and this has been for the junction temperature measurements of GaAs based hetero-structures bipolar transistors (HBTs) [41] and silicon germanium (SiGe) hetero-structures [42]. The reverse saturation current increases exponentially with temperature of P-N junctions and possible to use as a TSP to measure the temperature of insulated gate bipolar transistors (IGBTs) [43].

2.3.2. Optical thermal measurement techniques:

In this technique, the optical characteristic which includes emitted (IR) or reflected radiation from a surface of DUT is used as temperature sensing parameter [19]. It is considered as a non-contact thermal measurement technique, as a probe is not required to be in physical contact with the device surface and thus avoids the heat transfer to a physical contacting probe. High spatial resolution, the ability to measure rapid variations in temperature, the ability to create quasi-real time 2D thermal maps across the surface of device are some of the potential advantages. Disadvantages include optical access to the DUT surface, which is not always practical if the device being measured is packaged, the measuring equipment required is expensive and mostly require expertise to use when compared to some physical contact methods.

Some optical techniques, for example, Raman thermal spectroscopy (Raman thermography), requires an active optical source, for example a laser pointed onto the surface of the DUT at the point for the temperature measurement. The laser source can interfere with the electrical performance of a device as well as providing some local heating at the temperature measurement point. This can be minimised by the careful choice of incident

wavelength (wavelength that is smaller than the bandgap of semiconductor being measured) and by reducing the laser power. A spatial thermal resolution approaching ~500nm [44] is possible using Raman thermography. It is scanning method, and therefore for this optical technique, 2D real time thermal images are not possible.

2.3.2.1. Infra-red (IR) thermal microscopy:

Passive optical measurement techniques use specific wavelengths of the electromagnetic spectrum, which are a function of temperature to obtain the temperature of the DUT. For example, an IR measurement system normally operates in the 2-5µm waveband, whereas luminescence techniques use radiation in the visible region.

The infra-red thermal measurement technique is possibly the most common non-contact, non-destructive optical technique for measuring the temperature of an electronic device. IR thermal microscopy is completely passive and uses naturally emitted IR radiation from the surface of DUT to measure the temperature. It can also provide a 2D thermal map of the surface of the device. The method also allows relatively large device surface areas (depending upon the magnification of objective used) to be measured.

IR thermal microscopes are available commercially and instrumentation exists to identify hotspots for microelectronic failure analysis (as multi-array IR detectors are used to obtain an instantaneous matrix of temperature measurements) [45] over the surface of the DUT [46]. Commercial state-of-the-art IR microscopes typically offer a spatial resolution of ~2.5µm (in the 2.5 – 6µm wavelength bands) [47] and a range of analysis options which include real time thermal mapping and thermal transient detection. Although, the IR measurement technique has many advantages it suffers from temperature errors when low emissivity and optically transparent materials are studied. However, the method has been successfully used for the thermal analysis of GaAs FETs, MMICs [48], MEMS sensors [47] and RF amplifiers [49].

To further improve the temperature measurement on optically transparent and highly reflective surfaces, a novel method has been developed at DMU that employs a carbon microparticle with a high surface emissivity [7] – known as an IR probe [50]. The principles of IR thermal measurement are explained in more detail in Chapter 3**.**

2.3.2.2. Thermo-reflectance:

Reflection of light from a surface of a DUT can also be temperature dependant. In this technique, the intensity of the reflected photon from the surface of a DUT is used to determine the temperature profile. The thermo-reflectance method can be used to make sub-micron temperature mappings [51]. The main advantages of this technique are; non-contact and non-destructive approach for measuring the steady state and transient surface temperature of submicron features of electronic devices. The technique can provide good spatial thermal resolution (<0.5µm) [52]. Very short thermal transient measurements are also possible using this measurement method, with a 10ns of thermal transient resolution being claimed [3], [53]. The schematic of a thermo-reflectance measurement arrangement is shown in Figure 2.3.

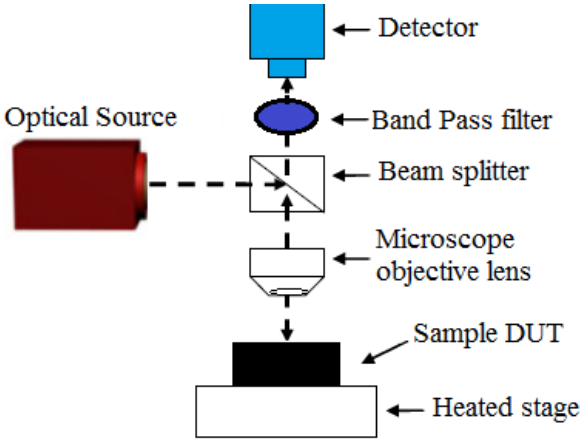

Figure 2.3: Schematic of thermo-reflectance measurement arrangement.

A parameter characterising the thermo-reflectance phenomenon is the thermo-reflectance coefficient (C_{TR}), which is the relative change in the reflectance per unit change in the temperature and is given by the equation **(2.4)**;

$$C_{TR} = \frac{1}{R}\frac{\Delta R}{\Delta T} \qquad \textbf{(2.4)}$$

Where, $\Delta R/R$ is the relative variation of reflectivity.

The accuracy of this technique depends on the level of noise contribution from the detector, electronics and quantisation processes. This technique has been used for making the temperature measurements of interconnects, semiconductor devices and thin films [3], [54], [55]. Although it should be added, the technique is still in its development infancy and interpretation of DUT temperature results requires great deal of experience and expertise.

2.3.2.3. Micro – Raman spectroscopy:

In recent years, laser Micro – Raman spectroscopy has become recognised as an optical method to explore the thermal characteristics of semiconductor devices [56]. In this measurement technique, a focused laser source is used to excite the DUT. A small portion of the incident laser photons are in-elastically scattered (known as Raman scattering) by the phonons causing a small shift in frequency of the photons. The phonon vibration is dependent on temperature. If the temperature dependence of the phonon shift is known, then the change in photon frequency with temperature can be used to characterise the thermal profile of the semiconductor device [57]. The Micro – Raman spectroscopy has been used to measure the temperature of Si MOSFETs, AlGaN/GaN HFETs [58] and GaAs HEMTs devices [59].

One of the main advantages of using the Raman technique for temperature measurements is, a high spatial thermal resolution of <1µm is possible [60]. High temporal resolution (in nanoseconds) and the possibility to measure the temperature distribution through different layers of semiconductor are some of the advantages of this technique. However, using this technique, it is difficult to create a detailed thermal map over large surface area, as measurements can only be made at single point and require long periods of time to average a number of individual readings [46]. Additionally, this technique is not suitable for making the

temperature measurements on metallised surfaces (because the metal phonons cannot be detected due to very low in energy) [46], [61], for instance, on the gold contacts of an electronic device. In this technique, there is also a possibility of some temperature error due to laser induced heating and carrier generation within the semiconductor.

2.3.2.4. Luminescence:

An external stimulation such as electric field or photo excitation will cause the emission of radiation which is known as luminescence [62]. On the basis of external stimulation, luminescence can be categorised into; electroluminescence or photoluminescence. Both of which have been used for measuring the temperature of compound semiconductor devices [3], [63]. The emitted radiation is monitored as a function of temperature to obtain the peak temperature of the device under test. The luminescence technique is useful for making the measurements on direct bandgap materials such as GaAs [3]. The spatial resolution of the photoluminescence method is ~1µm with temperature accuracy of 1 °C [3].

The potential of the above technique can be explored using nanotechnology and has been demonstrated [64]. In this method, the nano-sensors composed of Rhodamine B (RhB) fluorophores conjugated to a silica sol-gel, were spread over the surface of the CMOS MEMS micro-hotplate [64], and dried on the surface. The MEMS device was a miniature micro-heater with a high operating temperature and is small enough to be mounted beneath the microscope. The temperature dependent fluorescence intensity of the luminescent nano-sensors which were spread across the surface of miniature micro-heater can then be used for the thermal characterisation of nano/micro scale electronic devices.

2.3.2.5. Other optical temperature measurement techniques:

There are other optical characteristics that can be used for measuring the temperature of devices. For example; thermo-optic effect (the change in temperature with the changes in the optical index of refraction of a material). This technique has been used to measure the temperature in waveguide modulators [65]. A multi-spectral technique is another example of an optical measurement technique. In this technique, the temperature dependence of spectral distribution of infra-red radiation emitted by the surface of device under test, without knowing the emissivity, is used to measure the temperature [7]. A temperature measurement using a multi-spectral technique has also been demonstrated [66]. This technique is more suitable to study the thermal characteristics of surfaces heated to more than 600 K [7].

2.4. Comparison of thermal measurement techniques:

Thermal management of electronic devices has become increasingly important with the continuing commercial trends towards smaller, faster and low power electronic devices. The ultimate choice of the temperature measurement method depends on the device type to be tested, spatial resolution and measurement accuracy etc. The main advantages and disadvantages of different thermal measurement technique that are reviewed in this chapter are summarised in the Table 2.1.

Table 2.1: Comparison of thermal measurement techniques.

Methods	Advantages	Disadvantages
Liquid crystals	• Spatial resolution of ~1µm • Easy to use and high accuracy with temperature resolution of 0.1 °C	• Heat spreading occurs • Only a single point temperature can be made with each type of liquid crystals
Thermocouples	• Easily available • Capable of measuring wide range of temperatures (up to ~3000 °C, dependant on metal types) • Real-time measurements	• Spatial resolution limited to the probe size (~20µm) • Only a single point temperature measurement can be made
Atomic Force Microscopy (AFM)	• High spatial resolution <1µm • Measurement can be made on almost any material	• Heat spreading occurs due to physical contact • Small area measurements
Electrical methods	• Can measure the temperature on fully packaged devices • No physical contact probe for temperature measurement • No need of special sample preparation	• Only gives an average temperature • Cannot be used to detect the hotspots or create the 2D thermal maps
IR thermal microscopy	• Matrix of temperature measurement can be made to create 2D thermal map • Thermal maps can be made over large areas • Measurements can be made on metals	• Spatial resolution limited to ~2.5µm (in the 2.5 - 6µm wavelength bands) • Temperature errors when low emissivity and optically transparent materials are under study
Thermo-reflectance	• Spatial resolution <0.5µm • Can be used to make the very short thermal transient measurements, with a 10ns resolution	• Expensive technique
Micro-Raman spectroscopy	• High spatial resolution <1µm • Measurements can be made on semiconductor layers	• Small area measurements • Measurements cannot be made on metals • Not a real time measurement • Expensive technique
Luminescence	• Potential spatial resolution of < 100nm	• Single point measurement • Not real time • Manipulation of the nano-sensors

2.5. Summary:

There are a number of thermal characterisation techniques that can be used to thermally profile micro-scale electronic devices. Electrical techniques can be used to make the temperature measurements on packaged devices, however, they will only be able to provide average temperatures. Contact methods are required to make a physical contact and would damage delicate devices. Optical methods, such as IR microscopy, have been widely used to characterise the thermal behaviour of micro-scale electronic devices, and have a major benefit of being non-contact and non-invasive. In addition, these methods can be used to obtain a real time 2D thermal maps and enable to identify the hot areas within a structure which could lead to a possible failure sites.

Reviewing the thermal measurement techniques, IR microscopy was well suited and one of the few techniques which can be used to perform the thermal characterisation across the very thin (~5 µm) heater membrane of the MEMS based IR emitters studied in this work. Hence, it was used in this research work which enabled the thermal characterisation of the IR emitters to temperatures of 700 °C. For short wave infra-red emission (1.4 µm – 2.5 µm), the operating temperature of the IR emitters is in excess of 800 °C. To enable thermal characterisation of the delicate heater membrane of the IR emitter at elevated temperatures (>700 °C), a new non-contact temperature measuring techniques will require development, and in this present research, a passive optical approach based on thermal-incandescence microscopy is proposed (which is fully described in Chapter 7).

2.6. References:

[1] D. Pierścińska, "Thermoreflectance spectroscopy—Analysis of thermal processes in semiconductor lasers," *Journal of Physics D: Applied Physics*, vol. 51, no. 1, p. 013001, Jan. 2018, doi: 10.1088/1361-6463/aa9812.

[2] G. Zeng, H. Cao, W. Chen, and J. Lutz, "Difference in Device Temperature Determination Using p-n-Junction Forward Voltage and Gate Threshold Voltage," *IEEE Transactions on Power Electronics*, vol. 34, no. 3, pp. 2781–2793, Mar. 2019, doi: 10.1109/TPEL.2018.2842459.

[3] D. L. Blackburn, "Temperature measurements of semiconductor devices-a review," in *Twentieth Annual IEEE Semiconductor Thermal Measurement and Management Symposium*, 2004, vol. 70.

[4] M. Akita, S. Kishimoto, and T. Mizutani, "High-frequency measurements of AlGaN/GaN HEMTs at high temperatures," *IEEE Electron Device Letters*, vol. 22, no. 8, pp. 376–377, Aug. 2001, doi: 10.1109/55.936348.

[5] C. Qian *et al.*, "Thermal Management on IGBT Power Electronic Devices and Modules," *IEEE Access*, vol. 6, pp. 12868–12884, 2018, doi: 10.1109/ACCESS.2018.2793300.

[6] A. Sarua *et al.*, "Thermal Boundary Resistance Between GaN and Substrate in AlGaN/GaN Electronic Devices," *IEEE Transactions on Electron Devices*, vol. 54, no. 12, pp. 3152–3158, Dec. 2007, doi: 10.1109/TED.2007.908874.

[7] R. Hopper, "Accurate temperature measurements on semiconductor devices," Ph.D., De Montfort University, 2010.

[8] F. Arai *et al.*, "Ultra-small site temperature sensing by carbon nanotube thermal probes," in *4th IEEE Conference on Nanotechnology, 2004.*, 2004, pp. 146–148, doi: 10.1109/NANO.2004.1392278.

[9] J. Bodzenta, "Scanning thermal microscopy—a tool for thermal measurement in the nanoscale," in *Frontiers of Nanoscience*, vol. 14, Elsevier, 2019, pp. 181–213.

[10] D. G. Cahill, K. Goodson, and A. Majumdar, "Thermometry and Thermal Transport in Micro/Nanoscale Solid-State Devices and Structures," *J. Heat Transfer*, vol. 124, no. 2, pp. 223–241, Dec. 2001, doi: 10.1115/1.1454111.

[11] S. Gomès, A. Assy, and P.-O. Chapuis, "Scanning thermal microscopy: A review," *physica status solidi (a)*, vol. 212, no. 3, pp. 477–494, 2015,doi: 10.1002/pssa.201400360

[12] J. König, S. Moller, N. Granzow, and C. Cierpka, "On the application of a supercontinuum white light laser for simultaneous measurements of temperature and velocity fields using thermochromic liquid crystals," *Experimental Thermal and Fluid Science*, vol. 109, p. 109914, 2019, doi: 10.1016/j.expthermflusci.2019.109914.

[13] A. M. Chaudhari, T. M. Woudenberg, M. Albin, and K. E. Goodson, "Transient liquid crystal thermometry of microfabricated PCR vessel arrays," *Journal of Microelectromechanical Systems*, vol. 7, no. 4, pp. 345–355, Dec. 1998, doi: 10.1109/84.735341.

[14] J. Park and C. C. Lee, "A new thermal measurement technique using nematic liquid crystals with IR laser illumination for visible light emitting devices," in *Proceedings Electronic Components and Technology, 2005. ECTC '05.*, 2005, pp. 1607-1610 Vol. 2, doi: 10.1109/ECTC.2005.1442005.

[15] J. H. Park and C. C. Lee, "A new configuration of nematic liquid crystal thermography with applications to GaN-based devices," *IEEE Transactions on Instrumentation and Measurement*, vol. 55, no. 1, pp. 273–279, Feb. 2006, doi: 10.1109/TIM.2005.861243.

[16] M. Duff and J. Towey, "Two Ways to Measure Temperature Using Thermocouples Feature Simplicity, Accuracy, and Flexibility," in *Volume 44, Number 4, 2010 A forum for the exchange of circuits, systems, and software for real-world signal processing*, p. 3.

[17] P. R. N. Childs, J. R. Greenwood, and C. A. Long, “Review of temperature measurement,” *Review of scientific instruments*, vol. 71, no. 8, pp. 2959–2978, 2000, doi: 10.1063/1.1305516.
[18] T. Augspurger, M. Koch, F. Klocke, and B. Döbbeler, “Investigation of transient temperature fields in the milling cutter under CO2 cooling by means of an embedded thermocouple,” *Procedia CIRP*, vol. 79, pp. 33–38, Jan. 2019, doi: 10.1016/j.procir.2019.02.007.
[19] P. Pandey, “IR Thermal measurement on semiconductor devices.,” De-Montfort University, UK, 2014.
[20] M. M. Kim, A. Giry, M. Mastiani, G. O. Rodrigues, A. Reis, and P. Mandin, “Microscale thermometry: A review,” *Microelectronic Engineering*, vol. 148, pp. 129–142, Dec. 2015, doi: 10.1016/j.mee.2015.11.002.
[21] X. H. Jin, B. H. Ma, T. Qiu, and J. J. Deng, “ITO thin film thermocouple for transient high temperature measurement in scramjet combustor,” in *2017 19th International Conference on Solid-State Sensors, Actuators and Microsystems (TRANSDUCERS)*, 2017, pp. 1148–1151, doi: 10.1109/TRANSDUCERS.2017.7994256.
[22] Y.-Q. Tang, W.-Z. Fang, H. Lin, and W.-Q. Tao, “Thin film thermocouple fabrication and its application for real-time temperature measurement inside PEMFC,” *International Journal of Heat and Mass Transfer*, vol. 141, pp. 1152–1158, Oct. 2019, doi: 10.1016/j.ijheatmasstransfer.2019.07.048.
[23] P. Tovee, M. Pumarol, D. Zeze, K. Kjoller, and O. Kolosov, “Nanoscale spatial resolution probes for scanning thermal microscopy of solid state materials,” *Journal of Applied Physics*, vol. 112, no. 11, p. 114317, 2012, doi: 10.1063/1.4767923.
[24] O. Sahin, S. Magonov, C. Su, C. F. Quate, and O. Solgaard, “An atomic force microscope tip designed to measure time-varying nanomechanical forces,” *Nature nanotechnology*, vol. 2, no. 8, p. 507, Aug. 2007, doi:10.1038/nnano.2007.226.
[25] E. Hendarto, A. Altes, R. Heiderhoff, J. C. H. Phang, and L. J. Balk, “Investigation on the thermal distribution of nmosfets under different operation modes by scanning thermal microscopy,” in *Reliability Physics Symposium, 2005. Proceedings. 43rd Annual. 2005 IEEE International*, 2005, pp. 294–299, doi: 10.1109/RELPHY.2005.1493101.
[26] R. Aubry *et al.*, “SThM Temperature Mapping and Nonlinear Thermal Resistance Evolution With Bias on AlGaN/GaN HEMT Devices,” *IEEE Transactions on Electron Devices*, vol. 54, no. 3, pp. 385–390, Mar. 2007, doi: 10.1109/TED.2006.890380.
[27] W. Qu, X. Chen, and C. Ke, “Temperature-dependent frictional properties of ultra-thin boron nitride nanosheets,” *Appl. Phys. Lett.*, vol. 110, no. 14, p. 143110, Apr. 2017, doi: 10.1063/1.4979835.
[28] K. E. Mitchell, V. Gardner, S. W. Allison, and F. Sabri, “Synthesis and characterization of flexible thermographic phosphor temperature sensors,” *Optical Materials*, vol. 60, pp. 50–56, Oct. 2016, doi: 10.1016/j.optmat.2016.06.039.
[29] Z. Ghorbani-Tari, Y. Chen, and Y. Liu, “Complementary temperature-sensitive paint measurements and CFD analysis of wall heat transfer of cubes-in-tandem in a turbulent channel flow,” *Experimental Thermal and Fluid Science*, vol. 98, pp. 56–67, Nov. 2018, doi: 10.1016/j.expthermflusci.2018.05.014.
[30] G. Zeng, H. Cao, W. Chen, and J. Lutz, “Difference in device temperature determination using pn-junction forward voltage and gate threshold voltage,” *IEEE Transactions on Power Electronics*, pp. 1–1, 2018, doi: 10.1109/TPEL.2018.2842459.
[31] S. M. Sze and K. K. Ng, *Physics of semiconductor devices*. John Wiley & Sons, 2006.
[32] L. Alhmoud and A. K. Al-Jiboory, “Insulated-gate bipolar transistor junction temperature estimation based on $\mathscr{H}\infty$ robust controller in wind energy applications,” *Wind Engineering*, Sep. 2019, doi: 10.1177/0309524X19877645.

[33] J. R. Waldrop, K. C. Wang, and P. M. Asbeck, “Determination of junction temperature in AlGaAs/GaAs heterojunction bipolar transistors by electrical measurement,” *IEEE Transactions on Electron Devices*, vol. 39, no. 5, pp. 1248–1250, May 1992, doi: 10.1109/16.129117.
[34] V. Mehrotra, K. Boutros, and B. Brar, “Electric-Field Dependence of Junction Temperature in GaN HEMTs,” in *2007 65th Annual Device Research Conference*, 2007, pp. 143–144, doi: 10.1109/DRC.2007.4373689.
[35] M. X. Feng *et al.*, “Thermal characterization of GaN-based laser diodes by forward-voltage method,” *Journal of Applied Physics*, vol. 111, no. 9, p. 094513, May 2012, doi: 10.1063/1.4716003.
[36] J. W. Lee *et al.*, “Mobility analysis of surface roughness scattering in FinFET devices,” *Solid-State Electronics*, vol. 62, no. 1, pp. 195–201, Aug. 2011, doi: 10.1016/j.sse.2011.04.020.
[37] G. Pavlidis, S. Pavlidis, E. R. Heller, E. A. Moore, R. Vetury, and S. Graham, “Characterization of AlGaN/GaN HEMTs Using Gate Resistance Thermometry,” *IEEE Transactions on Electron Devices*, vol. 64, no. 1, pp. 78–83, Jan. 2017, doi: 10.1109/TED.2016.2625264.
[38] D. B. Estreich, “A DC technique for determining GaAs MESFET thermal resistance,” *IEEE Transactions on Components, Hybrids, and Manufacturing Technology*, vol. 12, no. 4, pp. 675–679, Dec. 1989, doi: 10.1109/33.49032.
[39] B. K. Schwitter, A. E. Parker, S. J. Mahon, and M. C. Heimlich, “Transient gate resistance thermometry demonstrated on GaAs and GaN FET,” in *2016 IEEE MTT-S International Microwave Symposium (IMS)*, 2016, pp. 1–4, doi: 10.1109/MWSYM.2016.7540035.
[40] H. Chen, V. Pickert, D. J. Atkinson, and L. S. Pritchard, “On-line monitoring of the MOSFET device junction temperature by computation of the threshold voltage,” pp. 440–444, Jan. 2006, doi: 10.1049/cp:20060147.
[41] S. Choi *et al.*, “Thermal Design and Characterization of Heterogeneously Integrated InGaP/GaAs HBTs,” *IEEE Transactions on Components, Packaging and Manufacturing Technology*, vol. 6, no. 5, pp. 740–748, May 2016, doi: 10.1109/TCPMT.2016.2541615.
[42] A. R. Reid, T. C. Kleckner, M. K. Jackson, D. Marchesan, S. J. Kovacic, and J. R. Long, “Thermal resistance in trench-isolated Si/SiGe heterojunction bipolar transistors,” *IEEE Transactions on Electron Devices*, vol. 48, no. 7, pp. 1477–1479, Jul. 2001, doi: 10.1109/16.930671.
[43] J. Zhang, M. Du, L. Jing, K. Wei, and W. G. Hurley, “IGBT Junction Temperature Measurements: Inclusive of Dynamic Thermal Parameters,” *IEEE Transactions on Device and Materials Reliability*, vol. 19, no. 2, pp. 333–340, Jun. 2019, doi: 10.1109/TDMR.2019.2910182.
[44] N. Killat *et al.*, “Thermal Properties of AlGaN/GaN HFETs on Bulk GaN Substrates,” *IEEE Electron Device Letters*, vol. 33, no. 3, pp. 366–368, Mar. 2012, doi: 10.1109/LED.2011.2179972.
[45] K. E. Goodson, “Infrared Microscopy | Stanford NanoHeat Lab,” *Stanford nanoHeat*. [Online]. Available: https://nanoheat.stanford.edu/tools/infrared-microscopy. [Accessed: 18-May-2019].
[46] J. Glover, “The design and thermal measurement of III-V integrated micro-coolers for thermal management of microwave devices,” Ph.D., De Montfort University, 2016.
[47] R. H. Hopper, I. Haneef, S. Z. Ali, F. Udrea, and C. H. Oxley, “Use of carbon micro-particles for improved infrared temperature measurement of CMOS MEMS devices,” *Meas. Sci. Technol.*, vol. 21, no. 4, p. 045107, Mar. 2010, doi: 10.1088/0957-0233/21/4/045107.

[48] C. H. Oxley, B. M. Coaker, and N. E. Priestley, “Measured thermal images of a gallium arsenide power {MMIC} with and without {RF} applied to the input,” *Solid-State Electronics*, vol. 47, no. 4, pp. 755–758, 2003, doi: http://dx.doi.org/10.1016/S0038-1101(02)00356-8.
[49] R. Hopper, D. Prime, G. Evans, K. Lee, and C. Oxley, “Improved infrared temperature measurement of RF devices,” 2013, Accessed: Aug. 29, 2018. [Online]. Available: http://www.armms.org/media/uploads/1326110849.pdf.
[50] C. H. Oxley, R. Hopper, D. Prime, M. C. Leaper, G. Evans, and A. Levick, “Probe propels IR thermal microscopy to a new level,” *Compound semiconductor*, vol. 17, pp. 33–36, Feb. 2011.
[51] A. E. Helou, P. E. Raad, and P. Komarov, “Temperature dependence of the thermoreflectance coefficient of gold by the use of a phase-locked single-point measurement approach,” in *2018 34th Thermal Measurement, Modeling Management Symposium (SEMI-THERM)*, 2018, pp. 161–164, doi: 10.1109/SEMI-THERM.2018.8357368.
[52] M. G. Burzo, P. L. Komarov, and P. E. Raad, “Noncontact transient temperature mapping of active electronic devices using the thermoreflectance method,” *IEEE Transactions on Components and Packaging Technologies*, vol. 28, no. 4, pp. 637–643, Dec. 2005, doi: 10.1109/TCAPT.2005.859738.
[53] Y. S. Ju and K. E. Goodson, “Short-time-scale thermal mapping of microdevices using a scanning thermoreflectance technique,” *Journal of heat transfer*, vol. 120, no. 2, pp. 306–313, 1998.
[54] H. Zhang, S.-B. Wen, and A. Bhaskar, “Two-wavelength thermoreflectance in steady-state thermal imaging,” *Appl. Phys. Lett.*, vol. 114, no. 15, p. 151902, Apr. 2019, doi: 10.1063/1.5087011.
[55] M. J. Tadjer *et al.*, “Electrothermal Evaluation of AlGaN/GaN Membrane High Electron Mobility Transistors by Transient Thermoreflectance,” *IEEE Journal of the Electron Devices Society*, vol. 6, pp. 922–930, 2018, doi: 10.1109/JEDS.2018.2860792.
[56] M. Kuball and J. W. Pomeroy, “A Review of Raman Thermography for Electronic and Opto-Electronic Device Measurement With Submicron Spatial and Nanosecond Temporal Resolution,” *IEEE Transactions on Device and Materials Reliability*, vol. 16, no. 4, pp. 667–684, Dec. 2016, doi: 10.1109/TDMR.2016.2617458.
[57] P. J. McNally and V. G. Sathe, “Raman Spectroscopy: Basics and Applications,” in *Nanomaterials*, S. C. Singh, H. Zeng, C. Guo, and W. Cai, Eds. Wiley-VCH Verlag GmbH & Co. KGaA, 2012, pp. 495–534.
[58] M. Kuball *et al.*, “Measurement of temperature distribution in multifinger AlGaN/GaN heterostructure field-effect transistors using micro-Raman spectroscopy,” *Appl. Phys. Lett.*, vol. 82, no. 1, pp. 124–126, Dec. 2002, doi: 10.1063/1.1534935.
[59] A. Sarua, A. Bullen, M. . Haynes, and M. Kuball, “High-Resolution Raman Temperature Measurements in GaAs p-HEMT Multifinger Devices,” *IEEE Transactions on Electron Devices*, vol. 54, no. 8, pp. 1838–1842, Aug. 2007, doi: 10.1109/TED.2007.901349.
[60] G. Brocero, Y. Guhel, P. Eudeline, J. P. Sipma, C. Gaquière, and B. Boudart, “Measurement of Self-Heating Temperature in AlGaN/GaN HEMTs by Using Cerium Oxide Micro-Raman Thermometers,” *IEEE Transactions on Electron Devices*, vol. 66, no. 10, pp. 4156–4163, Oct. 2019, doi: 10.1109/TED.2019.2935335.
[61] R. H. Hopper, C. H. Oxley, J. W. Pomeroy, and M. Kuball, “Micro-Raman/Infrared Temperature Monitoring of Gunn Diodes,” *IEEE Transactions on Electron Devices*, vol. 55, no. 4, pp. 1090–1093, Apr. 2008, doi: 10.1109/TED.2008.916709.

[62] M. A. Omary and H. H. Patterson, “Luminescence, Theory,” in *Encyclopedia of Spectroscopy and Spectrometry (Third Edition)*, J. C. Lindon, G. E. Tranter, and D. W. Koppenaal, Eds. Oxford: Academic Press, 2017, pp. 636–653.
[63] C.-H. Lin *et al.*, “Nanoscale mapping of temperature and defect evolution inside operating AlGaN/GaN high electron mobility transistors,” *Appl. Phys. Lett.*, vol. 95, no. 3, p. 033510, Jul. 2009, doi: 10.1063/1.3189102.
[64] V. M. Chauhan *et al.*, “Thermo-optical characterization of fluorescent rhodamine B based temperature-sensitive nanosensors using a CMOS MEMS micro-hotplate,” *Sensors and Actuators B: Chemical*, vol. 192, pp. 126–133, Mar. 2014, doi: 10.1016/j.snb.2013.10.042.
[65] M. Allard, R. A. Masut, and M. Boudreau, “Temperature determination in optoelectronic waveguide modulators,” *Journal of lightwave technology*, vol. 18, no. 6, p. 813, 2000.
[66] T. Pierre, B. Rémy, and A. Degiovanni, “Multi-Spectral Techniques Applied for the Measurement of the Microscale Temperature Through Cooled Multiplier Tube in Photon Counting Mode,” in *ASME 2008 First International Conference on Micro/Nanoscale Heat Transfer*, 2008, pp. 845–851.

Chapter 3

Infra-Red thermal measurement:

This chapter describes the basic infra-red (IR) thermal measurement technique along with a critical analysis of the different experimental stages encompassed in the measurement technique. The chapter also includes a description of the IR instrumentation and experimental setup used for the temperature measurement of the miniature micro-electro-mechanical systems (MEMS) micro-heater used in gas sensors.

Infra-red thermal measurement is a powerful, widely accepted, non-contact technique that can be used to measure the temperature of active electronic devices, as introduced in Chapter 2. It utilises naturally emitted infra-red radiation from the surface of the device under test (DUT). The emission of natural IR radiation from the DUT means that optics can be used to capture the radiation and therefore the measurement apparatus is not in physical (isothermal) contact with the DUT. This is a great advantage over physical contact techniques, as discussed in Chapter 2. The method can be set-up to measure the temperature at points over the surface area of the DUT by using a matrix of IR detectors; effectively giving a 2D temperature map, enabling the identification of hotspots on the surface of the DUT. Infra-red temperature measurements will give a good estimate of the device surface temperature provided the surface emissivity of the DUT is known. This chapter includes the introduction to the IR thermal measurement technique, instrumentation and software that has been used for the thermal measurement of miniature micro-heaters. The IR microscope at De Montfort University (DMU) is a commercially available Infrascope-II manufactured by Quantum Focus Instruments (QFI). The experimental process of making the IR temperature measurements using the IR microscope will be described in detail in section (**3.2.3**).

3.1. IR thermal microscopy:

Infra-red thermal microscopy as discussed is an optical method which will provide a 2D temperature profile of a biased micro-electronic circuit [1], [2]. In this technique the device temperature is calculated from the IR radiation emitted by the material of the device surface [3]. The Quantum Focus IR microscope offers a maximum spatial resolution of approximately 2.5μm (in the mid IR spectrum of wavelengths, λ = 2.5 to 6μm) and can be equipped with both transient and continuous wave (CW) imaging detectors. The instruments come with a range of objective lenses, for example low magnification objectives (×1) are used to image thermal maps of large surface areas (10 × 10 mm) and high magnification objective lenses (×25) can be used to image smaller areas (0.464 × 0.464 mm). This is particularly useful, if a hot area has been identified using the low magnification objective, it can then be imaged in more detail using the higher magnification objective lens. The Figure 3.1 shows a schematic of an IR thermal microscopy arrangement.

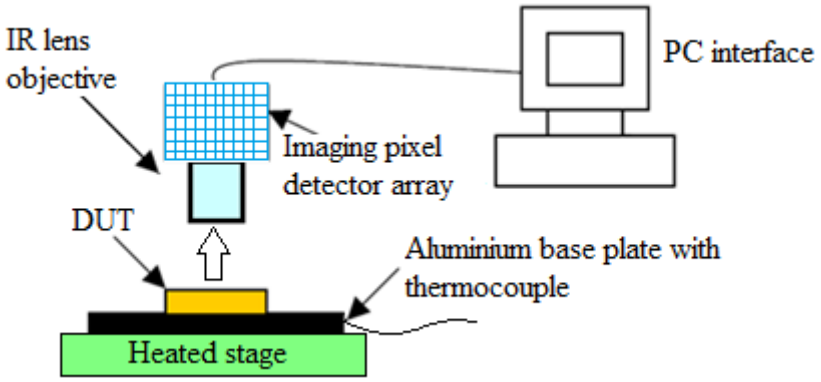

Figure 3.1: Schematic arrangement of IR thermal microscopy [4].

As thermal IR microscopy is a passive technique it will not interfere with the DUT either electrically or thermally. IR microscopy can provide temperature sensitivity up to 0.1 K [5], [6] and hence can be used as a characterisation tool for helping in thermal management design of electronic devices and circuits.

To understand the principle behind the IR thermal microscopy, it is necessary to understand the theory of thermal radiation. Thermal radiation can be defined as electromagnetic radiation produced by the thermal motion of charged particles in matter [7], [8]. All matter with a temperature greater than absolute zero (0 Kelvin) will emit radiation. However, most of the radiation emitted by an object at around room temperature is considered as infra-red radiation. IR radiation is part of the electromagnetic spectrum [9] and occupies the frequencies between the visible light and radio waves with wavelengths from 0.7µm to 1000µm as shown in the Figure 3.2.

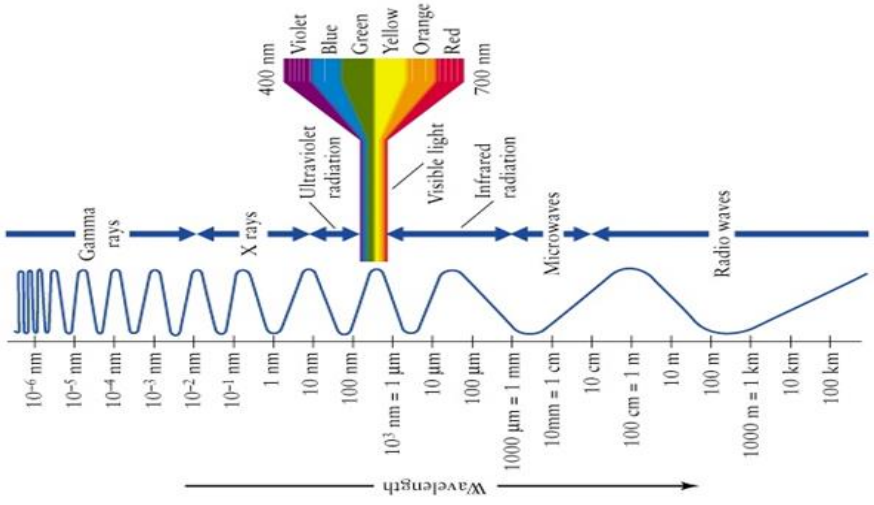

Figure 3.2: Electromagnetic spectrum [10].

The maximum energy that is possible to be radiated by an object is called black body radiation. It is a hypothetical object that can absorb electromagnetic radiations of all possible frequencies incident on its surface without any reflection. Thus, to maintain the conservation of energy, a black body must also be considered as a perfect emitter. A perfect absorber or emitter of radiation does not physically exist [11]. Therefore, the concept of emissivity arises and this is explained more in section **3.1.2**.

3.1.1. Planck's black body radiation law:

In 1900 Max Planck combined electromagnetism with thermal analysis by considering each atom as an individual oscillator giving a quanta (hv) of energy and from this he derived the expression for the electromagnetic radiation emitted by a black body when it is in thermal equilibrium at a known temperature. This is known as Planck's Law [8], [12];

$$w(\lambda) = \frac{2hc^2}{\lambda^5 \left\{ \exp\left(\frac{hc}{\lambda k_B T}\right) - 1 \right\}} \quad \textbf{(3.1)}$$

Where,

w is the power emitted by a black body (per unit area) as a function of wavelength λ at a known source temperature T.

c is speed of light in a vacuum = 2.997×10^8 m/s

h is Plank's constant = 6.63×10^{-34} J/ s

k_B is Boltzmann's constant = 1.38×10^{-23} watts/K

The spectral distribution of emitted radiation from a black body at different temperatures is shown in Figure 3.3 [13]. The plot shows the total power emitted by a black body increases as temperature increases.

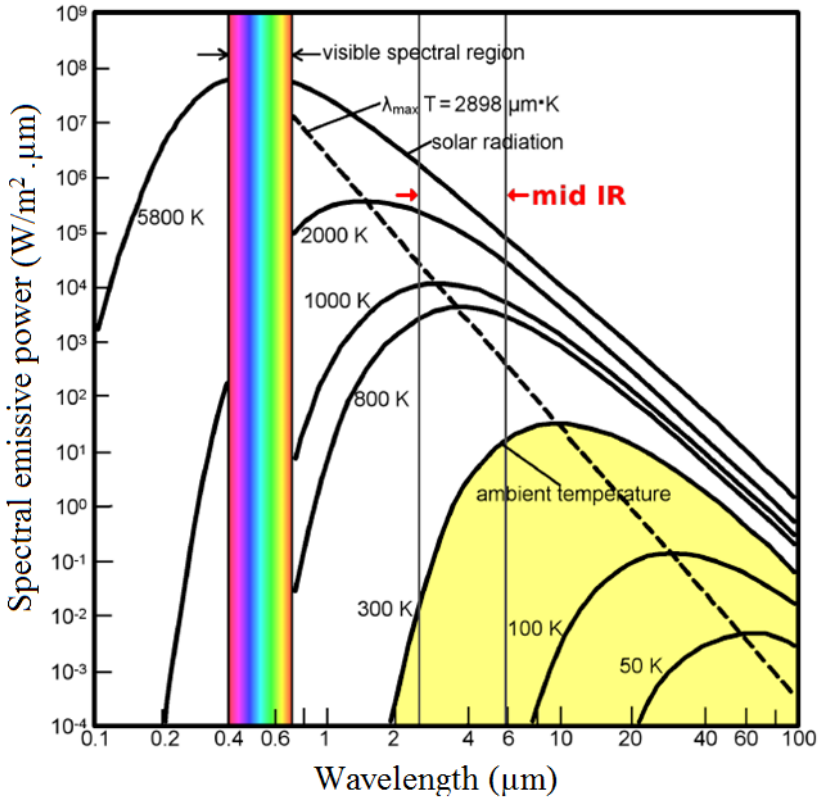

Figure 3.3: Spectral distribution of emitted radiation from black body at different temperatures [13].

The spectral distribution of thermally emitted radiation also shifts towards the shorter wavelengths as temperature increases (as described by Wein's law [14], [15], and shown in Figure 3.3). At lower temperature range (300 – 500 K), the spectral emissive power is maximum in the 2μm–10μm wavelength band. This spectral wavelength band is used by most of commercial passive IR detectors (for example, Indium antimony (InSb) IR detectors) to operate.

3.1.2. Emissivity concept and Stefan Boltzmann law:

In the real-world a perfect black body does not exist. Therefore, a parameter known as emissivity is introduced for the characterisation of radiative efficiency of a material surface. Emissivity is defined as the radiation efficiency of surfaces of real-world objects as compared to that of a perfect black body [4]. The perfect black body is said to have an emissivity equal to 1 [16]. However, at the same temperature, the real-world surface will emit IR radiation at a fraction of the black body radiation. Hence, the definition of surface emissivity (ε) is the ratio of real-world emitted radiation compared to that of a perfect black body at the same temperature and operating over the same spectral bandwidth. Therefore, surface emissivity varies between the values $0 < \varepsilon < 1$ [16].

$$\varepsilon = \frac{R_s}{R_b} \qquad \textbf{(3.2)}$$

Where, R_s and R_b are the level of emitted radiation (W/m^2.str) from the device surface and a black body respectively, at the same temperature and over the same wavelength range (assuming no background radiation is present).

The total amount of radiation emitted by a black body can be related to its temperature and is described by the Stefan Boltzmann law [17]. It states that the radiation power emitted per unit area of the surface of black body is directly proportional to the forth power of its absolute temperature and is given by equation [18],

$$w = \sigma . T^4 \qquad \textbf{(3.3)}$$

Where, σ = Stefan – Boltzmann constant and is given by 5.67×10^{-8} Wm^{-2}K^{-4} and T is absolute temperature.

The measurement is complicated by the fact that the amount of energy emitted by the device under test is dependent not only on its temperature but also on the surface emissivity (ε). The surface emissivity is dependent on the material and its surface finish. The total radiated power (w) from an object with an emissivity value ε is given by the equation,

$$w = \varepsilon \sigma . T^4 \qquad \textbf{(3.4)}$$

By measuring the emitted radiation level from a surface with a known emissivity, its temperature can be determined. Knowing the magnitude of the surface emissivity is very important for accurate temperature measurement using IR thermal microscopy, as it will determine the radiation emitted by the surface. The surface emissivity across a semiconductor device will vary widely depending on the semiconductor and metal contact materials, as well as its surface finish (matt, polished etc). Surface emissivity values of less than 0.1 are often observed on metals like gold, which is normally used as the contact metal for electronic devices.

There are two methods which can be used for measuring the surface emissivity of a material and these are described below:

3.1.2.1. One-temperature emissivity method:

The one-temperature emissivity technique assumes that the IR thermal microscopy has been calibrated against a black body (ε=1) over the required operating temperature range. The DUT is placed on a heated base-plate (which enables its temperature to be controlled) under the microscope objective and the radiance emitted is measured for a known base-plate temperature (T °C). The radiation R_T emitted (W/m^2.str) by the surface of the device at temperature T °C is given by the equation [19];

$$R_T = \varepsilon R_b + R_0 (1 - \varepsilon) \quad \textbf{(3.5)}$$

Where, R_b is the radiation levels (W/m^2.str) emitted by a black body at the same temperature (T °C) as the DUT surface and measured over the same wavelength range. R_0 is the level of external background radiance (W/m^2.str) at room temperature, and ε is the surface emissivity.

Equation **(3.5)** can be rearranged as shown in **(3.6)**,

$$\varepsilon = \frac{(R_T - R_0)}{(R_b - R_0)} \quad \textbf{(3.6)}$$

For a given temperature T °C the emissivity (ε) of the surface can be calculated using equation **(3.6)** by assuming the room temperature remains constant.

The use of this formula can be challenging, as the room temperature may vary after the manufacturers calibration and subsequent device measurements, leading to some variation in the surface emissivity. The method also requires the background radiance to be accurately measured, which is difficult as the background radiance (R_0) has a very small value (< 0.02 W/m^2.str) and depends on many factors, including convection currents, reflections and change in the background temperature etc. [20]. Therefore, the method is not very effective if the emissivity of the surface of the DUT is small leading to a small value of R_T, which could be a similar magnitude to the background radiation R_0. The stability of the measuring system over time is also very important, for example if R_T and R_0 are both small and similar in magnitude then any change in the instrument hardware could lead to an erroneous difference between them resulting in a large measurement error [20].

3.1.2.2. Two-temperature emissivity method:

The two-temperature emissivity method which was developed by P. Webb [19], is an improved emissivity measurement approach, and can be used to compensate for some of the short comings of the single temperature emissivity measurement. This approach involves measuring the change in emitted radiance level from the surface of the DUT at two known temperatures (T_1 and T_2). By assuming the external background radiation level (R_0) at room temperature remains constant during the measurement (this is a reasonable assumption provided T_1 and T_2 are not too dissimilar), the equation **(3.5)** can be rewritten to give the thermal radiation emitted by a surface of DUT at the two temperatures T_1 and T_2 respectively in equations **(3.7)** and **(3.8)**.

$$R_{T1} = \varepsilon R_{b1} + R_0 (1 - \varepsilon) \quad \textbf{(3.7)}$$

$$R_{T2} = \varepsilon R_{b2} + R_0 (1 - \varepsilon) \quad \textbf{(3.8)}$$

Where, R_{T1} and R_{T2} are the level of radiance emitted (W/m^2.str) by the surface at known temperature T_1 and T_2 respectively. R_{b1} and R_{b2} are the corresponding black body radiation values (W/m^2.str) at the two temperatures T_1 and T_2 respectively.

Subtracting the equation **(3.8)** from equation **(3.7)**, the surface emissivity is then given by the equation **(3.9)**, eliminating the background radiation R_0,

$$\varepsilon = \frac{(R_{T1} - R_{T2})}{(R_{b1} - R_{b2})} \qquad \textbf{(3.9)}$$

The IR microscope software (will be discussed in section **3.2.2**) calculates the surface emissivity value for every pixel within the detector matrix (Figure 3.1) thereby creating an emissivity map across the surface of the DUT. Once the emissivity map has been calculated; the IR microscope can be used to map the thermal profile of the electrically biased DUT.

The IR microscope software enables both automatic two-temperature emissivity and thermal mapping; using the built in black body calibration data (recalibrated on an annual basis). Unfortunately, the automatic emissivity correction does not account for any mechanical movement of the base-plate or DUT due to changes in operating temperature. If the movement happens at the time of the measurement process, the surface areas under study will become misaligned and provide incorrect emissivity values. Therefore, a manual two-temperature emissivity correction is recommended for correct emissivity values, in which the two radiance images can be manually realigned to overcome any mechanical movement.

The two-temperature emissivity method is an improvement over the one temperature emissivity calculation as it eliminates the background radiation R_0. Although, it improves the accuracy of emissivity measurements, there is possibility of error if the background radiation level changes with variation in the temperature or mechanical configuration around the DUT. This would necessitate re-measuring the surface emissivity of the DUT [19]. A heated-stage is used to heat the DUT to the two temperatures T_1 and T_2 to carry out the two-temperature emissivity correction. The heater will also emit radiation which will add to the normal background radiation leading to small changes in the surface emissivity and therefore minor errors in the measured temperature [19]. This problem can be minimised by carefully designing the base-plate and in particular the attachment of the DUT to the base-plate. Further, the thermal expansion or contraction of the base-plate and metal jig holding the DUT can result in problems with alignment of the detector pixels between making the measurements at the two temperatures T_1 and T_2. This can lead to an error in the radiance measurement resulting in incorrect emissivity values [2]. Therefore, the radiance images should always be checked and correctly realign between T_1 and T_2 radiance measurements, before using the emissivity map.

3.1.3. IR thermal measurement potential pitfalls:

The temperature accuracy of the IR thermal measurement technique is very dependent on the radiance property of the material under test. When a low emissivity/highly reflective metal or an optically transparent semiconductor are being measured there can be a significant temperature error in the DUT [19], [21]. When the materials have a low surface emissivity (< 0.1), the IR radiation emitted by the device surface will be similar in magnitude to the reflected background radiation and will give less reliable DUT temperature measurement compared to higher surface emissivity materials. Also, many materials, including semiconductors are transparent to IR radiation. Therefore, when making a surface emissivity measurements on transparent materials, the transparency could lead to anomalous surface emissivity values, as the detected IR radiation level will be the result from underlying layers as well as from the top surface of the semiconductor (Figure 3.4) [22], leading to errors in the measured surface temperature.

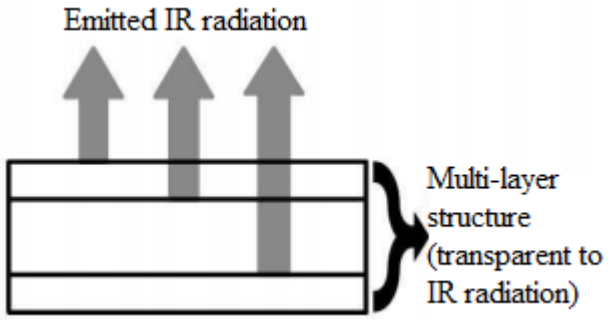

Figure 3.4: IR radiation emitted from multi-layer transparent materials.

If an accurate surface emissivity map of the DUT cannot be obtained, then neither can an accurate surface temperature. To overcome this problem, a high emissivity black coating can be applied on low emissivity and transparent materials in order to try to improve the temperature measurement accuracy. The coating used is normally a conventional black paint, which has a number of disadvantages. The black paint coating may cause heat spreading across the surface (thereby reducing the thermal spatial resolution) distorting the measured thermal profile, and it may also damage the electronic device. Further, the coating will be difficult to remove from the device surface, after measurement, without damaging the device. Therefore, this technique is normally used on sample devices, which can then be disposed of. Additionally, it will also obstruct the area where it is applied to the DUT making it difficult for any subsequent visual inspection.

To avoid these issues, a novel technique was developed at De Montfort University that uses a high emissivity spherical carbon microparticle, which is called a microparticle infra-red sensor (MPIRS) [21]. These are placed in temporary isothermal contact with the surface of the DUT at the point for the temperature measurement. The MPIRS technique is very useful to make temperature measurements on semiconductors (for example; Si, Ge, GaN and GaAs) which are transparent to IR radiation, and also on materials with low surface emissivity (for example; gold contacts) eliminating the need for physically coating the surface with a conventional black paint [21].

To use the MPIRS technique, the surface emissivity of the MPIRS has first to be measured, this is normally undertaken using the two-temperature emissivity measurement method, as already described in section **3.1.2.2**. The MPIRS will give an improved measurement over the black paint technique as little heat-spreading occurs. This is primarily due to the MPIRS having a low thermal mass and thermal time constant of the order of micro-seconds. The IR thermal measurement technique using MPIRS will be fully discussed in Chapter 4.

3.2. Methodology:

There are a number of commercial IR thermal measurement instruments on the market which can be used for making temperature measurements on electronic devices. As already stated the instrument which was used for this research work was an InfraScope-II manufactured by QFI (Quantum Focus Instruments, USA) and is described below:

3.2.1. QFI InfraScope-II:

Quantum Focus Instruments (QFI) is established as one of the world's leading manufacturer of IR thermal measurement equipment [23] and was an offshoot from the Barnes Company. Thermal measurement data is crucial for the design and characterisation of semiconductor devices (microwave, optical, MEMS etc.), and interfaces between the device and package [21]. The InfraScope-II primarily offers real time 2D IR temperature mapping with high thermal resolution (~3µm) and temperature sensitivity. Figure 3.5 shows a photograph of the QFI IR microscope system with supporting equipment and computers, which has been developed at De Montfort University.

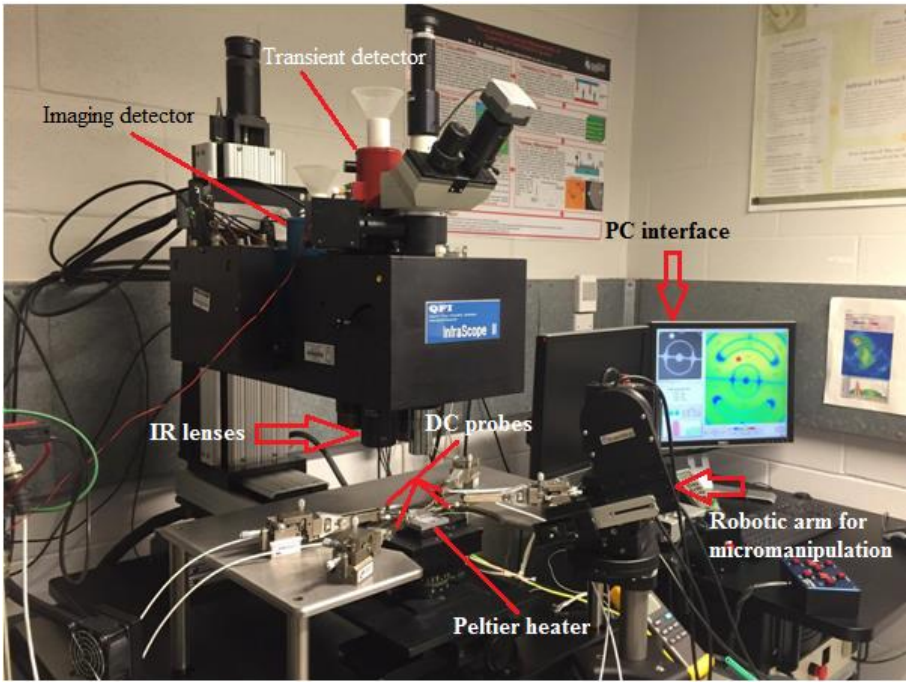

Figure 3.5: QFI InfrasScope-II available at De Montfort University.

The QFI InfraScope-II system at DMU offers 512 × 512 pixels, cooled (77 K) indium antimonide (InSb) imaging detector with three different objective lenses of magnification ×1, ×5 and ×25. The spatial resolutions at ×1, ×5 and ×25 are ~50µm, ~5µm and ~3µm with field of views 10 × 10mm, 2.3 × 2.3mm and 464 × 464µm respectively. The system is also capable of measuring the temperature range from 30 °C to ~700 °C. The high temperature measurement facility was recently added to enable thermal characterisation of MEMS micro-heaters, which operate at high temperatures (>500 °C).

QFI InfraScope-II has also been modified to make thermal transient measurements, with thermal response times close to 10 microseconds. The transient detector is a single element InSb detector cooled using liquid nitrogen (77 K). The transient detector can be used to measure the thermal response of switching power transistors, RF power transistors as well as a number of other devices including RFICs and ink jet devices when they operate in pulse mode [24].

The supporting equipment making up the DMU IR thermal measurement system is listed below:

- Anti-vibration table (which is used to reduce environmentally borne mechanical vibrations during the measurement).
- Built in DC/RF probe table.
- DC probes (Wentworth Laboratories PVX400) with magnetic base and these can hold both DC and RF probes.
- Adjustable stage mount (provided with controls to adjust the X and Y-axes, as well as the 90° of stage rotation along this plane). A temperature-controlled Peltier heater (used to control the base-plate temperature) is attached to this stage mount. The base-plate temperature can be set between 25 °C and 130 °C and controlled to better than (± 1 °C) using the thermal stage controller. To measure the base-plate temperature more precisely (± 0.1 °C) a thermocouple (K-type) has been embedded into the aluminium base-plate and mounted on the Peltier heater. The DUT is mounted on the temperature-controlled base-plate.
- The master PC supplied by QFI, contains the software required for controlling InfraScope-II and making IR thermal measurements.
- A dedicated Scientifica robotic arm [25], with micro-manipulator probe, which is used for placing and moving the MPIRS across the surface of DUT, and has been configured with Infrascope-II (this will be described further in Chapter 4)

3.2.2. Thermal map software:

The InfraScope-II comes with a dedicated software package (ThermalMap) for making thermal measurements. The software package has been continually updated as extra measurement facilities (transient detector, high temperature measurements etc.) have been added to the microscope.

This software is configured with an auxiliary program called headmaster, which is used for controlling the optical head functions, such as switching the lenses. A program called stage-

master is configured within the software to coordinate between the thermal stage controller and Peltier heater [26].

3.2.3. IR thermal measurement methodology/ DMU procedure:

The thermal measurement of a DUT can be in the form of a quasi-real time 2D thermal image. To obtain the image, three stages of measurement are made.

1) A radiance reference image is first taken, which measures the level of emitted radiation form the unbiased DUT at a known surface temperature.
2) An emissivity map is computed; that compares the level of emitted radiation from the device surface to that of black body at the same temperature.
3) The DUT is biased and a thermal map is computed using the already computed emissivity map. All three images of a thermal measurement need to be made at a known and constant base-plate temperature and the pixels of all three images need to be perfectly mechanically aligned to obtain a 'true' thermal profile of the biased DUT.

The DUT is first mounted on a thermally controlled base-plate. Care is taken to obtain a good thermal interface between the base-plate and Peltier heater-stage, which is often achieved by using thermal paste (e.g. RS Heat Sink Compound, RS 554-331). The liquid nitrogen (LN_2) cooled IR detectors are first topped up and time (approximately 30 minutes) is given for them to stabilise at 77 K. A complete description of the developed IR thermal measurement procedure in a chronological order is given below:

- The DUT is placed on the purpose built aluminium base-plate containing a calibrated K – type thermocouple (explained in Chapter 2), which monitors the base-plate temperature. This assembly is then mounted on a temperature controlled Peltier heater-stage. The aluminium base-plate helps to provide a large uniform thermal mass to compensate for any heating irregularities, enabling the temperature of the sample to be controlled accurately.
- Care is taken to obtain a good thermal interface between base-plate and the Peltier heater-stage as well as between the DUT and the aluminium base-plate, this is usually achieved by using a thermal paste. The DUT must be securely fixed to the thermally controlled base-plate because the InfraScope-II performs mathematical operations between sequential captured images and any DUT movement will reduce resolution and/or cause erroneous emissivity/temperature mapping results [23].
- The DUT must be positioned on a vertical alignment with the optics of the microscope.
- After mechanical mounting of the DUT on the base-plate/ Peltier heater; the electrical bias connection from the power supplies to the DUT are made using the available electrical connections (DC probes or dedicated connectors) and power suppliers.
- Open the QFI's ThermalMap software, installed in the master PC, and set the specific user defined base-plate temperature.
- The required IR objective lens is then selected. (Note: The first thermal exploratory measurements are normally made using a low magnification objective lens (×1) and if

hot areas or hotspots are identified then a high magnification objective lens (×5 or ×25) can be used to look at the hot areas/hotspots in more detail).

- To start the thermal measurements, the emissivity map is first produced. To make the thermal measurements using the two-temperature emissivity technique (benefits of this technique are explained in section **3.1.2.2**), two reference radiance images are captured at two elevated temperatures (for example, 65 °C and 95 °C) and need to perfectly aligned.
- After the computation of the 2D surface emissivity map; the DUT is biased and the radiance is re-measured. Using this radiance data and computed surface emissivity the temperature map can be obtained per pixel.
- From this data the 2D thermal map of the DUT over the same area of the device as the emissivity map can be computed and displayed. The 2D thermal map of the biased DUT can be used to analyse the thermal operation of the device, for example identify hot areas.

For a quick estimate of the surface temperature (or hotspots) of the biased DUT, IR thermal measurement can be made using one-temperature emissivity approach. In this technique, a background image is first captured to measure the level of background emitted radiation and then a radiance reference image of an unbiased DUT is captured only at a single known temperature to produce a single temperature emissivity map. After a surface emissivity map has been computed, the DUT is biased and then the emitted radiation is re-measured from the surface of biased DUT. Again a thermal map can be displayed which will highlight any regions of elevated temperature.

3.3. Summary:

The QFI Infrascope-II has been modified for high temperature measurement during this research work and has all the facilities to map temperature profiles of MEMS based micro-heaters to temperatures 700 °C. Other techniques will need to be investigated for temperatures above 700 °C. Two-temperature emissivity mapping will be used to thermally map the surface of the MEMS micro-heater as it will give improved sensitivity.

As already discussed, the MEMS micro-heater membrane is a thin semiconductor layer which will be transparent to IR radiation. Therefore, although thermal uniformity can be investigated using the two-temperature emissivity mapping and conventional IR microscopy the actual surface temperature of the micro-heater will be difficult to measure.

The MPIRS technique will be used to obtain a more accurate spot temperature of the MEMS micro-heater. To date, the MPIRS technology has only been used to temperatures around 200 °C, and therefore the use and calibration of MPIRS towards operating temperature of 700 °C will be explored as a part of this research work. Furthermore, the heater membranes are very thin and delicate and could be easily damaged when using MPIRS technology. Therefore an effective and precise manipulation of the MPIRS sensor or other techniques of positioning on the heater membrane will need to be explored.

3.4. References:

[1] J. Dallas *et al.*, "Thermal characterization of GaN vertical p-i-n diodes," in *2017 16th IEEE Intersociety Conference on Thermal and Thermomechanical Phenomena in Electronic Systems (ITherm)*, 2017, pp. 328–333, doi: 10.1109/ITHERM.2017.7992489.

[2] R. Hopper and C. Oxley, "Thermal measurement a requirement for monolithic microwave integrated circuit design," in *Proc. ARMMS*, 2008, pp. 385–390.

[3] Y. Wang *et al.*, "Ultrathin Radiation Coating Enabling High Accuracy and High Resolution Real-Time Infrared Imaging of Thermal MEMS Devices," in *2019 IEEE 32nd International Conference on Micro Electro Mechanical Systems (MEMS)*, 2019, pp. 1049–1052, doi: 10.1109/MEMSYS.2019.8870847.

[4] P. Pandey, C. Oxley, R. Hopper, Z. Ali, and A. Duffy, "Infra-red thermal measurement on a low-power infra-red emitter in CMOS technology," *IET Sci. Meas. Amp Technol.*, vol. 13, no. 1, pp. 25–28, Aug. 2018, doi: 10.1049/iet-smt.2018.5427.

[5] M. Zhao *et al.*, "Thermal analysis of AlGaN/GaN high-electron-mobility transistors by infrared microscopy," *Opt. Commun.*, vol. 291, pp. 104–109, Mar. 2013, doi: 10.1016/j.optcom.2012.10.077.

[6] G. Brocero, Y. Guhel, P. Eudeline, J. P. Sipma, C. Gaquière, and B. Boudart, "Measurement of Self-Heating Temperature in AlGaN/GaN HEMTs by Using Cerium Oxide Micro-Raman Thermometers," *IEEE Trans. Electron Devices*, vol. 66, no. 10, pp. 4156–4163, Oct. 2019, doi: 10.1109/TED.2019.2935335.

[7] E. M. Sparrow, *Radiation Heat Transfer, Augmented Edition*, 1st Edition. New York: Routledge, 2018.

[8] J. R. Howell, M. P. Menguc, and R. Siegel, *Thermal radiation heat transfer*, Sixth edition. New York: CRC press, 2015.

[9] A. Kumar and V. Dangi, "Electromagnetic spectrum and its impact on human life," *Int. J. Res. Educ. Sci. Methods*, vol. 4, no. 8, pp. 67–72, Aug. 2016.

[10] "Light: Electromagnetic waves, the electromagnetic spectrum and photons," *Khan Academy*. [Online]. Available: https://www.khanacademy.org/science/physics/light-waves/introduction-to-light-waves/a/light-and-the-electromagnetic-spectrum. [Accessed: 05-Jan-2020].

[11] R. Karwa, "Laws of Thermal Radiation," in *Heat and Mass Transfer*, R. Karwa, Ed. Singapore: Springer, 2017, pp. 665–696.

[12] B. C. Reed, "Supplementing Wien's Law with a measure of spectral breadth," *Phys. Educ.*, vol. 54, no. 5, p. 053005, Jul. 2019, doi: 10.1088/1361-6552/ab32a9.

[13] "IPS - Effects of low emissive wall coatings on thermal comfort and energy consumption," *IPS innovative products & systems*. [Online]. Available: http://www.ips-innovations.com/low_emissive_wall_coatings_ref.htm. [Accessed: 16-May-2019].

[14] R. Das, "Wavelength- and Frequency-Dependent Formulations of Wien's Displacement Law," *J. Chem. Educ.*, vol. 92, no. 6, pp. 1130–1134, Jun. 2015, doi: 10.1021/acs.jchemed.5b00116.

[15] A. E. Dubinov and I. N. Kitaev, "Generalized Wien's displacement law and Stefan-Boltzmann law for thermal radiation with a nonzero chemical potential," *J. Opt. Technol.*, vol. 85, no. 6, pp. 314–316, Jun. 2018, doi: 10.1364/JOT.85.000314.

[16] Y. Wang *et al.*, "A nanocomposite coating improving the accuracy in infrared temperature measurement for thermal micro-devices," *Sens. Actuators Phys.*, vol. 293, pp. 29–36, Jul. 2019, doi: 10.1016/j.sna.2019.02.019.

[17] G. Montambaux, "Generalized Stefan–Boltzmann Law," *Found. Phys.*, vol. 48, no. 4, pp. 395–410, Apr. 2018, doi: 10.1007/s10701-018-0153-4.

[18] B. J. Korites, “Planck’s Radiation Law and the Stefan-Boltzmann Equation,” in *Python Graphics: A Reference for Creating 2D and 3D Images*, B. J. Korites, Ed. Berkeley, CA: Apress, 2018, pp. 355–357.
[19] P. W. Webb, “Thermal imaging of electronic devices with low surface emissivity,” *IEE Proc. G Circuits Devices Syst.*, vol. 138, no. 3, pp. 390–400, Jun. 1991, doi: 10.1049/ip-g-2.1991.0065.
[20] D. L. Blackburn, “Temperature measurements of semiconductor devices - a review,” in *Twentieth Annual IEEE Semiconductor Thermal Measurement and Management Symposium (IEEE Cat. No.04CH37545)*, 2004, pp. 70–80, doi: 10.1109/STHERM.2004.1291304.
[21] R. H. Hopper, I. Haneef, S. Z. Ali, F. Udrea, and C. H. Oxley, “Use of carbon micro-particles for improved infrared temperature measurement of CMOS MEMS devices,” *Meas. Sci. Technol.*, vol. 21, no. 4, p. 045107, Mar. 2010, doi: 10.1088/0957-0233/21/4/045107.
[22] J. Glover *et al.*, “Thermal Profiles Within the Channel of Planar Gunn Diodes Using Micro-Particle Sensors,” *IEEE Electron Device Lett.*, vol. 38, no. 9, pp. 1325–1327, Sep. 2017, doi: 10.1109/LED.2017.2731961.
[23] “InfraScopeTM Systems | QFI Corporation,” *InfraScope Temperature Measurement Microscope Systems*. [Online]. Available: http://www.quantumfocus.com/products-2/infrascopetm/. [Accessed: 18-May-2018].
[24] “InfrascopeThermalMapperXPUsersManual.pdf.” Quantum Focus Instruments, 2006.
[25] “Scientifica PatchStar Motorised Micromanipulator,” *Scientifica*. [Online]. Available: https://www.scientifica.uk.com/products/scientifica-patchstar-micromanipulator. [Accessed: 05-Jan-2020].
[26] “Transient-IR | QFI Corporation,” *Transient-IR MWIR High-Speed Temperature Trace Option*. [Online]. Available: https://www.quantumfocus.com/products-2/infrascopetm/high-speed-transient-hst-temperature-detection-microscopy/. [Accessed: 05-Jan-2020].

Chapter 4

IR micro-sensors:

This chapter provides a description of the microparticle infra-red sensor (MPIRS) method, using the carbon microparticle, which has a high and known emissivity. This helps to improve the accuracy of the temperature measurements made on the optically transparent thin semiconductor layer forming the micro-electro-mechanical systems (MEMS) micro-heater studied in this research work.

4.1. Introduction:

Chapter 3 discussed the experimental methodologies to thermally characterise MEMS based micro-heaters and electronic devices in general using conventional passive infra-red (IR) thermal microscopy. Conventional IR thermal measurements on highly reflective metallised surfaces (usually very low emissivity <0.1) and IR transparent semiconductor layers of electronic devices may lead to significant temperature errors (discussed in Chapter 3, section **3.1.3**). Although, Micro-Raman spectroscopy (as discussed in Chapter 2, section **2.3.2.3**) could be used for the detailed thermal measurement (high thermal spatial resolution) on semiconductor devices, the technique is not possible to be used for making the temperature measurements on highly reflective metallised surfaces and contacts. Furthermore, this technique requires a laser source to excite the device under test (DUT). Therefore, the laser can affect the measurement, and so is not a passive technique. At De Montfort University, an IR thermal point measurement has been developed using a carbon based MPIRS technology that overcomes some of the problems of performing IR temperature measurements particularly on IR transparent semiconductor devices and high reflectivity metals [1].

The effect of the background material on the emitted radiance measurement from the MPIRS, as a function of temperature, has also been investigated. This has enabled experiments to be reported in this thesis that calibrate the MPIRS emitted radiance as a function of temperature to high operating temperatures taking into account the effect of background radiation. In addition, the emissivity of the MPIRS was also measured, for the first time, to temperatures approaching 300 °C by eliminating the background radiance.

4.2. Description of the microparticle measurement technique:

In this technique, a high emissivity opaque spherical carbon microparticle is placed in temporary isothermal contact with the surface of the device (DUT) in which the temperature is to be measured. The spherical shape was chosen as it enabled a stable point contact with the surface of the DUT [2]. To make a temperature measurement using the MPIRS, the surface emissivity of the microparticle is first measured. This was done by measuring the radiance emitted by the MPIRS, using the Quantum Focus Instruments (QFI) IR microscope, at two known temperatures and then applying the standard two-temperature emissivity measurement approach (as already described in Chapter 3, section **3.1.2.2**). The QFI IR microscope takes the black body radiation values from a stored black body calibration (which is recalibrated by user on an annual basis) to provide a value of the surface emissivity. The measured surface emissivity of the MPIRS can then be used to determine a more accurate indication of the

temperature of the surface with which the MPIRS is in isothermal contact. In this measurement technique, the surface emissivity of the MPIRS is independent of the radiative surface properties of the DUT. The MPIRS has a small thermal mass and an estimated thermal time-constant of the order of micro-seconds which is very short compared with the image acquisition time of milliseconds [1] for QFI IR microscope. Therefore, a thermal equilibrium will be reached very quickly between the DUT surface and the MPIRS, enabling a more accurate temperature measurement to be made. The MPIRS can also be removed from a surface of the DUT without causing damage to the device. The schematic experimental arrangement of this technique is shown in Figure 4.1.

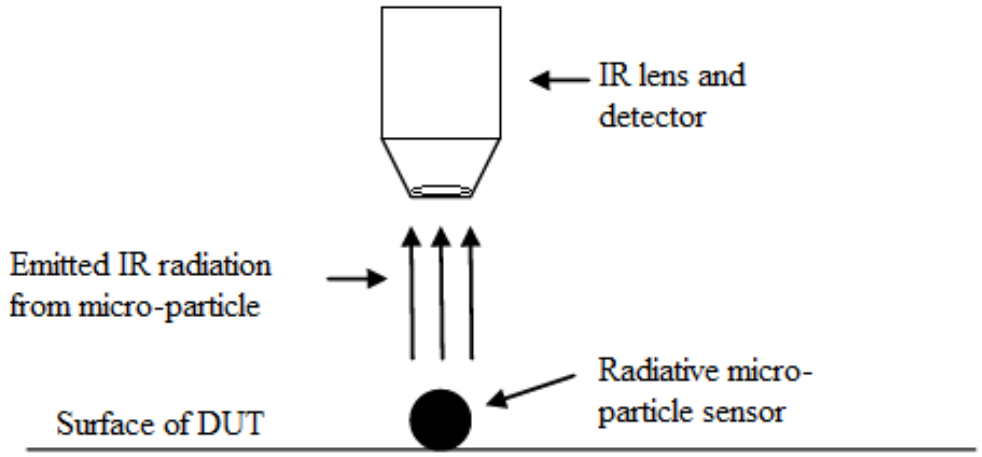

Figure 4.1: Schematic arrangement for IR thermal measurement using microparticle sensor technique.

The microparticle measurement technique offers the following advantages over conventional IR temperature measurements;

- The technique is not dependent on the surface emissivity of the device being measured but only on the surface emissivity of the MPIRS, which has to be initially measured. Therefore, temperature measurement accuracy will be independent of the surface emissivity of the DUT.
- A higher spatial resolution (limited to the spatial resolution of the IR microscope) is possible when compared to coating the DUT with a high emissivity paint, as an individual MPIRS (spherical) has a small area in contact isothermally with the surface of DUT, thus limiting lateral heat spreading [3]. Maximum spatial resolution can only be achieved using MPIRS with a diameter similar to the spatial resolution of the microscope.

One potential problem using the MPIRS technique is that carbon is an electrically conductive material and may cause a problem when used in electrically biased semiconductor electronic devices [4]. However, most electronic semiconductor devices are electrically passivated using a non-conductive film [5], for example; silicon dioxide (SiO_2) or silicon nitride (Si_3N_4), and therefore positioning the conducting carbon microparticle on a passivated DUT should not present any measurement problems. It is also interesting to note that some of these passivation films may well enhance the surface emissivity of the device [6].

The technique enables a point thermal measurement using a single carbon microparticle sensor [7], and hence, accurately knowing the surface emissivity of the microparticle is very important. To improve the thermal precision of the MPIRS it can be moved across the surface of the DUT more accurately using a micro-manipulator. Using this technique, precise thermal profiles can be obtained. However, the measurement will no-longer be in real time and so care needs to be taken to minimise any changes in the environment surrounding the DUT.

4.2.1. Microparticle sensor manipulation:

In this research work, spherical shape amorphous carbon MPIRS particles with a diameter between 2µm to 50µm were used. These were purchased from commercial suppliers (Sigma-Aldrich and Alfa Aesar). The MPIRS can be used in different ways to make the surface temperature measurement. An individual MPIRS can be placed on the area of interest (for example, at a hotspot location, which can be first identified using conventional IR thermal microscopy) using a pick and place method as shown in the schematic Figure 4.2, or a collection of microparticle sensors with an appropriate range of diameters can be scattered over the area of interest on the surface of the DUT, if exact positioning is not important [2]. However, for detailed thermal measurements at a specific location (for example, temperature profiling within the channel of planar Gunn diode) [8], the preferred method would be to use a calibrated single MPIRS placed in isothermal contact with the device surface.

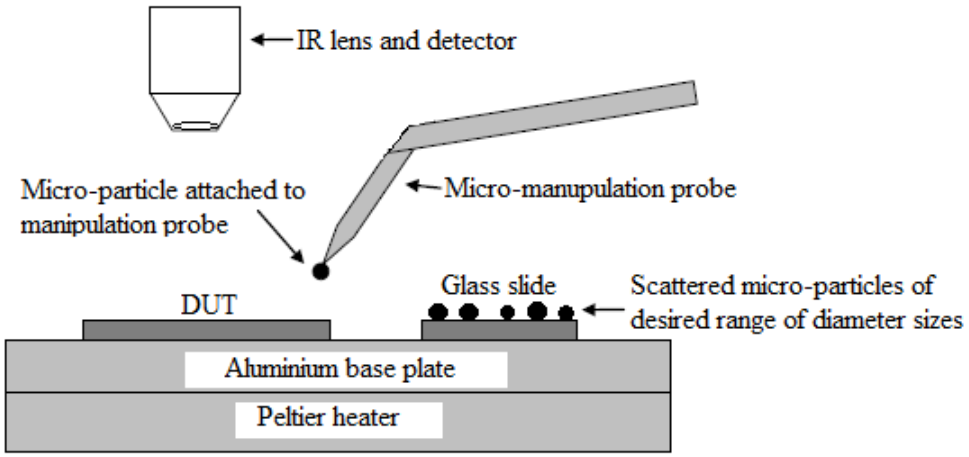

Figure 4.2: Schematic arrangement to pick and place the carbon MPIRS.

To accurately pick and place, and to move a MPIRS across the surface of the DUT, a micro-manipulator can be used. The micro-manipulator used in De Montfort University measurement set-up was supplied by Scientifica. The unit has been mechanically configured with the QFI Insfrascope-II thermal microscope (shown in Figure 4.3). It was experimentally found that the MPIRS naturally adhered to the micro-manipulator probe (Hunter Scientific injection glass pipettes) by naturally occurring electrostatic and van-der-Waals forces. Hence, a single microparticle can be effectively transferred to the point on the surface of the DUT where the temperature is to be measured [9], [10]. The process of picking up and transferring the microparticle to another point on the surface of the DUT will require further development to improve repeatability.

Figure 4.3: Scientifica micro-manipulator with manipulation probe.

To conduct a detailed thermal analysis using this method, the reliable and precise manipulation of a single microparticle is essential. Initially the microparticle has to be picked up by the manipulation probe. Therefore, to optimise the picking up process, tests were undertaken by scattering the microparticles onto different substrates (Al, Cu, Si, Ge and glass). Figure 4.4 shows a photograph of the carbon microparticles scattered on the surface of the glass substrate.

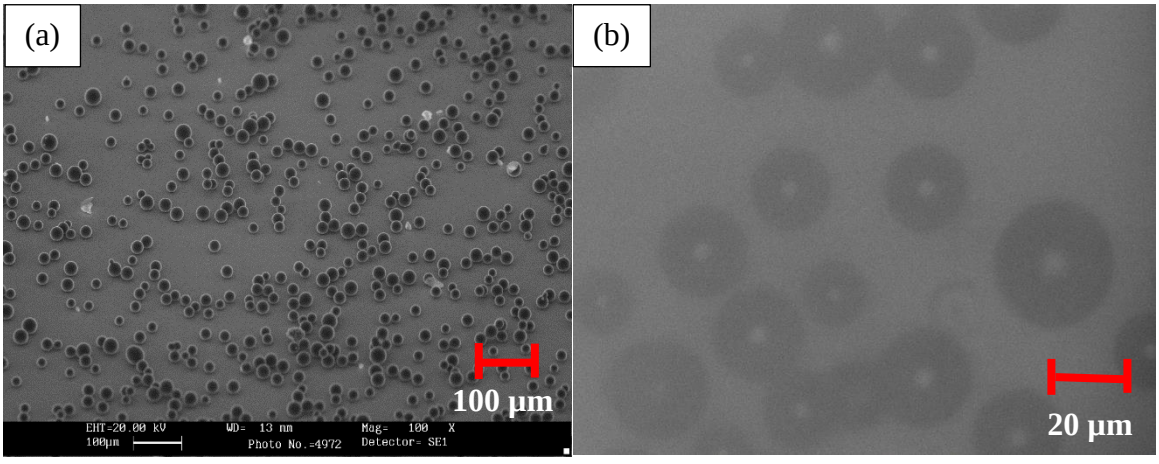

Figure 4.4: Figure showing the carbon microparticles scattered on the surface of the glass substrate (a) SEM image (Non spherical white substances are foreign particles) (b) an optical image.

It was possible to pick a target carbon microparticle using the manipulation probe very easily from a number of distributed particles scattered on the surface of a glass substrate when compared to the surface of substrates made from other materials. This is an important observation when manipulating a single carbon microparticle using pick and place method (as shown in Figure 4.2). An optical image showing the MPIRS attached to a glass manipulation probe is shown in Figure 4.5 (a). The above observation could be due to the glass substrates and the manipulation probe both being electrically non-conductive.

It is more difficult to pick the microparticles if the substrate or the manipulation probe is manufactured from a material providing some electrical conductivity. Carbon microparticles will have an electric charge which will be discharged when touching them with a manipulation probe manufactured from a material which is electrically conductive making it difficult for the microparticle to adhere to the manipulation probe.

Additional research to control the electrostatic attractive force between microparticle and manipulation probe tip will be required and is outside the scope of the present research. This could be an area of future research work to develop a more precise and reliable micro-manipulation process.

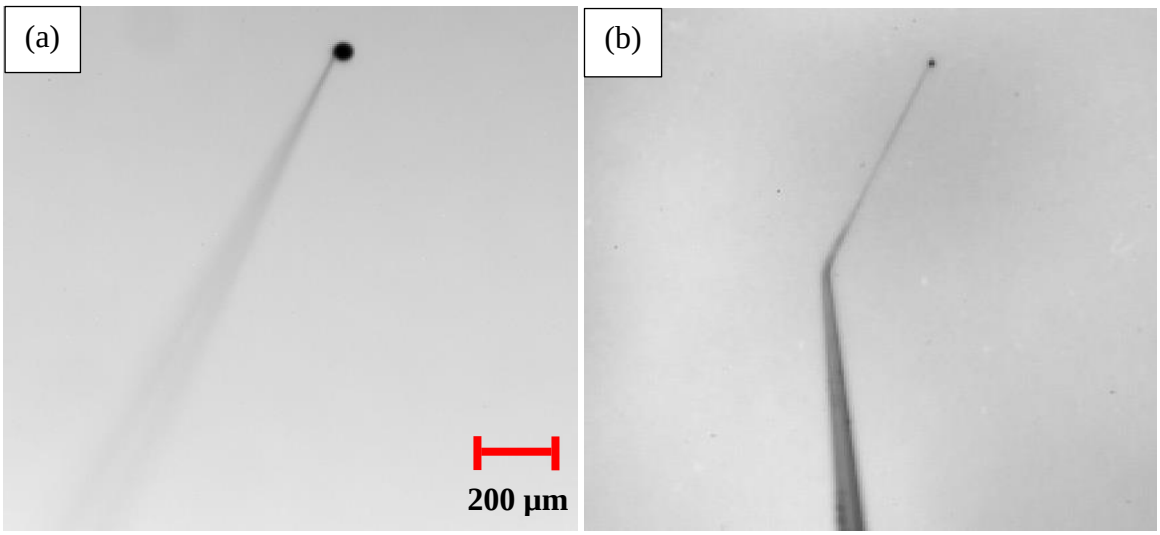

Figure 4.5: Optical image showing (a) Microparticle attached to the tip of the manipulation probe (b) manipulation probe bend.

In order to drop the MPIRS from the manipulation probe tip, it is required to touch at a desired location on the surface of the DUT and then pull the tip aside (as shown in Figure 4.6) so only a weak adhesive force acts on the particle enabling the particle to attach to the device surface [11]. The particle is retained on the DUT surface by the means of van-der-Waals force. Microparticle, once placed on the surface of DUT, can be manipulated, repositioned and removed as required without causing electrical or physical damage to the DUT. The manipulation probe was also inclined slightly (at ~ 30° angle to the vertical as shown in Figure 4.5 (b)) so that it would bend easily without breaking and absorb force from any over displacement of the probe in the process of capturing and manipulating the MPIRS.

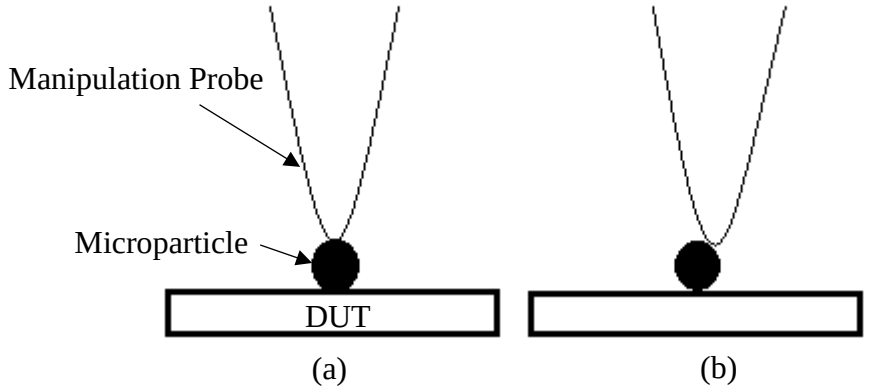

Figure 4.6: Figure showing the schematic of the MPIRS placed on the surface of DUT. (a) MPIRS touching on the surface of the DUT (b) figure showing the manipulation probe tip touching the side of the MPIRS.

4.3. Theoretical background on radiance measurements of microparticle IR sensors:

The emissivity measurement (the emissivity measurement method is fully described in Chapter 3, section **3.1.2**) of the MPIRS depends on accuracy of the IR microscope and measurement method, and on the spurious radiation emitted by the material surface where the MPIRS is placed i.e. its background surroundings. In the emissivity calibration process, this spurious radiation must be considered, as there will be a difference between the magnitude of true emitted radiation from the surface of MPIRS and the measured radiation using the microscope as it will include radiation emitted from the background surface.

The emissivity of the MPIRS is obtained by comparing the magnitude of the radiation emitted by its surface (R_p) to that of the radiation emitted by a black body (R_b) at the same temperature and same frequency bandwidth. Thus, the emissivity of the MPIRS can be expressed as;

$$\varepsilon = \frac{R_p}{R_b} \qquad \textbf{(4.1)}$$

The application of this formula depends on a number of factors including the experimental equipment (QFI microscope IR detector) and the surrounding background radiation [12], [13].

Assume that the MPIRS is placed on the surface of the DUT and the IR microscope is focused on the microparticle, where;

Emissivity of the microparticle is ε_1

Emissivity of the background surface is ε_2

Surface area of the microparticle is A_1

Area of the background surface is A_2

Defocused parameter is Q

Microscope configuration factor (gain, solid angle etc.) is K, and assume it is constant for any particular objective lens of the IR microscope.

Hence, the total measured radiation signal (R_m) received by the IR detector can be written as;

$$R_m = \sigma K\ [\ A_1 \varepsilon_1 T^4 + \ Q\varepsilon_2\ (A_2 - A_1)\ T^4] \qquad \textbf{(4.2)}$$

Where, σ is Stefan constant and T is the temperature. Therefore, at uniform temperature,

$$R_m = \sigma K T^4\ [\ A_1 \varepsilon_1 + \ Q\varepsilon_2 (A_2 - A_1)\ ] \qquad \textbf{(4.3)}$$

If it is assumed that the background material surface on which the MPIRS has been placed is a black body surface, then, for this particular set-up, σK can be found as it is a straight-line equation.

$$R_b = \sigma K T^4 A_2 \qquad \textbf{(4.4)}$$

Of the form,

$$y = mx \qquad \textbf{(4.5)}$$

A plot of the black body radiance (R_b) against $T^4 A_2$ will give the constant for microscope/objective ($\sigma K = Z$) from the gradient.

As,

$$R_m = ZT^4\ [A_1 \varepsilon_1 + \ Q\varepsilon_2 (A_2 - A_1)] \qquad \textbf{(4.6)}$$

And knowing Z, A_1 and A_2, ε_1 and ε_2, it will be possible to calculate Q,

Therefore, the equation **(4.3)** become,

$$R_m = R_b\ [\ A_1 \varepsilon_1 + \ Q\varepsilon_2 (A_2 - A_1)\ ] \qquad \textbf{(4.7)}$$

$$R_b A_1 \varepsilon_1 = R_m - R_b\ [\ Q\varepsilon_2 (A_2 - A_1)\ ] \qquad \textbf{(4.8)}$$

Assuming the temperature of the IR detector and the room temperature remain constant during the experiment, the external background surrounding radiation [$R_0(\lambda)$] reaching the IR detector remains constant and can be considered to be independent of temperature. Hence, the radiation emitted by the microparticle IR sensor (R_p) will be;

$$R_p = R_m - R_b\ [\ Q\varepsilon_2 (A_2 - A_1)\ ] + \ R_0(\lambda) \qquad \textbf{(4.9)}$$

The result show the radiation from the microparticle is dependent on the background surface material.

4.4. Experiments and discussion:

4.4.1. Initial tests to assess the effect of background material on emissivity measurements:

The QFI Infrascope-II thermal microscope (shown in Figure 3.5, in Chapter 3) was first calibrated using a black body source (shown in Figure 4.7 (a)). This was covered by a very low surface emissivity aluminium ($\varepsilon \approx 0.1$) shield, and therefore the effect of the background radiation was minimised. The black body source covered with an aluminium shield was provided by QFI. The black body radiation was measured through the ~5mm diameter window cut in the top surface of the aluminium shield, see Figure 4.7 (b).

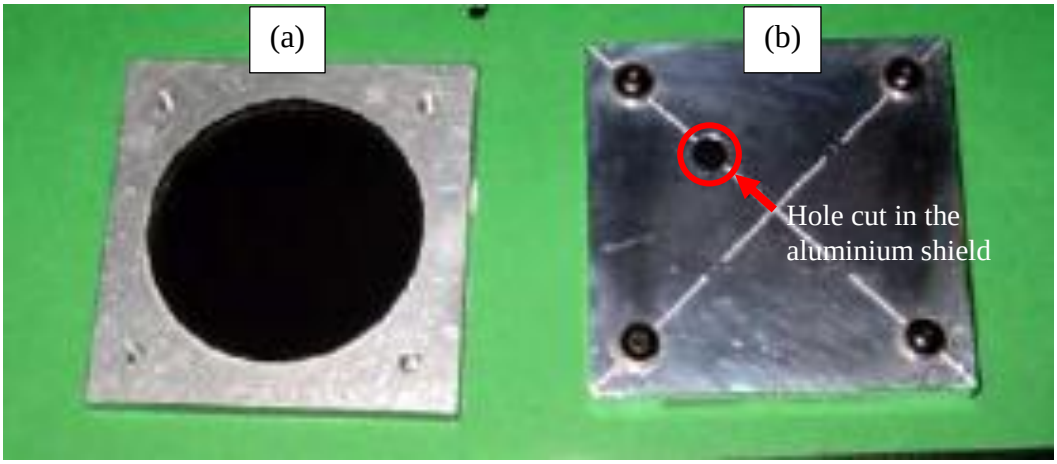

Figure 4.7: Black body calibration kit provided by QFI (a) figure showing the surface of the black body source (b) figure showing the hole cut in the aluminium shield.

A preliminary set of experiments was then carried out to determine the effect of surrounding background radiation on the measurement of a high emissivity material. Scotch brand 33+ vinyl electrical black tape was used as the material, as it has a known and high surface emissivity of 0.95 [14], [15]. The surface emissivity of the black tape was measured by placing it on the base-plate heater under the QFI IR microscopy (×25 objective) and measuring its emissivity at different base-plate temperatures (from approximately 70 ºC to 120 ºC). The tape was placed on both low emissivity background (aluminium base-plate, $\varepsilon \approx 0.1$) [16] as well as a much higher emissivity background (black tape, $\varepsilon \approx 0.95$). The two-temperature emissivity method (described in Chapter 3, section **3.1.2.2**) was used to measure the emissivity where the two radiance images were taken with a temperature difference of 30 ºC. The surface emissivity measurement results are shown in Figure 4.8 (the results are also provided in a table in Appendix – 4A).

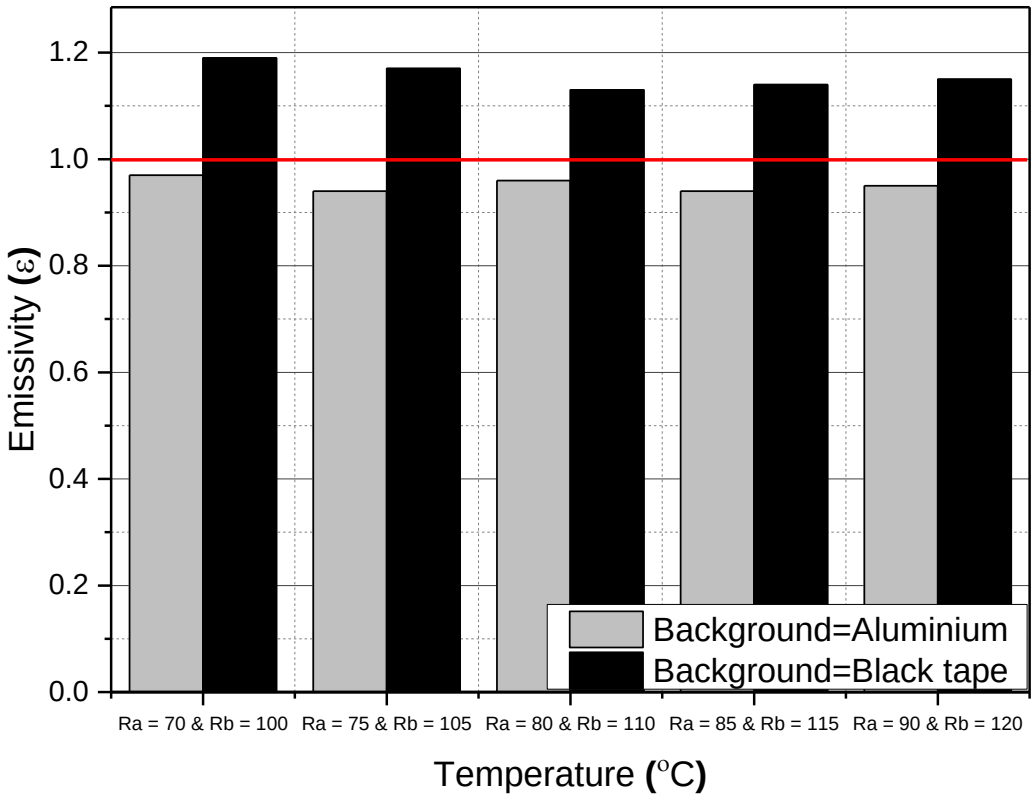

Figure 4.8: Emissivity measurement results on a black tape when placed on two different background. Red line represents emissivity of a perfect black body (ε = 1).

The results show the measured emissivity of the vinyl black tape is (average value, ε = 0.952) almost identical to the published value (0.95) when placed on a very low surface emissivity background material. However, it was found that, the measured emissivity of a black tape is above 1 when measured by placing on very high emissivity background material, therefore showing some error in the measurement. This preliminary work indicates that the background surface radiation will have an influence on the value of the surface emissivity of the DUT being measured, suggesting the DUT should always be placed on a very low emissivity background material (for example, aluminium base-plate as shown in Figure 3.1, in Chapter 3) for the measurements using the IR microscopy to minimise error in the measured temperature.

4.4.2. Effect of microparticle diameter size on radiance measurements:

Before investigating the effect of background radiation on the value of the surface emissivity of the MPIRS, some preliminary work was undertaken to look at the effect of diameter of the MPIRS on radiance measurements. It has been observed the diameter of the MPIRS has an effect on the magnitude of the IR radiation emitted from its surface area, this could lead to an error in the measured temperature [2]. The reason for this can be argued as follows: the IR microscope system tries to average the received radiance level from 9 neighbouring pixels rather than one, which will cover the surface area of ~81μm^2 (the spatial resolution is 3μm when using ×25 lens objective therefore the smallest area resolved by the microscope is approximately 9μm^2). The surface area of a 10μm diameter particle will be approximately 79μm^2 assuming that the microscope has a depth of focussed field of

approximately 5µm. Therefore, when the MPIRS with a diameter of less than 10µm is used on a surface with a low emissivity background, the radiance recorded by the microscope will decrease. Hence the microscope will be recording a level of radiation from an area larger than the particle surface area and the low-level background surface radiance around the MPIRS will also contribute, thereby reducing the surface radiance. This effect becomes more dominant with the smaller diameters of the MPIRS. There is also a further argument, as the diameter of MPIRS decreases to less than 2µm, then the particle diameter is going to become comparable to the wavelength of the emitted IR radiation which may lead to a quantum exclusion effect (longer wavelengths no-longer emitted). Neither of the above effects would be seen in MPIRS particles which have diameters greater than 10µm [2].

An experiment was carried to ascertain how the radiance from a MPIRS decreases as the diameter of the particle is decreased. A number of particle with diameters between 4µm to 50µm was deposited onto a uniformly heated aluminium plate (low background emissivity and therefore a low level of surface background radiation) which was held at a constant temperature of ~ 85 °C. The radiance emitted from each MPIRS was measured and plotted as a function of MPIRS diameter and shown in Figure 4.9. The results show the measured radiance from individual microparticles decreases substantially, if the diameter of the MPIRS is less than 10µm.

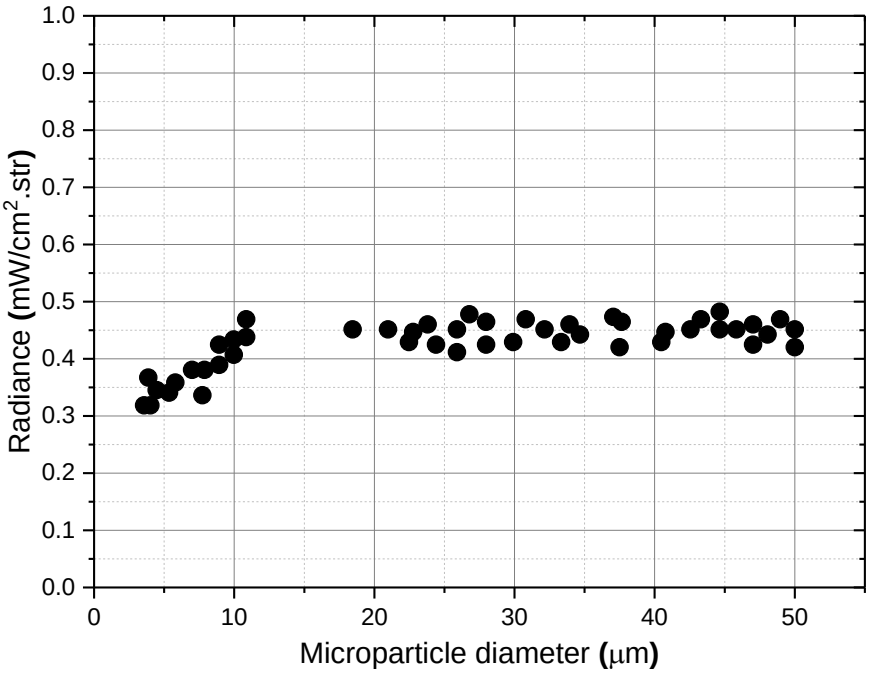

Figure 4.9: Effect of MPIRS diameter size on emitted IR radiation measured at constant temperature of ~ 85 °C.

To support the findings as shown in Figure 4.9, the experiment was repeated where the radiance emitted by two large size microparticles (20µm and 45µm in diameter) were measured at different operating temperatures. Figure 4.10 shows the radiance emitted from each microparticle as a function of temperature and shows larger size microparticles (with a diameter greater than 10µm) emit very similar radiance levels, for any given temperature.

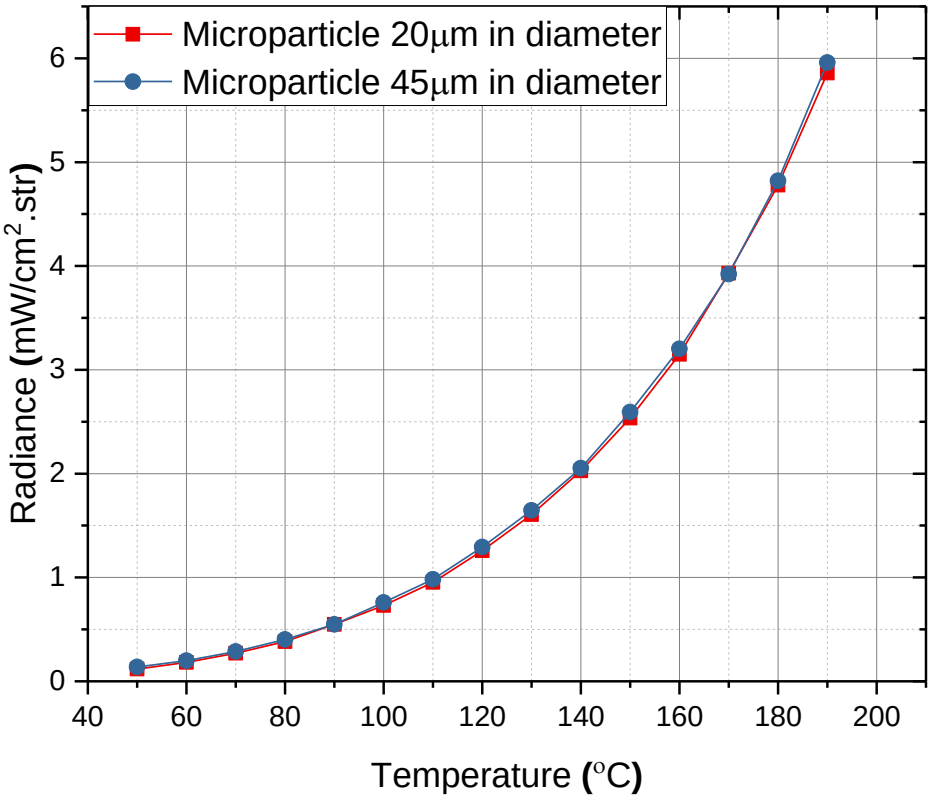

Figure 4.10: Plot comparing the level of radiance emitted by different size MPIRS as a function of temperature.

4.4.3. Effect of background surface on the radiance measurements of microparticle sensors:

A set of experiments was carried out to look at the effect of background surface radiation on the radiance calibration of MPIRS. To experimentally determine the effect of the background material surface emissivity has on a MPIRS the following experiment was set-up. A single MPIRS (diameter size ~22μm) was placed using the micro-manipulation process (as described in section **4.2.1**) onto each of the following; (i) a very low emissivity material (6mm thick polished aluminium block, ε=0.06, and a 2mm thick polished copper block, ε=0.07), and on a material (ii) with a higher surface emissivity (270 μm thick Si wafer, ε=0.56), and finally on a material (iii) with a very high emissivity (1mm thick glass slide, ε=0.9) [16] respectively. An example of the deposited MPIRS on the surface of the polished aluminium base-plate, including its IR radiance image are shown in Figure 4.11 (a) and (b) respectively.

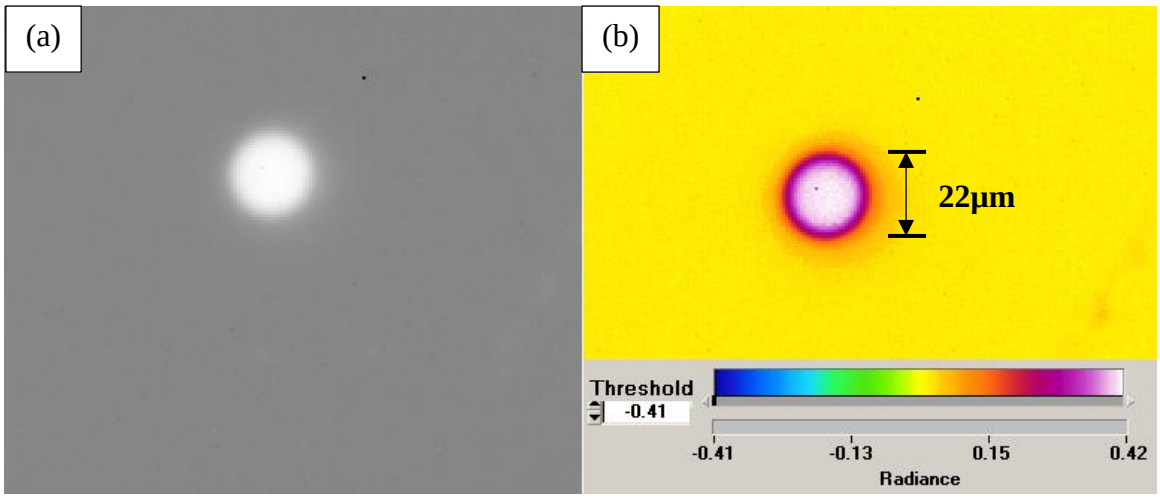

Figure 4.11: MPIRS deposited onto the surface of Al block (a) an optical image measured using ×25 lens (b) an IR radiance image measured at a temperature of 80 °C.

In this experiment, the level of IR radiation emitted by the deposited carbon MPIRS was measured using QFI IR Infrascope at different Peltier base-plate temperatures (from approximately 40 °C to 130 °C). Figure 4.12 shows the level of emitted radiation from the surface of the MPIRS when placed on different background materials (Al, Cu, Si and glass) and then compared with black body radiance over the same temperature range and for the same spectrum of wavelengths.

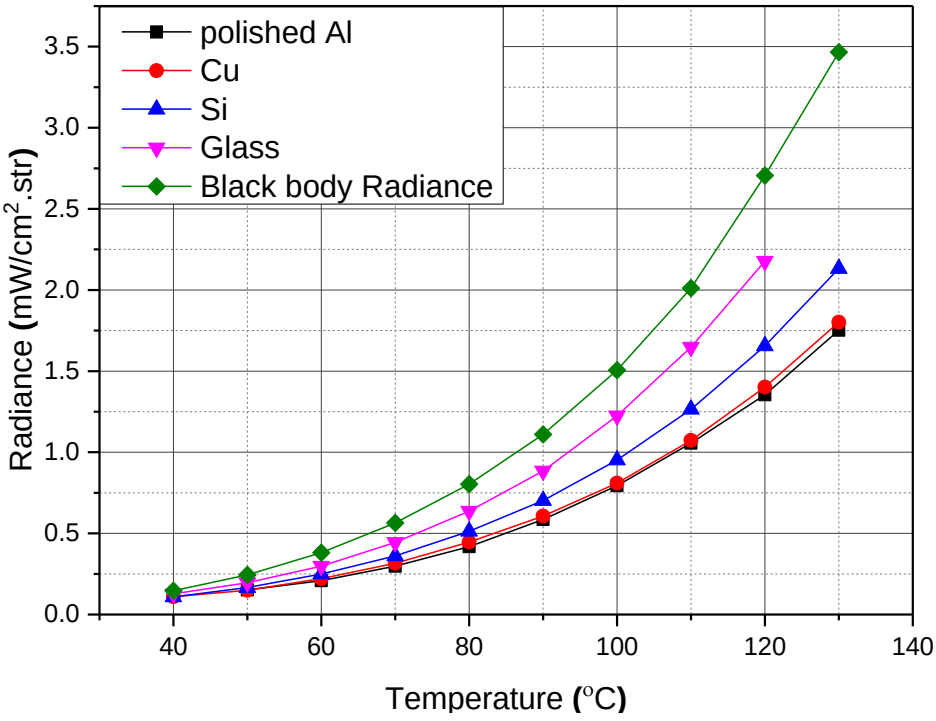

Figure 4.12: Emitted radiance level at different operating temperatures from the surface of carbon microparticle (~22 µm in diameter) deposited on different emissivity background materials and compared with black body radiance measured.

The radiance measurement results indicate the temperature of the MPIRS is dependent on the temperature of the background, and also on the material surface emissivity of the

background material. Materials with highest surface emissivity (for example, glass substrate) gave the highest levels of background radiance. This result suggests to obtain reasonable measurement accuracy, the MPIRS calibration would be best carried out on materials with very low emissivity (will be discussed in section **4.4.7**).

The effect of highly IR transparent semiconductor materials (eg, Si and GaAs) on the temperature measurement of the MPIRS will be further investigated and will be discussed later in the chapter.

4.4.4. Emissivity measurements of a microparticle IR sensor:

To fully confirm the background material surface emissivity has an effect on the MPIRS emissivity measurements, further emissivity measurements were made on a carbon microparticle sensor (40µm - 47µm in diameter) deposited again on substrates with different surface emissivity. For this experiment, the emissivity of the different substrates were first measured, and compared with published values [16], [17], [18], [19], [20], [21] (results are shown in Table 4.1). A single MPIRS was then deposited onto the surface of each of the different substrates using the Scientifica micro-manipulation probe (Figure 4.3). The surface emissivity measurement of both the substrate and the MPIRS were carried out using the two-temperature approach (described in Chapter 3, section **3.1.2.2**), where the radiance measurements were captured at two base-plate temperatures of 70 °C and 100 °C, respectively.

Table 4.1: Table showing the effect of background surface emissivity has on the emissivity measurements of microparticle IR sensor.

Background surface material	Measured surface emissivity values of background material	Published surface emissivity values of background material	Emissivity of deposited MPIRS on the background substrate
Polished Aluminium (Al)	0.07	0.09 [16], [17]	0.57
Gold (Au)	0.11	< 0.1 [16], [17]	0.58
Copper (Cu)	0.23	0.26 [17]	0.60
Sapphire	0.33	0.2 - 0.4 [16], [18]	0.64
Alumina (Al_2O_3)	0.3	0.2 - 0.3 [17]	0.63
Germanium (Ge)	0.28	0.26 [19]	0.63
Silicon (Si)	0.56	0.39 [19]	0.79
Gallium Arsenide (GaAs)	0.74	0.1 - 0.3 [20], [21]	0.87

From the experiment it is seen that the microparticle's surface emissivity depends on the background material surface emissivity. It is interesting to note that in Table 4.1, with low surface emissivity background materials ($\varepsilon < 0.35$), the measured emissivity of the MPIRS is 0.605+/- 0.035 (the resulting error in the surface temperature will be very small, ±1.5 %). This is believed to represent the true value of the surface emissivity of the MPIRS (this will be further verified in section **4.4.7**) as the background radiation and any subsequent reflections will contributed very little radiation to the camera lens.

However, on semiconductor materials (Si & GaAs) which have an apparent high emissivity ($\varepsilon > 0.55$), the measured surface emissivity of the MPIRS is higher than its actual value. This highlights the need to calibrate the surface emissivity of the MPIRS on a low emissivity background (e.g., highly polished Al surface) rather than measuring its emissivity on the surface to be measured, for example, a semiconductor device which is highly transparent to IR radiation.

After the emissivity of the MPIRS is calibrated by placing it onto a very low surface emissivity background, it can then be transferred onto any material surface of the DUT (using the micro-manipulation process described in section **4.2.1**). The calibrated MPIRS is then used to obtain a thermal profile as the measured emissivity of the MPIRS is independent to the radiative surface properties of the DUT.

4.4.5. Initial temperature measurements using microparticle IR sensor:

A set of experiments was also carried out to check if the IR temperature measurements made on deposited MPIRS could be used to track the ambient temperature of the background surface. A single MPIRS (size ~22 μm in diameter) was placed onto the surface of polished aluminium base-plate (6mm thick). A K-type thermocouple was attached to aluminium base-plate in order to provide an indication of the background surface temperature. The emissivity of the MPIRS was measured using the two-temperature emissivity technique, with two radiance images captured at 65 °C & 95 °C respectively. The Peltier heater was used to increase the surface temperature of an aluminium base-plate from temperatures ranging between 50 °C to 130 °C. At each temperature point, the ×25 lens of an IR microscope was used to record the temperature of the MPIRS deposited onto the surface of the aluminium base-plate. A result showing a comparison between measured MPIRS temperatures using IR microscopy and recorded thermocouple temperatures are shown in Figure 4.13 (The results are also provided in a table in Appendix – 4B).

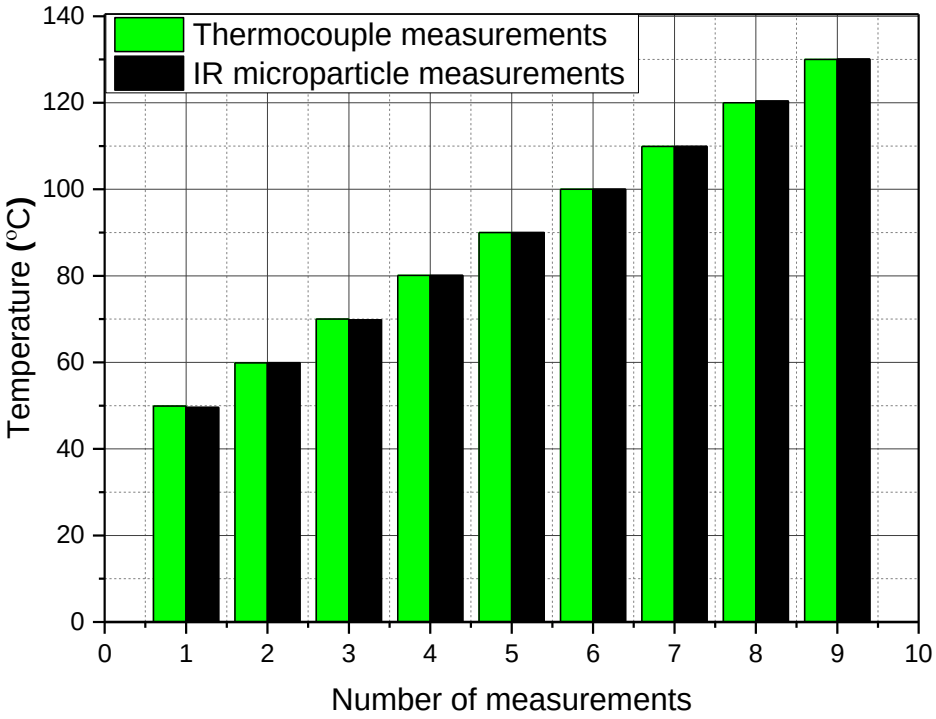

Figure 4.13: Comparison between temperature measurements using thermocouple and carbon microparticle IR sensor.

The results show the temperature measurements made on the deposited MPIRS were in good agreement (within ± 0.5 °C) with the temperature results recorded using an attached thermocouple. These results indicate that the MPIRS technique is capable of providing an accurate surface temperature measurement on isothermally heated structures. The technique has been used to thermally characterise the CMOS based MEMS micro-heaters and the results will be discussed in Chapter 6.

4.4.6. Radiance calibration of microparticle sensors at high temperatures:

An improved base-plate heater was developed to heat the MPIRS to higher temperatures (in excess of ~ 300 °C) to enable its radiance calibration (previously they have been only calibrated to a temperature approaching 130 °C) as a function of temperature. The revised base-plate heater used a temperature controlled element of a soldering iron. A circular hole (7mm in diameter) was cut through the aluminium base-plate block and the tip of the soldering iron was inserted through that hole to heat the aluminium block and to provide the uniform temperature. A calibrated K-type thermocouple was attached to the aluminium block to monitor the temperature of the base-plate heater. A photograph of the base-plate heater assembly is shown in Figure 4.14.

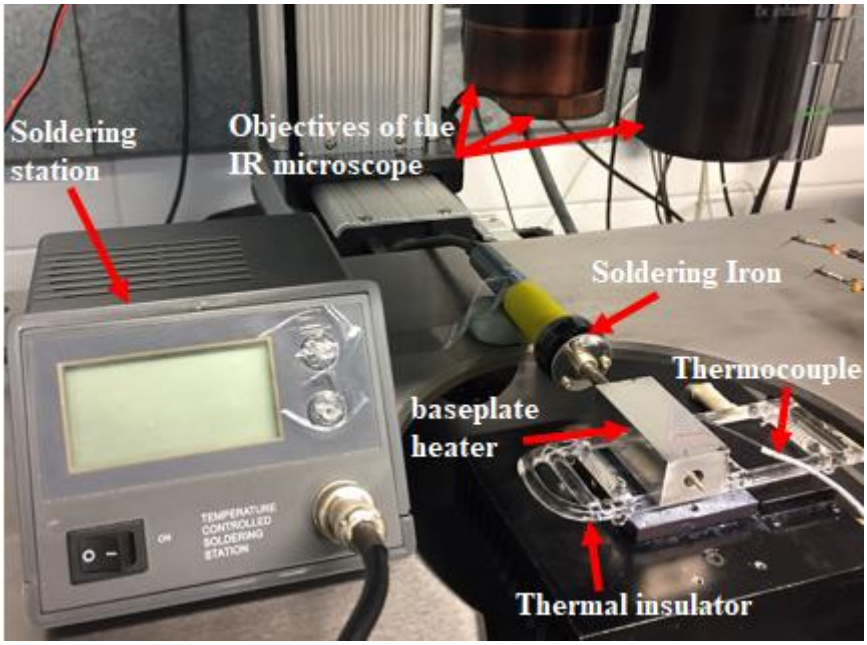

Figure 4.14: Figure showing the base-plate heater assembly positioned underneath the IR microscope.

Experiments were carried out, for the first time, to calibrate the MPIRS radiance to higher temperatures approaching 310 °C. The top surface of the base-plate heater (shown in Figure 4.14) was highly polished to reduce the error due to background surface radiance. A MPIRS was placed onto the highly polished aluminium base-plate heater using the micro-manipulation process as described in section **4.2.1**. The temperature of the base-plate heater was increased from approximately 140 °C to 310 °C and the emitted radiance level from the surface of the MPIRS was measured using the QFI thermal microscope. The radiance measurements at high temperatures were made on four MPIRS samples (one at a time). The ×25 lens was used for imaging and measuring the emitted radiance from the MPIRS as a function of temperature. The results are shown in Figure 4.15 (The results are also provided in a table in Appendix – 4C). The experiment showed that the level of emitted radiance as a function of temperature from all four MPIRS was very similar. As the base-plate heater temperature is increased from 140 °C to 310 °C, the average emitted radiation level from the surface of MPIRS rises from 2.023 to 37.33 mW/cm^2.str.

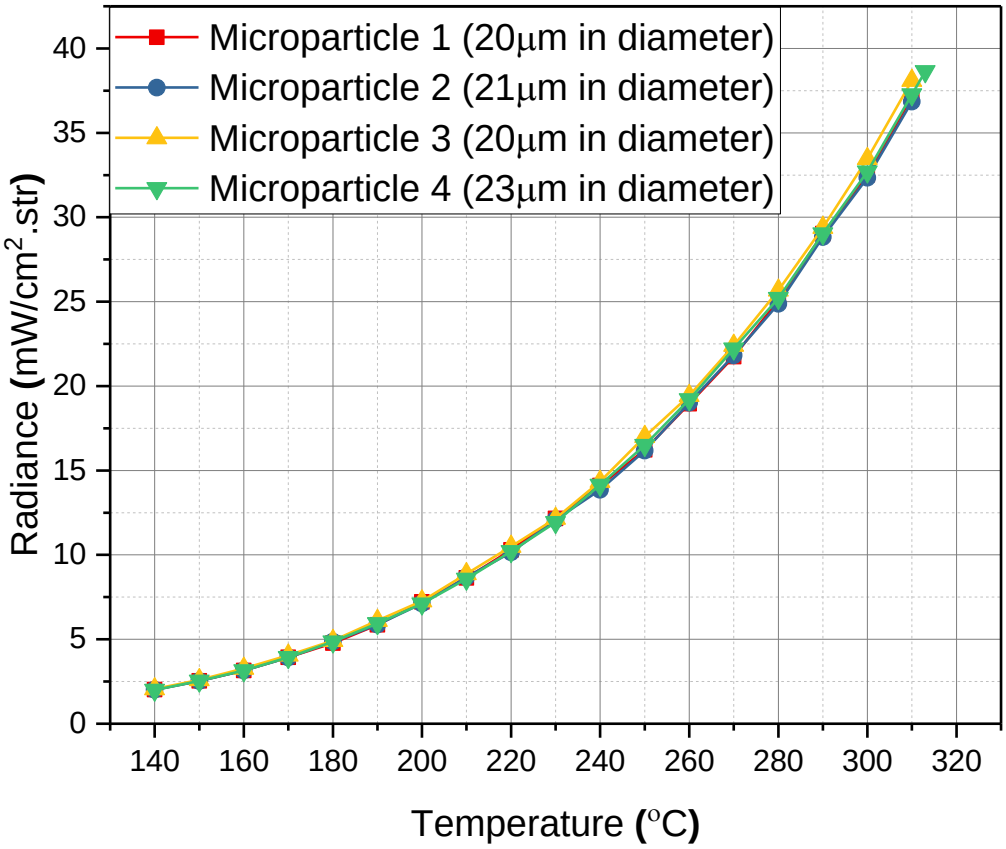

Figure 4.15: Emitted radiance level from the surface of MPIRS deposited on highly polished Al surface and calibrated as a function of temperature.

4.4.7. Microparticle IR sensor emissivity calibration:

A further experiment was carried out and for the first time to determine the surface emissivity of the MPIRS taking into account the emitted surface background radiance, to temperatures approaching 300 °C. To minimise background radiance the MPIRS was placed on a low emissivity surface. For this experiment, the MPIRS (~ 45μm in diameter) was manipulated onto the surface of a highly polished aluminium heated base-plate. Initially, the radiance emitted from the surface of MPIRS was measured at different base-plate temperatures (from 50 °C to 300 °C) using the ×25 lens objective. To measure the level of background surface radiance at the same temperatures, the IR Infrascope head was moved along the *X*-*Y* plane (keeping the same focal length with reference to the surface of MPIRS), until the MPIRS was out of the field of view. Therefore, the measured emitted radiance will only be as a result of the background material. Figure 4.16 shows the level of background surface radiance was low compared to the MPIRS radiance. However, it does show that the background radiance increases at elevated temperatures.

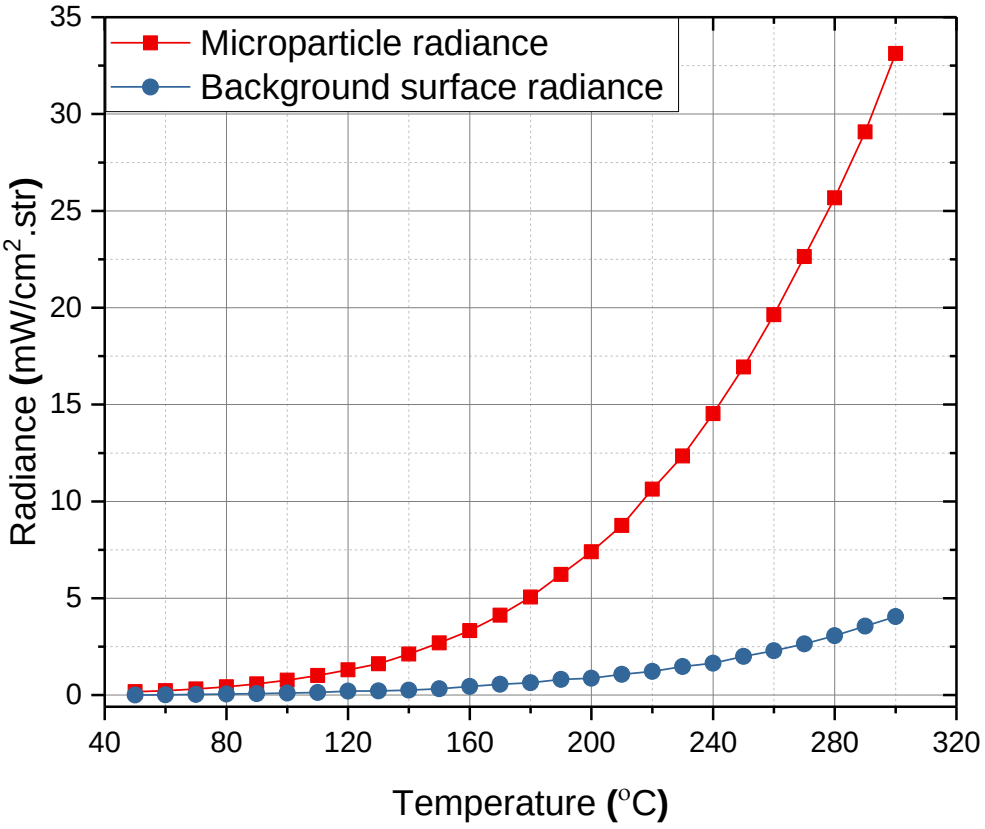

Figure 4.16: Figure showing the effect of background material surface radiance has on the microparticle sensor radiance at different operating temperatures.

To obtain a more accurate emissivity of the MPIRS particle, the emitted radiance of the MPIRS particle is required to be calibrated against the radiance emitted by a black body at the same temperature and over the same range of wavelengths.

The top surface of the highly polished aluminium base-plate heater was evenly painted with matt black paint. It was initially believed that the emissivity of the matt black paint was close to a black body source. To fully confirm this, the level of radiance emitted from black painted surface of the aluminium base-plate heater was compared with level of radiance emitted from the black body calibration kit (provided by QFI) at different temperatures (from 40 °C to 130 °C) and the results are shown in Figure 4.17. As can be seen from the results, the emitted radiation level from both the surfaces is almost identical over the measured temperature range. Hence, the matt black paint on the aluminium base-plate heater was used as black body source for the radiance calibration at higher temperatures (>130 °C).

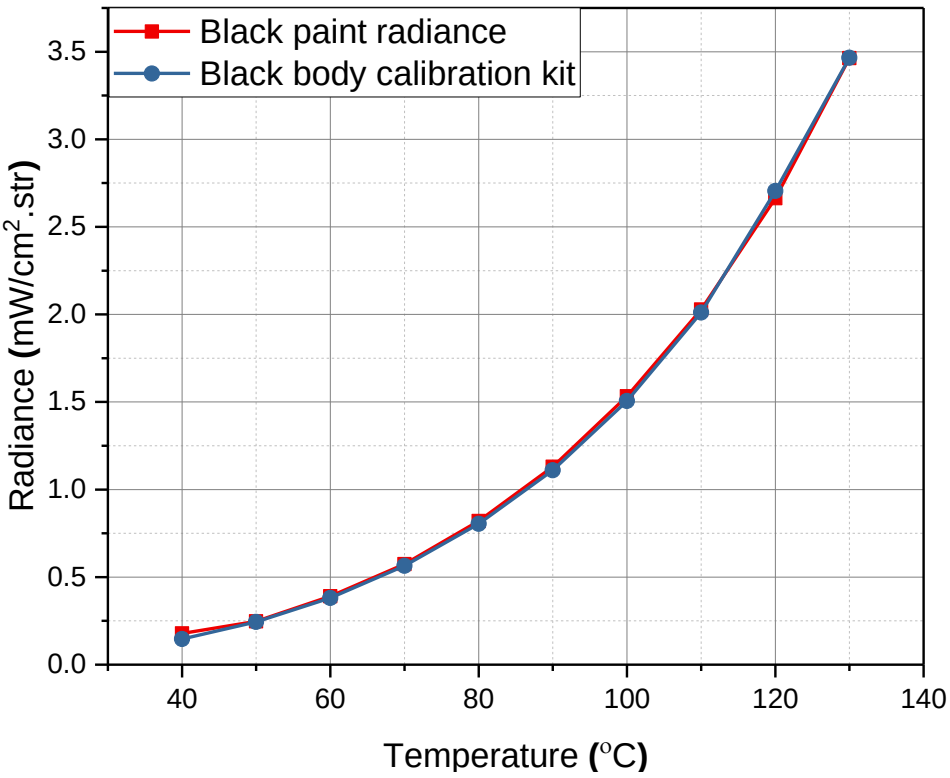

Figure 4.17: Figure showing the comparison between the emitted radiation level from the surface of matt black paint (painted on Al base-plate heater) and black body calibration kit.

To minimise the error due to the influence of spurious background radiance, a highly polished aluminium shutter was designed (shown in Figure 4.18). The black body source was covered with aluminium shutter and the whole assembly was positioned in a vertical alignment with the objective of the IR microscope, as shown in Figure 4.18.

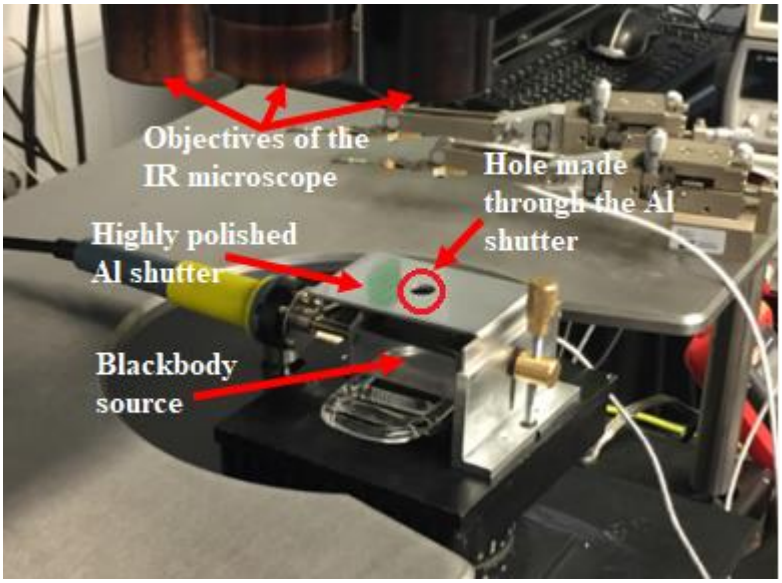

Figure 4.18: Black body source covered with highly polished aluminium shutter.

The level of emitted radiance by the black body source at elevated temperatures (>140°C) was measured (using a ×25 lens) through an approximately 5mm diameter window cut, made in the top surface of the aluminium shutter to the same dimensions as the hole in the aluminium shield provided by QFI (Figure 4.7 (b)) for consistency. To experimentally verify the effect of the spurious background radiance, the black body radiance measured using the aluminium shutter, was compared with the black body radiance measured without using the aluminium shutter and the difference in results as a function of temperature is shown in Figure 4.19.

To calculate an emissivity of the MPIRS at higher temperatures (>140 °C), taking into account the background surface radiance, the magnitude of the background material surface radiance (shown in Figure 4.16) was subtracted from the total detected radiance emitted by the surface of MPIRS. The level of emitted MPIRS radiance calculated by eliminating the background surface radiance was compared with black body radiance at the same temperatures and shown in Figure 4.19.

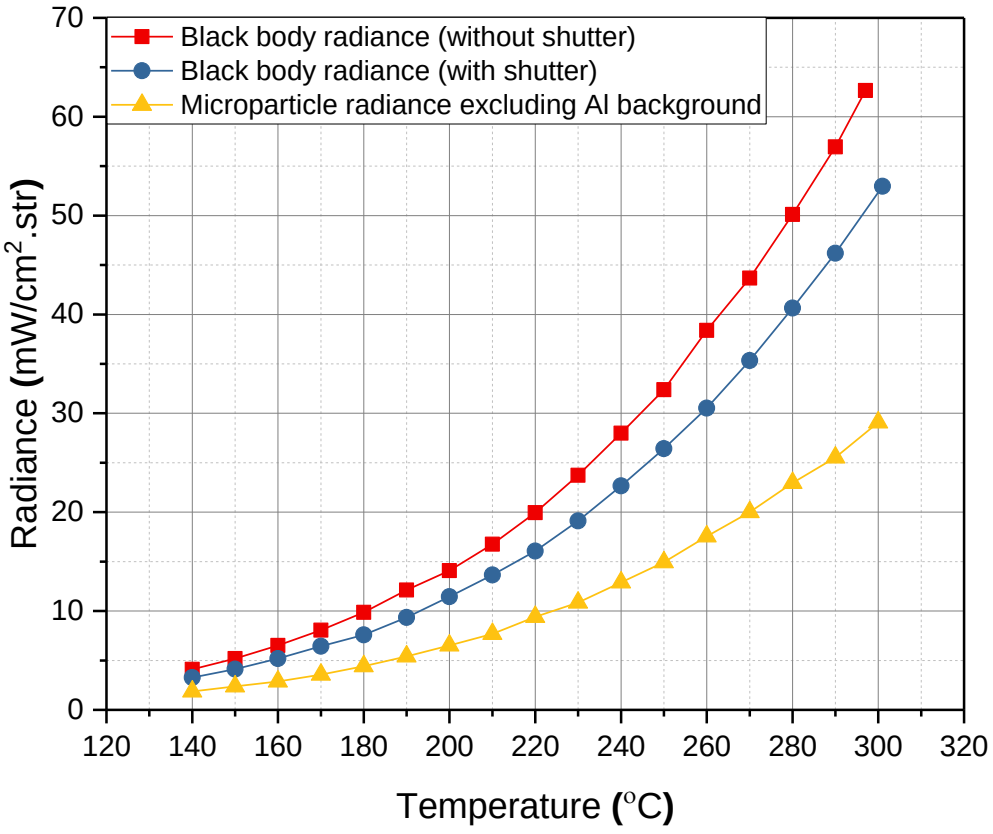

Figure 4.19: MPIRS radiance (calculated by eliminating aluminium background surface radiance) compared with the radiance emitted by the black body source at different temperatures.

The emissivity of the MPIRS was calculated from the results shown in Figure 4.19, using the equation **(4.10)**;

$$\varepsilon = \frac{R_p - R_{Al}}{R_{b0}} \qquad \textbf{(4.10)}$$

In equation **(4.10)**, R_p is the total detected radiance emitted by the surface of MPIRS, R_{Al} is the level of radiance emitted by the background aluminium surface, and R_{b0} is the black body radiance measured using the aluminium shutter.

The calculated (from the equation, **4.10**) emissivity of the MPIRS as a function of temperature to 300 °C is shown in Figure 4.20. The results indicate the emissivity of the MPIRS is around 0.6, which agrees well with the measured and stated value in section **4.4.4** of this chapter. By eliminating the background radiance the surface emissivity of the MPIRS is almost invariant with temperature up to 300 °C.

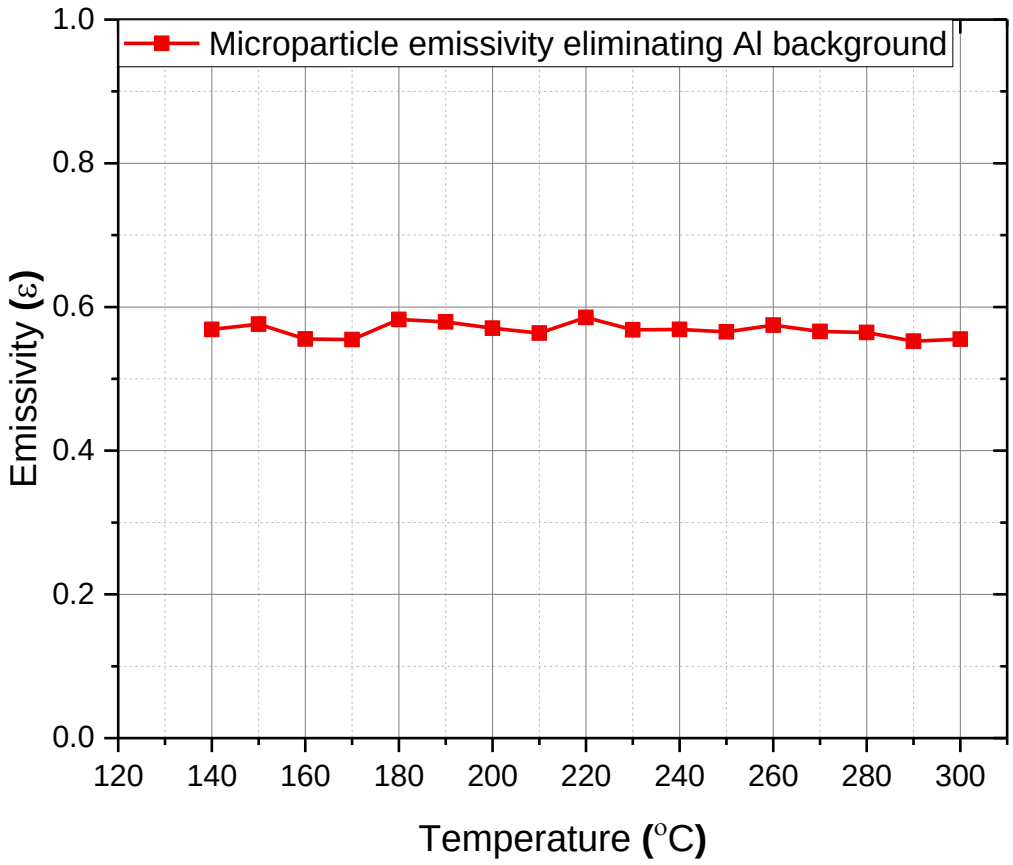

Figure 4.20: MPIRS emissivity measured by eliminating the background material surface radiance.

4.5. Conclusion:

In this chapter, the IR thermal measurement using a single MPIRS to improve the IR surface temperature measurement on transparent semiconductor and low surface emissivity materials has been discussed. To use a single MPIRS, glass substrates were shown to be a convenient surface to pick an individual microparticle with a help of manipulation probe and to place onto the surface of DUT. It has been shown that a MPIRS with less than 10μm in diameter may lead to an error in the measured temperature. This was further verified by measuring the temperature of the MEMS micro-heater using different diameter size MPIRS particles including sub-10μm diameter size, and the comparison of the temperature results will be discussed in Chapter 6.

The effect of the background surface on the emissivity measurement of the MPIRS was discussed, and for the first time, the MPIRS radiance has been calibrated to higher temperatures approaching 300 °C. In the calibration process there are advantages in placing the MPIRS on a low emissivity polished surface which can be taken into account. The measured surface emissivity of the MPIRS was found to be of the order of 0.6 and was almost invariant with temperature to 300 °C. Initially it was thought the carbon based MPIRS will emit IR radiation close to that of a black body and therefore have a high surface emissivity (> 0.9) but this work suggests that the actual emissivity of the MPIRS is around 0.6. This value agrees with previous work carried out by R. H. Hopper [4]. The MPIRS technique was used for thermal characterisation of the CMOS based MEMS micro-heaters used in gas sensing technology (a review of different types of the gas sensors requiring a miniature micro-heater technology will be discussed in Chapter 5), and the results will be discussed in Chapter 6.

4.6. References:

[1] C. H. Oxley, R. Hopper, D. Prime, M. C. Leaper, G. Evans, and A. Levick, "Probe propels IR thermal microscopy to a new level," *Compound semiconductor*, vol. 17, pp. 33–36, Feb. 2011.

[2] J. Glover, "The design and thermal measurement of III-V integrated micro-coolers for thermal management of microwave devices," Ph.D., De Montfort University, 2016.

[3] P. Pandey, "IR Thermal measurement on semiconductor devices.," De-Montfort University, UK, 2014.

[4] R. Hopper, "Accurate temperature measurements on semiconductor devices," Ph.D., De Montfort University, 2010.

[5] L. Zhou, B. Bo, X. Yan, C. Wang, Y. Chi, and X. Yang, "Brief Review of Surface Passivation on III-V Semiconductor," *Crystals*, vol. 8, no. 5, p. 226, May 2018, doi: 10.3390/cryst8050226.

[6] C. H. Oxley, B. M. Coaker, and N. E. Priestley, "Measured thermal images of a gallium arsenide power {MMIC} with and without {RF} applied to the input," *Solid-State Electronics*, vol. 47, no. 4, pp. 755–758, 2003, doi: http://dx.doi.org/10.1016/S0038-1101(02)00356-8.

[7] Y. Wang *et al.*, "A nanocomposite coating improving the accuracy in infrared temperature measurement for thermal micro-devices," *Sensors and Actuators A: Physical*, vol. 293, pp. 29–36, Jul. 2019, doi: 10.1016/j.sna.2019.02.019.

[8] J. Glover *et al.*, "Thermal Profiles Within the Channel of Planar Gunn Diodes Using Micro-Particle Sensors," *IEEE Electron Device Letters*, vol. 38, no. 9, pp. 1325–1327, Sep. 2017, doi: 10.1109/LED.2017.2731961.

[9] P. Pandey, C. Oxley, R. Hopper, Z. Ali, and A. Duffy, "Infra-red thermal measurement on a low-power infra-red emitter in CMOS technology," *IET Science, Measurement & Technology*, vol. 13, no. 1, pp. 25–28, Aug. 2018, doi: 10.1049/iet-smt.2018.5427.

[10] Y. Zhou and B. J. Nelson, "The effect of material properties and gripping force on micrograsping," in *Proceedings 2000 ICRA. Millennium Conference. IEEE International Conference on Robotics and Automation. Symposia Proceedings (Cat. No.00CH37065)*, 2000, vol. 2, pp. 1115–1120 vol.2, doi: 10.1109/ROBOT.2000.844748.

[11] A. I. Denisyuk, F. E. Komissarenko, and I. S. Mukhin, "Electrostatic pick-and-place micro/nanomanipulation under the electron beam," *Microelectronic Engineering*, vol. 121, pp. 15–18, Jun. 2014, doi: 10.1016/j.mee.2014.02.019.

[12] T. Echániz, R. B. Pérez-Sáez, and M. J. Tello, "IR radiometer sensitivity and accuracy improvement by eliminating spurious radiation for emissivity measurements on highly specular samples in the 2–25μm spectral range," *Measurement*, vol. 110, pp. 22–26, Nov. 2017, doi: 10.1016/j.measurement.2017.06.010.

[13] R. B. Pérez-Sáez, L. del Campo, and M. J. Tello, "Analysis of the Accuracy of Methods for the Direct Measurement of Emissivity," *Int J Thermophys*, vol. 29, no. 3, pp. 1141–1155, Jun. 2008, doi: 10.1007/s10765-008-0402-4.

[14] C. De Capua, R. Morello, and I. Jablonski, "Active and eddy current pulsed thermography to detect surface crack and defect in historical and archaeological discoveries," *Measurement*, vol. 116, pp. 676–684, Feb. 2018, doi: 10.1016/j.measurement.2017.10.035.

[15] "Use Low-Cost Materials to Increase Target Emissivity." [Online]. Available: https://www.flir.co.uk/discover/rd-science/use-low-cost-materials-to-increase-target-emissivity/. [Accessed: 24-Jun-2019].

[16] "Emissivity Coefficients Materials," *The Engineering ToolBox*. [Online]. Available: https://www.engineeringtoolbox.com/emissivity-coefficients-d_447.html. [Accessed: 06-Jul-2019].

[17] “Table of emissivity of various surfaces for infrared thermography.” MIKRON Instrument Company, Inc., Accessed: Jul. 06, 2019. [Online]. Available: http://www-eng.lbl.gov/~dw/projects/DW4229_LHC_detector_analysis/calculations/emissivity2.
[18] P. Honnerová, J. Martan, Z. Veselý, and M. Honner, “Method for emissivity measurement of semitransparent coatings at ambient temperature,” *Scientific Reports*, vol. 7, no. 1, pp. 1–14, May 2017, doi: 10.1038/s41598-017-01574-x.
[19] H. Madura, H. Polakowski, and B. Wiecek, “Spectral emissivity evaluation for material used in microelectronics,” in *Proceedings of the 1996 International Conference on Quantitative InfraRed Thermography*, 1996, doi: 10.21611/qirt.1996.009.
[20] C. H. Oxley and R. H. Hopper, “Effect of transparency within a semiconductor on emissivity mapping for thermal profile measurements of a semiconductor device,” *IET Science, Measurement Technology*, vol. 1, no. 2, pp. 79–81, Mar. 2007, doi: 10.1049/iet-smt:20060091.
[21] P. J. Timans, “The experimental determination of the temperature dependence of the total emissivity of GaAs using a new temperature measurement technique,” *Journal of Applied Physics*, vol. 72, no. 2, pp. 660–670, Jul. 1992, doi: 10.1063/1.351849.

Chapter 5

Gas sensors:

This chapter provides an overview of different gas sensors using a micro-electro-mechanical systems (MEMS) micro-heater technology including the gases which can be detected, the principle of operation and corresponding applications. Gas sensors require a micro-heater to raise the temperature of the gas sensing element and to initiate the gas chemical reactions which take place at high temperatures (typically >300 °C) [1]. There are a number of reports in the literature on the fabrication of the miniature micro-heaters using different heating materials (e.g., poly-silicon, tungsten etc.) and this will be discussed in this chapter. Most of the modern gas sensors are very important application of the MEMS micro-heater based on tungsten metallisation studied in this research work, and this will also be discussed further in this chapter.

5.1. Introduction:

Gas sensors are chemical sensors that are becoming an important part of our everyday lives. Historically, gas sensors were primarily used to detect the hazardous gases found in coal mines, which include nitrogen dioxide (NO_2), carbon monoxide (CO), hydrogen (H_2), sulphur dioxide (SO_2), methane (CH_4) and other hydrocarbons [2] as well as to detect low oxygen levels. The modern era of the gas sensor started in 1927 by Dr Oliver Johnson who developed a catalytic combustion sensor for detecting combustible gases using a platinum catalyst [3]. Modern gas sensor technologies are gaining significant interest because of the widespread applications in various fields which include; (i) indoor air quality monitoring (e.g., monitoring CO levels from boilers), (ii) industrial safety application (e.g., detection of CH_4 in mines), (iii) automobiles (e.g., detection of polluting gasses from vehicles), (iv) medical applications (for example the electronic nose (based on arrays of gas sensors), for testing the food smell and artificial fragrances [4], (v) environmental science (monitoring of greenhouse gases) and (vi) laboratory analysis (analysis of methanol and benzene) [5]. It is also very widely used in smoke detectors in private and public housing.

Over the past few decades, the demand for low cost, low power, miniaturised and reliable gas sensors are increasing [6]. This demand along with advances in micro and nanofabrication technologies has led to significant improvement in sensor design with the use of different materials (e.g., metals and their alloys, semiconductors and other compound materials like titanium nitride) [7]. MEMS technology is crucial to the modern gas-sensor and has enabled the design and fabrication of miniaturised integrated sensors with excellent performance, including low power consumption, high sensitivity, accurate selectivity and fast response/recovery time [8], [9]. Recently, gas sensors based on MEMS micro-heater technology are drawing attentions for the applications in the IoT (Internet of Things) based gas sensors [10] and expected for the potential future market [6].

Gas sensors normally consist of a chemically active layer (the detector) and a transducer, which converts a desired chemical reaction into a measurable electronic signal, such as a frequency shift, a change in resistance, a current or voltage signal, or the absorption

of light at certain frequencies [8]. Gas sensors are usually classified based on the process involved for a gas detection and the type of materials used in their fabrication.

5.2. MEMS micro-heater technology for gas sensors:

MEMS micro-heaters are becoming a crucial part for a number of micro-system applications which include wind sensors, humidity sensors and gas sensors [11]. Micro-heaters are a key element for most of the gas sensors to detect the individual gas concentrations, which are present in the mixture of gases, when it is integrated with gas sensing materials like metal oxides (e.g., ZnO, TiO_2) and polymers. The use of a micro-heater is necessary due to the gas chemical reaction which happens in the sensing layer and normally takes place at high temperatures (for example; a resistive gas sensor has an operating temperature of ~ 400 °C). In addition, MEMS micro-heaters can also be used as an IR source in a non-dispersive (NDIR) gas sensors [12], [13].

The MEMS micro-heaters consist of a substrate and a heating element, which is used to heat the sensing material for better sensitivity and short thermal response time. MEMS micro-heaters are mainly fabricated on silicon making them compatible with microelectronics integrated circuit fabrication processes including complementary-metal-oxide-semiconductor (CMOS). Micro-heaters produce heat by applying an electrical current to a thin conducting path which is made of high resistive materials (e.g., poly-silicon).

The silicon-based MEMS micro-heaters are also receiving an increasing attention in portable electronic applications because of the following potential advantages:

- Low power consumption; this allows the micro-heaters to be used in portable and wireless applications.
- Miniaturisation; small size helps in reducing the cost as small chip area enables more chips per wafer run. Additionally, small size is very important for portable devices.
- CMOS compatibility; this helps to produce low cost and reproducible sensors, and allows integration with wide range of electronic circuitry.
- Fast thermal response time; enables operation of the device in transient mode thereby reducing power consumption and temperature modulation for improved detection.
- Uniform temperature; this helps to ensure a stable performance over the device lifetime, and improves accuracy of detection.

Micro-heaters are fabricated on a membrane formed by bulk etching therefore the heater structure is thermally isolated from the rest of the circuit. In microelectronics technology, membranes are normally a very thin layer (of the order of μm) of semiconductor material (e.g., silicon, silicon dioxide, silicon nitride etc), which is formed by etching away a part of the substrate. Based on the membrane structures the micro-heaters are normally classified into two types; (i) closed membrane type and (ii) suspended membrane type (also called spider type) [7], [14]. The first type of micro-heater is formed by anisotropic etching of substrate (typically silicon) from the backside using wet etchants like potassium hydroxide

(KOH). The second type of micro-heater is usually processed by bulk or sacrificial etching from the front side [15]. The different membrane types used in micro-heaters are schematically shown in Figure 5.1.

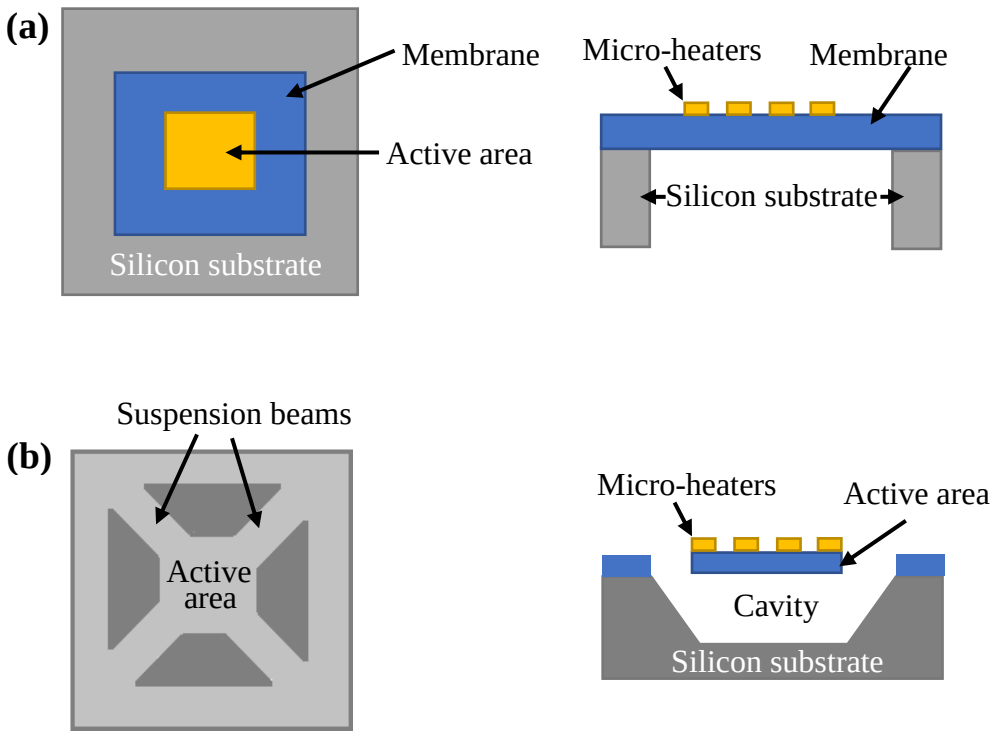

Figure 5.1: Schematic view of the micro-heaters with different membrane configuration (a) closed type (b) suspended type (left: top surface view, right: side cross-section view).

Micro-heaters based on suspended type membrane offer very low power consumption compared to the closed membrane type due to very low thermal mass of the substrate. In addition, the low thermal inertia of these type of heaters contribute to fast heat-up and cool-down times, enabling more reliable temperature modulation [8]. However, they are prone to mechanical instability, as they are supported by only 2 or 4 dielectric beams (as shown in Figure 5.1) [16].

5.2.1. The heating element materials for micro-heaters:

The selection of appropriate material for the heating element plays a very important role in the long term reliability of the micro-heater based gas sensors [15]. Chemical and mechanical stability at high temperatures are the main concerns when selecting the material for the heating element. The choice of an ideal material for the heating element depends on its properties, which include high melting point, high electrical resistivity, large Young's modulus, high thermal conductivity and also has to be compatible with standard microelectronics fabrication technologies [7].

In integrated circuit (IC) technology aluminium (Al) is well known metallisation element, and in some cases it has been used as a heating element material [15], [17]. However, the use of aluminium in these heaters limits the maximum operating temperature, due to its low melting point (660 °C) and it also suffers from surface oxide formation and electromigration at

high temperatures. In addition, aluminium also has poor contact properties to the gas sensing materials and low resistivity. Gold is a further material which has been used as a heater element but suffers from similar problems, as well as low resistivity and poor adhesion [18] to other materials. Doped poly-silicon [19] is also a widely adopted material for micro-heaters due to it being fully CMOS compatible and has good adhesion to other materials. However, poly-silicon displays poor long term stability at temperatures above 300 °C and also suffers from drift in resistivity at high temperatures (>500 °C) [8], [20].

Platinum is the most extensively used material for the heater element due to its high thermal conductivity, chemical inertness and good stability at high temperatures (~500 °C), but may suffer from drift in resistivity above (>650 °C) [7]. However, there are problems, as platinum is expensive and is not commonly used in the CMOS fabrication processes. Micro-heaters based on molybdenum metallisation [21] have been reported for operating temperature above the stability point of platinum (~500 °C) and poly-silicon (~300 °C) [20]. The main advantages of the molybdenum include; high melting point (2623 °C), ease of deposition and subsequent patterning and chemical inertness towards silicon etchant potassium hydroxide (KOH) but it is not CMOS compatible, which would lead to high manufacturing costs.

Recently, tungsten has served as an alternative heater element material for high temperature operating micro-heaters due to its very high melting point (3422 °C) and being resistant to electromigration induced failure, when compared with aluminium or poly-silicon [22], [23]. Furthermore, tungsten is CMOS compatible and enables the fabrication of micro-heaters with long term stability, thereby having all the advantages of CMOS technology.

Ali *et al.* [22] have fabricated a novel high-temperature tungsten micro-heater for use in gas sensors. The group have also been working to design and develop novel IR emitters in CMOS technology using micro-heaters based on tungsten metallisation, to enable high temperature operation [20], [24]. These emitters typically consist of a tungsten micro-heater embedded within a dielectric (SiO_2) membrane to provide thermal isolation from the silicon substrate. The devices normally operate at temperatures around 500 °C therefore emitting thermal radiation in the mid-IR range (2.5µm – l5µm) for NDIR gas sensing and spectroscopy applications. A future requirement is to operate the IR emitters at elevated temperatures (>800 °C) for spectral sensing applications in the short-wave region of the IR spectrum (1.4µm – 2.5µm) [25]. Knowledge about the thermal uniformity and maximum operating temperature of the micro-heater is key to understanding the performance and reliability of these IR emitters. The thermal characterisation of the tungsten based micro-heater, is a part of this research and the work was published [24].

The high melting point and high resistivity of titanium nitride (TiN) has led to reports on micro-heaters based on CMOS compatible titanium nitride (TiN) [26] with operating temperature up to 700 °C. Presently the fabrication process leads to high stress in the TiN films, which may cause yield problems. Low cost materials, such as nickel (Ni) have been reported as a promising alternatives for heater elements for operating temperatures below 300 °C [27] but the material may suffer from long term durability problems. Compound semiconductors like SiC [28] and doped tin dioxide [29] based micro-heaters have also been reported to be

effective heater materials for operating temperatures range of 650 °C – 1000 °C due to their robust performance at high temperatures.

The Table 5.1 provides a summary of the properties of the most common materials used in the fabrication of MEMS micro-heaters and their CMOS compatibility

Table 5.1: Comparison of material properties of different materials used in fabrication of micro-heaters [7].

Materials	Electrical resistivity in Ω-m ($\times 10^{-10}$) at 300 K	Thermal conductivity ($W.m^{-1}K^{-1}$) at 300 K	Melting point (°C)	Young's modulus (GPa)	CMOS compatibility
Al	282	237	660.3	70	Yes
Au	221.4	318	1064	79	No
Poly-silicon	322	16-34	1412	169	Yes
Pt	1050	71.6	1768	168	No
Mo	534	138	2623	329	No
W	528	173	3422	411	Yes
Ni	693	90.9	1455	200	No
TiN	2000	19.2	2930	79-250	Yes

5.3. Types of gas sensor technologies:

A review of the different types of gas sensors including their principle of operations, applications in various disciplines and their respective advantages and weakness will be discussed in the following sections.

5.3.1. Catalytic gas sensors:

Over the past several decades the catalytic gas sensors, also known as catalytic Pellistor sensors are well known for detecting combustible gases and vapours present in the air [30] These type of sensors are very sensitive to most of the available combustible gases (e.g., methane) and used for the measurement of lower explosive limit percentage (LEL) of the gas mixtures. LEL of a particular combustible gas and/or vapour is defined as; a minimum concentration of the particular gas required for combustion in normal atmospheric air. Combustible gas mixtures will burn when they reach a particular ignition temperature, but with some specific chemical processes, the gas mixtures will begin to ignite or burn even at lower temperatures. This process is commonly referred as a catalytic combustion and the catalytic gas sensors are based on this principle [31].

A conventional catalytic gas sensor is comprised of two important operational elements; (i) a detector (sensitive to combustible gases) and (ii) a compensator which has to be inert. The detector element composed of a catalytic surface which is constructed around a heater (usually platinum coil) that heats the catalyst, usually palladium, to a sufficiently high temperature to ensure any flammable gas molecules present can burn and release heat. The heater also acts as a thermal sensor and is used to determine the gas concentration by monitoring its temperature by an induced resistance change when combustion reaction takes place in the catalyst. Figure 5.2 shows a schematic of measuring circuit operation of the conventional catalyst gas sensor.

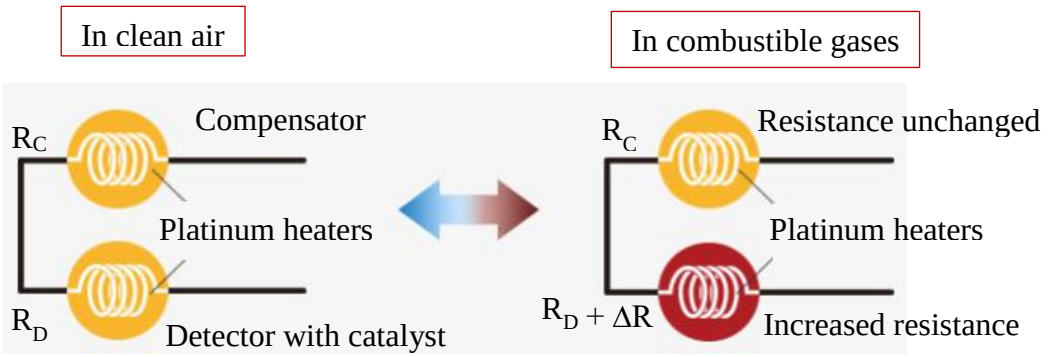

Figure 5.2: Schematic diagram of catalytic gas sensor.

Catalytic gas sensors are simple to operate, relatively less sensitive to temperature and humidity effects, fairly stable and offers long life span. However, the susceptibility to a variety of contaminating compounds such as silicones, compounds containing lead and sulphur may deteriorate the long-term stability of these sensors. Initially, these sensors were used to detect methane in coal mines, but nowadays they have been widely adopted in other industrial applications, for example, monitoring kerosene spillages in petrochemical industry. However, they require the presence of oxygen in the atmosphere to function correctly and the catalytic nature of the reaction restrict the applications to flammable gases such as hydrogen, methane, propane and butane [8].

There is a commercial drive for the low power gas sensors with the development of wireless sensor networks. Nowadays, micro-heaters have been widely used in catalytic gas sensors in preference to using a conventional platinum coil which typically has a high power consumption. There are many reports in a literature where micro-heater based catalytic gas sensors have been fabricated using MEMS technology [28], [30], [32].

5.3.2. Electrochemical gas sensors:

Electrochemical gas sensors are based on the change in electrical properties when a target gas diffuses and reacts with the sensing material. A conventional electrochemical gas sensor comprise of three important elements; a reference electrode, a sensing electrode, and a counter electrode deployed in electrolyte. These type of gas sensors allow the target gases to diffuse through a porous membrane (as shown in Figure 5.3) to a sensing electrode where they are either chemically oxidized or reduced. The oxidation or reducing reaction between the sensing material and the gas molecules gives rise to an electrical signal (current, voltage) that

is proportional to the gas concentration. It is possible to improve the sensor's selectivity to a specific gas by varying the electrode material and the electrolyte [33]. Electrochemical sensors have been widely used in a variety of environments such as, refineries, gas turbines and chemical plants for the detection of the level of oxygen and toxic gases (e.g., ammonia, carbon monoxide etc.). They are attractive because of low cost, low power, high sensitivity and high selectivity [33]. However, they suffer from limited life-time due to evaporation of the supporting liquid electrolytes. In recent years, room temperature ionic liquids (RTILs) have been utilised as electrolytes to overcome this limitation [34].

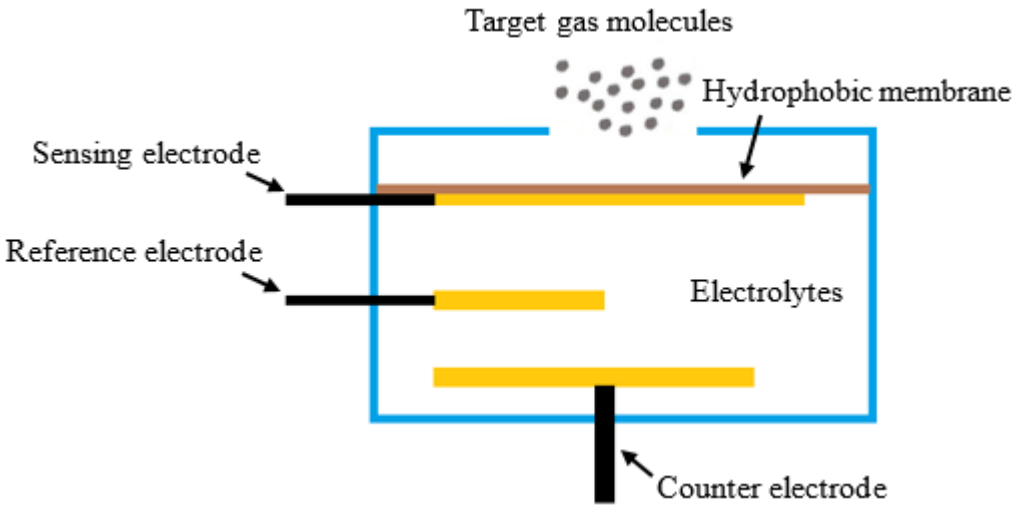

Figure 5.3: A schematic design of a basic electrochemical gas sensor.

The miniaturisation of these electrochemical gas sensors are comparatively easy (compared to optical gas sensors which will be introduced in section **5.3.3**) and can be manufactured using microfabrication (MEMS) technologies. Examples of the successful miniaturisations include metal-oxide-semiconductor (MOS) and chemical field effect transistor (chemFET) based gas sensors.

5.3.2.1. Metal oxide semiconductor gas sensors:

In the past decade, MOS based gas sensors have received significant academic and commercial attention due to their compatibility with CMOS fabrication processes and increased demand in applications including environmental, automotive emission and food safety monitoring [35]. The MOS gas sensor was first introduced by *Seiyama et. al.* as a result of studies on gas sensing properties of semiconducting metal oxide (ZnO) thin films in 1962 [36], which led to the first commercialised SnO_2 based sensor (also known as Taguchi gas sensors) for the detection of inflammable gases by *N. Taguchi* in 1968.

A typical MOS gas sensor uses a specific sensing element normally consisting of a semiconducting material deposited on an insulating substrate between a set of metallic electrodes. A heater element is also required and is electrically isolated from the sensing element. The heater element is essential to initiate the chemical reactions in the sensing layer, which take place at high temperatures. MOS gas sensors fabricated using advanced MEMS micro-heater technology play a dominant role in consumer markets due to their advantages of

short response time, high thermal efficiency, long lifetime and low fabrication cost [8]. Figure 5.4 illustrates the schematic of a MEMS micro-heater based MOS gas senor.

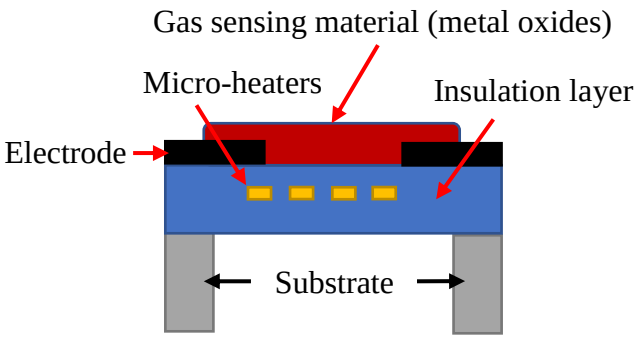

Figure 5.4: Cross sectional view of a MOS gas sensor fabricated using MEMS micro-heater technology.

A MOS gas sensor is based on change in the electrical conductivity of the sensing material (metal oxides) within the device in the presence of reducing or oxidizing gases. The sensing material is directly exposed to the target gas. Therefore, a chemical reaction is expected to take place when the sensing material is in contact with the target gas resulting in changes to the chemical and physical properties of the heated sensing material [9], leading to a change in the electrical conductivity. The change in electrical conductance of the metal oxide sensing layer is proportional to the concentration of the target gas. In general, MOS based sensors are classified into two main types; (i) n-type MOS [e.g., Tin dioxide (SnO_2), Titanium dioxide (TiO_2), Zinc oxide (ZnO), and tungsten oxide (WO_3)] based sensors and, (ii) p-type MOS [e.g, Nickel oxide (NiO), Manganese oxide (Mn_3O_4) and Chromium oxide (Cr_2O_3)] based sensors [37]. When n-type MOS sensors are exposed to reducing gases (e.g., carbon monoxide (CO), ammonia (NH_3) or other hydrocarbons etc.), there will be an increase in electrical conductivity and if it is exposed to an oxidizing gas (e.g., NO_2) then depletion of charge carriers occur, leading to a decrease in electrical conductivity. Conversely, when the p-type MOS sensor interact with reducing or oxidizing gases, then it shows a vice versa behaviour.

MOS gas sensors are commonly used in applications requiring to detect low concentration of volatile organic compounds (VOCs) such as benzene and formaldehyde. The advantages of these sensors include user simplicity, durability, high sensitivity, high stability, detection of a wide variety of gases and resistant to many common sensor contaminations such as silicones and compounds containing lead [38]. However, they suffer from poor gas selectivity. It has been reported that the better selectivity can be achieved by adding small amount of a noble metal like palladium. For example; tin oxide can be made more selective to carbon monoxide gas with a doping of 0.5% of palladium [16] [37].

5.3.2.2. Chem FET gas sensors:

These are field effect transistors (FET) with the gate fabricated with a conducting gas sensing material, typically a catalytic metal, such as platinum. The selectivity for the target gas is highly dependent on the electrical characteristics of the catalytic metal [33]. FET sensors use the shift in the transistor threshold voltage to determine the gas concentration, when the gas

molecules interact with the gate material. The technology is fully compatible with CMOS processes and can operate at room temperatures, and thus has a very low level of power consumption. However, their performance is strongly influenced by change in temperature, and FET gas sensors with platinum or palladium gates are only sensitive to hydrogen. Recently, nanomaterials such as graphene, nanowires (NWs) and carbon nanotubes (CNTs) have been used as the gas sensing element to improve selectivity and performance of FET gas sensors [39], [40]. These improved FET sensors have been used to detect volatile organic compounds (VOCs) including NO_2, CO_2, CO, NH_3 and toxic gases. These sensors show great potential in various fields including of fire detection, food storage, environmental monitoring, medical applications and smart health care industries [41]. A schematic diagram of the FET gas sensor is shown in Figure 5.5.

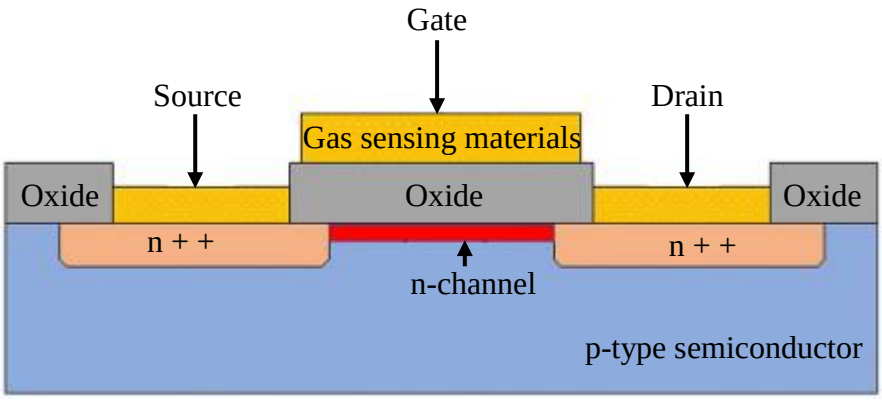

Figure 5.5: Schematic of a typical FET gas sensor.

5.3.3. Optical gas sensors

Optical emission/absorption or scattering of gas molecules at defined optical wavelengths is monitored by the optical gas sensors to detect and measure the gas concentration. The key parts are; a light source (light-emitting diode (LED), quantum cascade lasers, MEMS thermal emitters etc.) with optical emission in the range of interest, a photo-detector, a filter and a gas sensing element responding to the optical emission [12]. The advantages of this type of gas sensor include; high sensitivity, long term stability, high selectivity and the performance is invariant to a changing environment. In addition, they offer real-time and *in situ* detection. Optical gas sensors have been used in indoor air quality management, medical applications (e.g., breath analysis) [42], food quality control and in atmospheric science where they are used to detect the greenhouse gases [12], [43]. Their cost is high and difficult to miniaturise for system integration which will restrict their use in portable equipment.

One of the most common optical gas sensors is the non-dispersive infra-red (NDIR) gas sensor, which will be discussed in the following section.

5.3.3.1. Non-dispersive infra-red gas sensors:

Many chemicals exhibit strong absorption lines caused by molecular vibrations in the UV/visible, near-IR or mid-IR regions of the electromagnetic spectrum. NDIR gas sensing

relies on the specific radiation bandwidth (typically in wavelengths between 2µm to 14µm spectral region) and the absorption properties of target gas molecules [12]. The mid-IR spectral region is of particular interest because it supports stronger molecular absorption compared with the near IR region, and also the spectra lines are less congested, allowing greater selectivity [12]. The characteristic absorption lines of some important gas molecules with their relative intensities in the mid-IR spectral region is shown in Figure 5.6 [12], [44]. NDIR spectroscopy provides excellent stability, high sensitivity and selectivity. Therefore, it is one of the highly preferred technique for chemical analysis in industrial process control, environmental monitoring, and medical diagnosis (e.g., asthma monitoring device) [45].

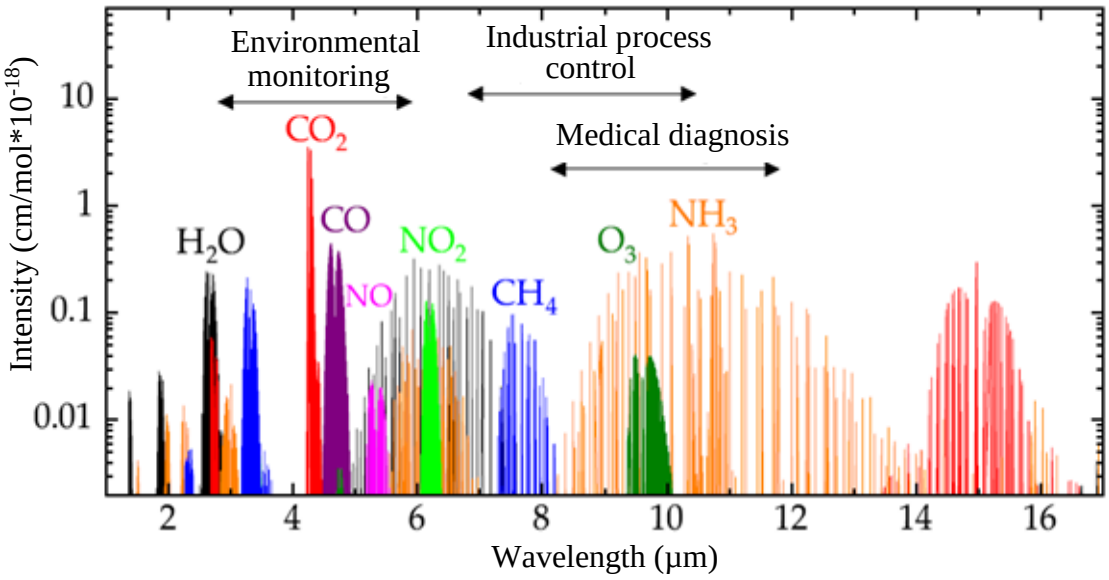

Figure 5.6: Absorption spectra of selected gas molecules in the mid-IR region of the electromagnetic spectrum [12].

The working principle of the NDIR gas sensors is based on the Beer-Lambert's law [46], where a gas is detected according to equation **(5.1)** [12].

$$I(\lambda) = [I_0(\lambda) \times e^{-\alpha(\lambda)c.l}] \qquad \textbf{(5.1)}$$

Where, $I(\lambda)$ and $I_0(\lambda)$ (typically with units of [W/m^2]) are the respective detected and emitted optical intensities at the spectral wavelength λ. Similarly, l is the optical path-length, which governs the sensor sensitivity, c is the gas concentration, and $\alpha(\lambda)$ is the gas absorption coefficient.

A typical NDIR gas sensor will consist of an IR source, a gas chamber which enables the light to interact with the gas, an optical filter to select the range of wavelengths characteristic to the target gas and a detector. Figure 5.7 shows a schematic diagram of a typical NDIR gas sensor.

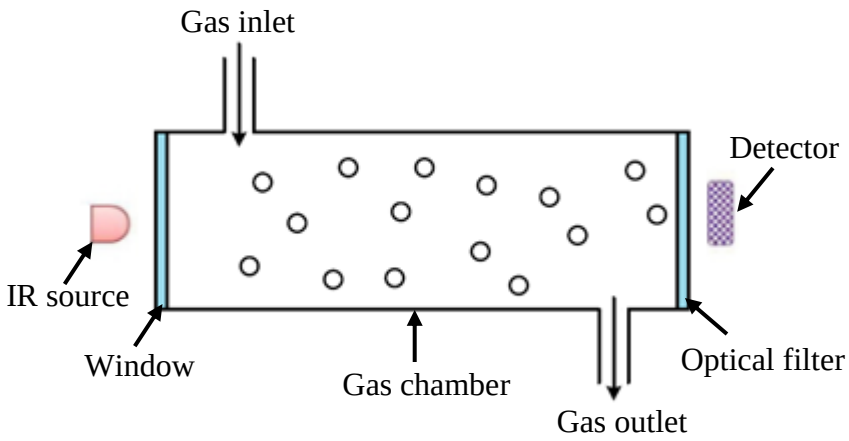

Figure 5.7: A schematic diagram of a typical NDIR gas sensing system.

One of the main components of NDIR spectroscopy is the IR source. NDIR gas sensors traditionally use a glass micro-bulb as the IR source. Although, these bulbs can be manufactured at low cost, they suffer from high power consumption, they are large in comparison with silicon based IR sources, have slow transient response time, the output is limited to a wavelength of around 5µm and poor life-time. In recent years, CMOS compatible miniature IR sources based on MEMS processing technology have become available [13], [24], [47], [48]. The development of these low power, low cost miniaturised IR sources with fast thermal transient times, have increased the popularity of NDIR gas sensors particularly for detecting gases with absorbance peak in the longer wavelength part of the mid-IR spectrum (>5µm). The technology is also compatible with wireless gas sensor networks such as indoor air quality monitoring system (heating, ventilation and air conditioning), toxic gas sensing in military battlefield operations [49], [50] and capnography applications [43]. With the emerging trend in miniaturisation, the potential applications of NDIR gas sensors such as integration with medical devices to identify the impurities or counterfeits in medicines [51] and also integration with consumer electronics (e.g., smartphones, tablets and other wearable digital devices) are expected.

NDIR gas sensors have been mainly used to detect CO_2, as this gas has a pronounced absorption peak around 4.26µm wavelength and is difficult to be detected by electrochemical or other inexpensive gas sensors. However, the technology has been successfully implemented to detect other gases including carbon monoxide, ammonia, methane, ethanol, and other volatile organic compounds (VOCs) [13], [52]. The major advantages of NDIR gas sensor include the ability to detect target gases in inert atmospheres, immunity to contamination and poisoning, and stable long-term operation. The main disadvantage of the NDIR gas sensor is, they require the target gas to be IR active. Additionally, they are susceptible to high humidity and dust environments which may increase maintenance costs, to increase sensitivity long optical interaction path-length are required, interference may also occur from highly absorbing compounds like water vapour and not suitable for multiple gas detection.

A major part of my research work has been to look at the temperature uniformity and maximum operating temperature of the MEMS micro-heater which can be used as the mid and

near field IR sources. It is important to assess the thermal uniformity and accurate maximum operating temperature of these IR sources to ensure consistent IR emission for better gas selectivity detection as well as optimum performance and reliability. The MEMS micro-heater is also used in other types of gas sensor including MOS gas sensor [53], [54] and catalytic gas sensor [55].

5.3.3.2. Other optical gas sensing technology:

Photoionization gas sensors are a commonly used optical technique for the detection of VOCs such as vinyl chloride, benzene, toluene and other hydrocarbons [56]. These sensors use high energy ultraviolet (UV) photons to excite and ionize the gas molecules. The generated charged ions produce an electrical current which is proportional to the concentration of the target gas. The main advantages of these sensors include, low cost and simplicity of use, portability, non-destructive, high sensitivity and fast response time. The limitations include humidity effects, non-specific response to gas type and not suitable to detect chemicals with high ionization potentials such as methane.

The photonic crystal gas sensor is another example of an optical gas sensing technology. These sensors are refractive index based that commonly employ highly periodic micro or nano structural arrangements of dielectric materials with different refractive index for gas detection [9], [57]. The advantages of these gas sensors include, high sensitivity, high detection accuracy and fast response time. The operating principle is based on refractive index changes, and therefore, detecting different gases with same refractive index is very challenging. This technique has been used for the detection of VOCs including ethanol and carbon disulphide [9], [58].

5.3.4. Acoustic wave gas sensors:

The idea of the acoustic gas sensor began with quartz crystal microbalance (QCM) and was first implemented to sense organic vapour by King in 1964 [59]. Acoustic gas sensors measure the frequency shift of the acoustic wave when the target gas molecules are absorbed on the surface of an oscillating structure (which is usually a quartz crystals transducer). The sensor device is usually coated with the sensing material which absorbs the target gas. The process of absorption adds mass to the sensing layer resulting in change in the acoustic wave oscillation frequency (Figure 5.8) [60]. Acoustic wave based sensors can offer low power consumption at a low unit cost, high sensitivity and short response time [61], [62]. However, the acoustic wave properties are highly dependent on temperature, thus, giving rise to environment issues. Gas sensors based on this method have been successfully used for the detection of VOCs such as alcohols, halocarbons, and toxic gases [9], [63].

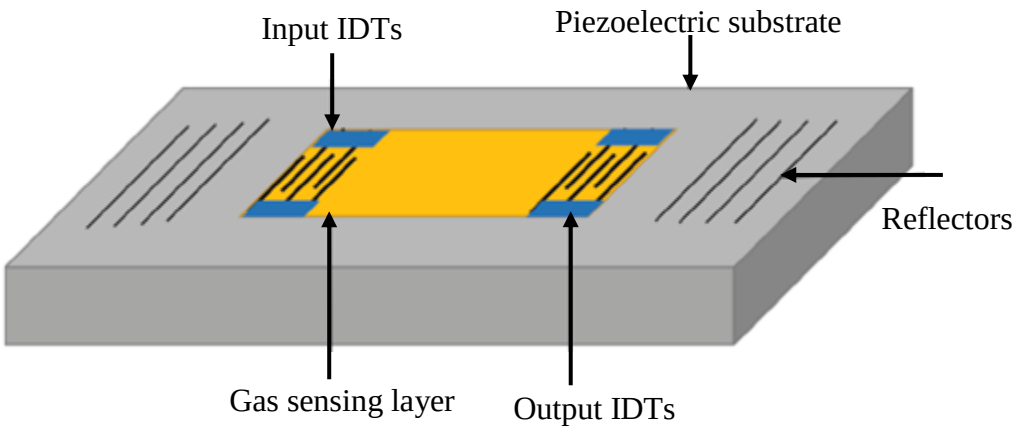

Figure 5.8: A schematic diagram of an acoustic wave gas sensing device [9].

5.4. Gas sensing materials:

Gas sensing material is the core part of most gas sensors which involve chemical reactions for gas sensing. Thus, the performance, reliability and sensitivity of these chemically active gas sensors are highly dependent on the sensing materials. In the past conducting polymers and carbon nano-tubes (CNTs) have been extensively investigated as sensor materials.

5.4.1. Polymers:

Conducting polymers, such as polyaniline (PANI), polypyrrole (PPy), polythiophene (PTs) and their derivatives have been widely used as a gas sensing materials [33]. Gas sensors fabricated using conducting polymers are of interest due to their important features, which include short response time with high sensitivity, ease in fabrication and modifications to improve the selectivity, good mechanical properties and ability to operate at lower temperatures [64] compared to metal oxide based gas sensors. In addition, sensor arrays can also be formed with MEMS fabrication techniques, which enable for miniaturisation and mass production of gas sensors at low-cost. However, the main disadvantages of polymer-based gas sensors include temperature dependence, short lifetime, the sensitivity can be influenced by humidity and prone to contamination.

5.4.2. Carbon nano-tubes (CNTs):

The electronic properties of the CNTs are highly sensitive to the absorbed molecules on their surface, which make the CNTs a popular material in gas sensing research/applications. CNTs are formed from graphene sheets rolled up into a tube shape, and are generally categorized into two types; (i) single-walled carbon nano-tube (SWCNT), and (ii) multi-walled carbon nano-tube (MWCNT). Single-walled CNT comprises of single layer of CNT while multi-walled CNT consist of a multiple layers of CNTs inside each other, sharing the same central axis as shown in Figure 5.9. In RFID tag antennas SWCNTs have been used for detecting the toxic gases and MWCNTs for remote detection of gases like CO_2 and ammonia [5].

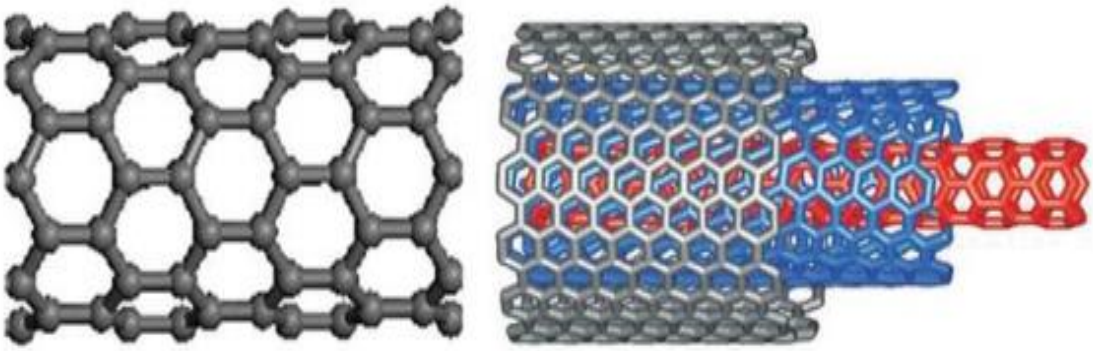

(a) **(b)**

Figure 5.9: Schematic configuration of CNTs (a) SWCNTs (b) MWCNTs [65].

The electrical properties of CNTs rely upon the twist of the nanotubes (graphene), and can either be metallic or semiconducting in nature depending upon the direction rolled to form a tubular construction. Semi-conducting CNTs are generally used in gas sensing [66]. CNTs have proved to be promising gas sensing materials particularly because of their high surface-to-volume ratio with very strong intermolecular bond capability. This means they require a relatively small area for gas detection, enabling the miniaturisation of gas sensors. In addition, CNTs based gas sensors offer fast response time, resistance to corrosion, ability to operate at room temperatures, and the ability to detect wide variety of gases including NO_2, NH_3, CH_4, H_2S, H_2O_2, CO, CO_2 and alcohol hydrocarbons [67]. However, some of the challenges related to CNTs for gas sensing applications include; CNT synthesis is expensive, precise control over the growth of CNTs on the surface of gas sensors is difficult and sensitive to high humidity effects.

5.5. Comparison of different gas sensing methods:

Table 5.2 gives an overview of advantages, disadvantages and application of different gas sensing techniques. The table also provides information regarding the MEMS micro-heater technology (discussed in section 5.2) required for different gas sensing techniques for their operation.

Table 5.2: Comparison of different gas sensing technology.

Gas sensing methods	**Advantages**	**Disadvantages**	**Requiring miniature hotplate technology**
Catalytic	• Low cost, simple to operate • Low effect by temperature and humidity • Widely used in coal mines and petrochemical industries • Suitable for detection of hydrogen and methane	• Require oxygen to operate • Risk of catalyst contamination by lead, silicones etc. • Risk of explosion	Yes
Electrochemical	• Low cost • Can detect wide range of target gases • Can measure toxic gases in low concentration • Widely used in refineries to detect oxygen levels	• Generally require high operating temperature • Difficult to identify the failure modes	Yes
Non-dispersive infra-red	• Ability to operate in inert atmospheres • Immune to contamination • Often used to detect CO_2 • Stable long term operation	• High cost and difficulty in miniaturisation • Target gas must be an IR active • Not suitable for detecting low concentration of gas	Yes

Surface acoustic wave	• Small size and can be used in wireless applications • Long lifetime • Able to operate at high resonant frequency	• Suffer from physical and/ or chemical interference	No
CNT based gas sensors	• Highly sensitive and fast response time • Large surface-to-volume ratio • High adsorption capacity • Ability to operate at room temperatures	• High cost • Difficulties in fabrication and repeatability of CNTs growth	No

5.6. Conclusion:

The chapter has reviewed the different gas-sensor technologies, which are in a continuous demand for miniaturisation and high-performance gas sensors. Gas sensor technology based on MEMS micro-heater technology is being used in a number of sensing technologies which have been identified. The major part of this research work is to look at the temperature uniformity and maximum operating temperature of the tungsten based MEMS micro-heater which can also be used as a mid and near field IR emitter source in gas sensing technology. The thermal uniformity across the surface of the micro-heater is very important for gas sensing applications as any localised hotspots will cause thermally induced stress leading to reliability issues. Uniformity of the heater surface is also required for good gas selectivity detection.

As described, the MEMS micro-heater was designed to operate at very high operating temperatures, in excess of 800 °C. The high temperature thermal characterisation of the MEMS micro-heater will be carried out using the non-contact optical approaches based on IR and a novel thermal-incandescence microscopy technique (fully described in Chapter 7). The experimental thermal profiling results of tungsten MEMS micro-heaters will be discussed in Chapter 6 (using IR microscopy) and Chapter 7 (using thermal-incandescence microscopy).

5.7. References:

[1] Y. Xing, T. A. Vincent, M. Cole, and J. W. Gardner, “Real-Time Thermal Modulation of High Bandwidth MOX Gas Sensors for Mobile Robot Applications,” *Sensors*, vol. 19, no. 5, p. 1180, Jan. 2019, doi: 10.3390/s19051180.

[2] Sharma Swati and Madou Marc, “A new approach to gas sensing with nanotechnology,” *Philosophical Transactions of the Royal Society A: Mathematical, Physical and Engineering Sciences*, vol. 370, no. 1967, pp. 2448–2473, May 2012, doi: 10.1098/rsta.2011.0506.

[3] R. Achkar, N. Makhoul, C. A. Haidar, and H. Osseili, “Gas ascertainment via smartphone,” in *2013 7th IEEE GCC Conference and Exhibition (GCC)*, 2013, pp. 220–224, doi: 10.1109/IEEEGCC.2013.6705779.

[4] K. Arshak, E. Moore, G. M. Lyons, J. Harris, and S. Clifford, “A review of gas sensors employed in electronic nose applications,” *Sensor Review*, Jun. 2004, doi: 10.1108/02602280410525977.

[5] X. Liu *et al.*, “A Survey on Gas Sensing Technology,” *Sensors*, vol. 12, no. 7, pp. 9635–9665, Jul. 2012, doi: 10.3390/s120709635.

[6] J. B. A. Gomes, J. J. P. C. Rodrigues, R. A. L. Rabêlo, N. Kumar, and S. Kozlov, “IoT-Enabled Gas Sensors: Technologies, Applications, and Opportunities,” *Journal of Sensor and Actuator Networks*, vol. 8, no. 4, p. 57, Dec. 2019, doi: 10.3390/jsan8040057.

[7] P. Bhattacharyya, “Technological Journey Towards Reliable Microheater Development for MEMS Gas Sensors: A Review,” *IEEE Transactions on Device and Materials Reliability*, vol. 14, no. 2, pp. 589–599, Jun. 2014, doi: 10.1109/TDMR.2014.2311801.

[8] H. Liu, L. Zhang, K. H. H. Li, and O. K. Tan, “Microhotplates for Metal Oxide Semiconductor Gas Sensor Applications—Towards the CMOS-MEMS Monolithic Approach,” *Micromachines*, vol. 9, no. 11, p. 557, Nov. 2018, doi: 10.3390/mi9110557.

[9] H. Nazemi, A. Joseph, J. Park, and A. Emadi, “Advanced Micro- and Nano-Gas Sensor Technology: A Review,” *Sensors*, vol. 19, no. 6, p. 1285, Jan. 2019, doi: 10.3390/s19061285.

[10] J.-H. Suh *et al.*, “Fully integrated and portable semiconductor-type multi-gas sensing module for IoT applications,” *Sensors and Actuators B: Chemical*, vol. 265, pp. 660–667, Jul. 2018, doi: 10.1016/j.snb.2018.03.099.

[11] W.-J. Hwang, K.-S. Shin, J.-H. Roh, D.-S. Lee, and S.-H. Choa, “Development of Micro-Heaters with Optimized Temperature Compensation Design for Gas Sensors,” *Sensors*, vol. 11, no. 3, pp. 2580–2591, Mar. 2011, doi: 10.3390/s110302580.

[12] D. Popa and F. Udrea, “Towards Integrated Mid-Infrared Gas Sensors,” *Sensors*, vol. 19, no. 9, p. 2076, Jan. 2019, doi: 10.3390/s19092076.

[13] A. Pusch *et al.*, “A highly efficient CMOS nanoplasmonic crystal enhanced slow-wave thermal emitter improves infrared gas-sensing devices,” *Scientific Reports*, vol. 5, p. 17451, Dec. 2015, doi: 10.1038/srep17451.

[14] T. Li, L. Xu, and Y. Wang, “Micro-Heater-Based Gas Sensors,” in *Micro Electro Mechanical Systems*, Q.-A. Huang, Ed. Singapore: Springer Singapore, 2018, pp. 717–752.

[15] I. Simon, N. Bârsan, M. Bauer, and U. Weimar, “Micromachined metal oxide gas sensors: opportunities to improve sensor performance,” *Sensors and Actuators B: Chemical*, vol. 73, no. 1, pp. 1–26, Feb. 2001, doi: 10.1016/S0925-4005(00)00639-0.

[16] S. Z. Ali, “Electro-thermo-mechanical study of membrane devices for smart IC technologies,” Ph.D., University of Cambridge, 2008.

[17] R. Phatthanakun, P. Deekla, W. Pummara, C. Sriphung, C. Pantong, and N. Chomnawang, “Design and fabrication of thin-film aluminum microheater and nickel temperature sensor,” in *2012 7th IEEE International Conference on Nano/Micro*

Engineered and Molecular Systems (NEMS), 2012, pp. 112–115, doi: 10.1109/NEMS.2012.6196735.
[18] K. L. Zhang, S. K. Chou, and S. S. Ang, "Fabrication, modeling and testing of a thin film Au/Ti microheater," *International Journal of Thermal Sciences*, vol. 46, no. 6, pp. 580–588, Jun. 2007, doi: 10.1016/j.ijthermalsci.2006.08.002.
[19] H. San, X. Chen, M. Cheng, and F. Li, "A silicon micromachined infrared emitter based on SOI wafer," in *MEMS/MOEMS Technologies and Applications III*, 2008, vol. 6836, p. 68360N, doi: 10.1117/12.755923.
[20] S. Z. Ali, A. D. Luca, R. Hopper, S. Boual, J. Gardner, and F. Udrea, "A Low-Power, Low-Cost Infra-Red Emitter in CMOS Technology," *IEEE Sensors Journal*, vol. 15, no. 12, pp. 6775–6782, Dec. 2015, doi: 10.1109/JSEN.2015.2464693.
[21] L. L. R. Rao, M. K. Singha, K. M. Subramaniam, N. Jampana, and S. Asokan, "Molybdenum Microheaters for MEMS-Based Gas Sensor Applications: Fabrication, Electro-Thermo-Mechanical and Response Characterization," *IEEE Sensors Journal*, vol. 17, no. 1, pp. 22–29, Jan. 2017, doi: 10.1109/JSEN.2016.2621179.
[22] S. Z. Ali, F. Udrea, W. I. Milne, and J. W. Gardner, "Tungsten-Based SOI Microhotplates for Smart Gas Sensors," *Journal of Microelectromechanical Systems*, vol. 17, no. 6, pp. 1408–1417, Dec. 2008, doi: 10.1109/JMEMS.2008.2007228.
[23] F. Shao *et al.*, "NH3 sensing with self-assembled ZnO-nanowire μHP sensors in isothermal and temperature-pulsed mode," *Sensors and Actuators B: Chemical*, vol. 226, pp. 110–117, Apr. 2016, doi: 10.1016/j.snb.2015.11.109.
[24] P. Pandey, C. Oxley, R. Hopper, Z. Ali, and A. Duffy, "Infra-red thermal measurement on a low-power infra-red emitter in CMOS technology," *IET Science, Measurement & Technology*, vol. 13, no. 1, pp. 25–28, Aug. 2018, doi: 10.1049/iet-smt.2018.5427.
[25] M. Yu, Y. Okawachi, A. G. Griffith, N. Picqué, M. Lipson, and A. L. Gaeta, "Silicon-chip-based mid-infrared dual-comb spectroscopy," *Nature Communications*, vol. 9, no. 1, p. 1869, May 2018, doi: 10.1038/s41467-018-04350-1.
[26] J. F. Creemer *et al.*, "Microhotplates with TiN heaters," *Sensors and Actuators A: Physical*, vol. 148, no. 2, pp. 416–421, Dec. 2008, doi: 10.1016/j.sna.2008.08.016.
[27] P. Bhattacharyya, P. K. Basu, B. Mondal, and H. Saha, "A low power MEMS gas sensor based on nanocrystalline ZnO thin films for sensing methane," *Microelectronics Reliability*, vol. 48, no. 11, pp. 1772–1779, Nov. 2008, doi: 10.1016/j.microrel.2008.07.063.
[28] A. Harley-Trochimczyk, A. Rao, H. Long, A. Zettl, C. Carraro, and R. Maboudian, "Low-power catalytic gas sensing using highly stable silicon carbide microheaters," *Journal of Micromechanics and Microengineering*, vol. 27, no. 4, p. 045003, 2017, doi:10.1088/1361-6439/aa5d70.
[29] J. Spannhake, O. Schulz, A. Helwig, A. Krenkow, G. Müller, and T. Doll, "High-temperature MEMS Heater Platforms: Long-term Performance of Metal and Semiconductor Heater Materials," *Sensors*, vol. 6, no. 4, pp. 405–419, Apr. 2006, doi: 10.3390/s6040405.
[30] E.-B. Lee *et al.*, "Micromachined catalytic combustible hydrogen gas sensor," *Sensors and Actuators B: Chemical*, vol. 153, no. 2, pp. 392–397, Apr. 2011, doi: 10.1016/j.snb.2010.11.004.
[31] Z. Yunusa, M. N. Hamidon, A. Kaiser, and Z. Awang, "Gas sensors: A review," *Sensors & Transducers*, vol. 168, no. 4, pp. 61–75, Apr. 2014.
[32] L. Xu, Y. Wang, H. Zhou, Y. Liu, T. Li, and Y. Wang, "Design, Fabrication, and Characterization of a High-Heating-Efficiency 3-D Microheater for Catalytic Gas Sensors," *Journal of Microelectromechanical Systems*, vol. 21, no. 6, pp. 1402–1409, Dec. 2012, doi: 10.1109/JMEMS.2012.2208219.

[33] D. Kwak, Y. Lei, and R. Maric, “Ammonia gas sensors: A comprehensive review,” *Talanta*, vol. 204, pp. 713–730, 2019, doi: 10.1016/j.talanta.2019.06.034.
[34] J. Lee, G. D. Plessis, D. W. M. Arrigan, and D. S. Silvester, “Towards improving the robustness of electrochemical gas sensors: impact of PMMA addition on the sensing of oxygen in an ionic liquid,” *Analytical Methods*, vol. 7, no. 17, pp. 7327–7335, 2015, doi: 10.1039/C5AY00497G.
[35] F. Morisot *et al.*, “ZnO based nanowire network for gas sensing applications,” *Mater. Res. Express*, vol. 6, no. 8, p. 084004, May 2019, doi: 10.1088/2053-1591/ab1f60.
[36] T. Seiyama, A. Kato, K. Fujiishi, and M. Nagatani, “A New Detector for Gaseous Components Using Semiconductive Thin Films.,” *Anal. Chem.*, vol. 34, no. 11, pp. 1502–1503, Oct. 1962, doi: 10.1021/ac60191a001.
[37] A. Dey, “Semiconductor metal oxide gas sensors: A review,” *Materials Science and Engineering: B*, vol. 229, pp. 206–217, Mar. 2018, doi: 10.1016/j.mseb.2017.12.036.
[38] J. Zhang, Z. Qin, D. Zeng, and C. Xie, “Metal-oxide-semiconductor based gas sensors: screening, preparation, and integration,” *Physical Chemistry Chemical Physics*, vol. 19, no. 9, pp. 6313–6329, 2017, doi: 10.1039/c6cp07799d.
[39] A. I. Chernov *et al.*, “Field Effect Transistor Based on Solely Semiconducting Single-Walled Carbon Nanotubes for the Detection of 2-Chlorophenol,” *physica status solidi (b)*, vol. 255, no. 1, p. 1700139, 2018, doi: 10.1002/pssb.201700139.
[40] H. Fan, S. Han, Z. Song, J. Yu, and H. E. Katz, “Organic field-effect transistor gas sensor based on GO/PMMA hybrid dielectric for the enhancement of sensitivity and selectivity to ammonia,” *Organic Electronics*, vol. 67, pp. 247–252, Apr. 2019, doi: 10.1016/j.orgel.2019.01.038.
[41] S. Zhang, Y. Zhao, X. Du, Y. Chu, S. Zhang, and J. Huang, “Gas Sensors Based on Nano/Microstructured Organic Field-Effect Transistors,” *Small*, vol. 15, no. 12, p. 1805196, Mar. 2019, doi: 10.1002/smll.201805196.
[42] M. Metsälä, “Optical techniques for breath analysis: from single to multi-species detection,” *J. Breath Res.*, vol. 12, no. 2, p. 027104, Jan. 2018, doi: 10.1088/1752-7163/aa8a31.
[43] J. Hodgkinson and R. P. Tatam, “Optical gas sensing: a review,” *Meas. Sci. Technol.*, vol. 24, no. 1, p. 012004, Nov. 2012, doi: 10.1088/0957-0233/24/1/012004.
[44] I. E. Gordon *et al.*, “The HITRAN2016 molecular spectroscopic database,” *Journal of Quantitative Spectroscopy and Radiative Transfer*, vol. 203, pp. 3–69, Dec. 2017, doi: 10.1016/j.jqsrt.2017.06.038.
[45] O. P. Singh and M. Malarvili, “Review of Infrared Carbon-Dioxide Sensors and Capnogram Features for Developing Asthma-Monitoring Device,” *JOURNAL OF CLINICAL AND DIAGNOSTIC RESEARCH*, vol. 12, no. 10, 2018, doi: 10.7860/JCDR/2018/35870.12099.
[46] P. F. Bernath, *Spectra of Atoms and Molecules*, 3rd ed. Oxford, UK; New York, NY, USA: Oxford University Press, 2016.
[47] T. A. Vincent and J. W. Gardner, “A low cost MEMS based NDIR system for the monitoring of carbon dioxide in breath analysis at ppm levels,” *Sensors and Actuators B: Chemical*, vol. 236, pp. 954–964, Nov. 2016, doi: 10.1016/j.snb.2016.04.016.
[48] N. Li *et al.*, “A Monolithically Integrated CMOS-MEMS Infrared Emitter with Graphene Oxide for Emission Enhancement,” in *Conference on Lasers and Electro-Optics (2019), paper JTh2A.34*, 2019, p. JTh2A.34, doi: 10.1364/CLEO_AT.2019.JTh2A.34.
[49] P. Bansal and R. Thareja, “Recent Advances and Techniques in the Hazardous Gases Detection,” *Handbook of Ecomaterials*, pp. 1–19, 2018.
[50] C. Corsi, “Infrared: a key technology for security systems,” *Advances in Optical technologies*, vol. 2012, 2012.

[51] G. Lawson, J. Ogwu, and S. Tanna, “Quantitative screening of the pharmaceutical ingredient for the rapid identification of substandard and falsified medicines using reflectance infrared spectroscopy,” *PLOS ONE*, vol. 13, no. 8, p. e0202059, Aug. 2018, doi: 10.1371/journal.pone.0202059.
[52] R. Bogue, “Detecting gases with light: a review of optical gas sensor technologies,” *Sensor Review*, vol. 35, no. 2, pp. 133–140, 2015, doi: 10.1108/SR-09-2014-696.
[53] B. C. Serban *et al.*, “Nanostructured metal oxides semiconductors for oxygen chemiresistive sensing,” *Romanian Journal of Information Science and Technology*, vol. 20, no. 2, pp. 86–100, 2019, doi: 10.17863/CAM.44743.
[54] J. W. Gardner, T. Ahmed, P. T. Moseley, S. Z. Ali, M. F. Chowdhury, and F. Udrea, “High temperature robust SOI ethanol sensor,” *Procedia Engineering*, vol. 25, pp. 1317–1320, 2011, doi: 10.1016/j.proeng.2011.12.325.
[55] C. Zuliani, R. Hopper, M. Musto, A. De Luca, C. Falco, and F. Udrea, “A CMOS-Based Thermo-Electrocatalytic Gas Sensor for Selective and Low-Level Detection of Carbon Monoxide and Hydrogen,” in *2019 20th International Conference on Solid-State Sensors, Actuators and Microsystems Eurosensors XXXIII (TRANSDUCERS EUROSENSORS XXXIII)*, 2019, pp. 322–325, doi: 10.1109/TRANSDUCERS.2019.8808602.
[56] X. Pang, H. Nan, J. Zhong, D. Ye, M. D. Shaw, and A. C. Lewis, “Low-cost photoionization sensors as detectors in GC × GC systems designed for ambient VOC measurements,” *Science of The Total Environment*, vol. 664, pp. 771–779, May 2019, doi: 10.1016/j.scitotenv.2019.01.348.
[57] H. Xu, P. Wu, C. Zhu, A. Elbaz, and Z. Z. Gu, “Photonic crystal for gas sensing,” *J. Mater. Chem. C*, vol. 1, no. 38, pp. 6087–6098, Sep. 2013, doi: 10.1039/C3TC30722K.
[58] T. Hemati and B. Weng, “The Mid-Infrared Photonic Crystals for Gas Sensing Applications,” *Photonic Crystals - A Glimpse of the Current Research Trends*, Nov. 2018, doi: 10.5772/intechopen.80042.
[59] W. H. King, “Piezoelectric sorption detector.,” *Analytical Chemistry*, vol. 36, no. 9, pp. 1735–1739, 1964, doi: 10.1021/ac60215a012.
[60] A. Mujahid and F. L. Dickert, “Surface Acoustic Wave (SAW) for Chemical Sensing Applications of Recognition Layers,” *Sensors*, vol. 17, no. 12, p. 2716, Dec. 2017, doi: 10.3390/s17122716.
[61] J. D. N. Cheeke and Z. Wang, “Acoustic wave gas sensors,” *Sensors and Actuators B: Chemical*, vol. 59, no. 2, pp. 146–153, Oct. 1999, doi: 10.1016/S0925-4005(99)00212-9.
[62] L. Rana, R. Gupta, R. Kshetrimayum, M. Tomar, and V. Gupta, “Fabrication of surface acoustic wave based wireless NO2 gas sensor,” *Surface and Coatings Technology*, vol. 343, pp. 89–92, Jun. 2018, doi: 10.1016/j.surfcoat.2017.10.077.
[63] S. Öztürk, A. Kösemen, Z. A. Kösemen, N. Kılınç, Z. Z. Öztürk, and M. Penza, “Electrochemically growth of Pd doped ZnO nanorods on QCM for room temperature VOC sensors,” *Sensors and Actuators B: Chemical*, vol. 222, pp. 280–289, Jan. 2016, doi: 10.1016/j.snb.2015.08.083.
[64] J. Sołoducho and J. Cabaj, “Conducting Polymers in Sensor Design,” *Conducting Polymers*, Oct. 2016, doi: 10.5772/63227.
[65] J. Tang, X. Zhang, S. Xiao, and Y. Gui, “Experimental Analysis of Modified CNTs-Based Gas Sensor,” *Electrochemical Sensors Technology*, May 2017, doi: 10.5772/intechopen.68590.
[66] Y. Wang and J. T. W. Yeow, “A Review of Carbon Nanotubes-Based Gas Sensors,” *Journal of Sensors*, vol. 2009, p. 493904, 2009, doi: 10.1155/2009/493904.
[67] T. Han, A. Nag, S. Chandra Mukhopadhyay, and Y. Xu, “Carbon nanotubes and its gas-sensing applications: A review,” *Sensors and Actuators A: Physical*, vol. 291, pp. 107–143, Jun. 2019, doi: 10.1016/j.sna.2019.03.053.

Chapter 6

IR thermal measurements on MEMS micro-heaters

6.1. Introduction:

This chapter describes the thermal characterisation of novel tungsten micro-heaters used in infra-red (IR) micro-emitter chips, based on CMOS technology. The temperature characterisation of the micro-heater is described using both electrical and the IR thermal microscopy (discussed in Chapter 3). The radiance emission performance and reliability of the thermal IR micro-emitter chip (described in section **6.2**) is very dependent on the operating temperature and its uniformity across the micro-heater, which is embedded within a silicon dioxide membrane [1]. Therefore it is necessary to make accurate temperature measurements. As fully discussed the accuracy of the IR thermal measurement is limited by the optical transparency of the semiconductor layers forming the membrane heater (Chapter 3, section **3.1.3**), which has poor emissivity when compared to a black body source. Therefore, a high emissivity carbon microparticle infra-red sensor (MPIRS) (described in Chapter 4) was used to improve the accuracy of the IR temperature measurements. IR thermal microscopy is capable of producing a two-dimensional (2D) real-time thermal maps (described in Chapter 3) across the surface of the miniature micro-heater which is an integral part of the IR micro-emitter. The thermal map can then be used to analyse the temperature uniformity across the surface of the micro-electro-mechanical systems (MEMS) micro-heater and to identify any hotspots, which may lead to early failure of the device.

During IR temperature measurements on the IR micro-emitter chips, it was observed at high DC input power the device operating voltage decreased as the current was increased. This suggested the device electrical parameters were initially changing with increasing DC input power due to the rising temperature of the micro-heater structure. This effect was noted on a number of chips and to stabilise the effect, electrical burn-in tests were conducted and analysed.

6.2. Device design details:

The micro-heaters, an integral part of the IR emitter chip (supplied by ams sensors Ltd, Cambridge), are based on tungsten metallisation technology, which can be heated to high operating temperatures [2]. The device typically operates at temperatures around 500 °C [2] to thermally generate optical emission for mid-IR spectroscopy applications, including optical gas sensing (discussed in section **5.3.3** of Chapter 5) [3]. The chip-scale source has the advantage of having a smaller physical envelope, compared to the micro-bulb based IR source, and can be assembled in a surface mount package.

The IR emitter (die size 1.76mm × 1.76mm) was fabricated using a 1.0µm CMOS process at a commercial foundry [4]. The CMOS based IR emitter chip has a miniature tungsten heater, consisting of a circular multi-ring structure (800µm diameter), embedded within a 5µm thick, 1200µm diameter circular silicon dioxide (SiO_2) dielectric membrane, passivated with silicon nitride (Si_3N_4). The circular design of the membrane allows for uniform intrinsic stress distribution at the membrane's edge [5] by reducing the mechanical stresses. Silicon

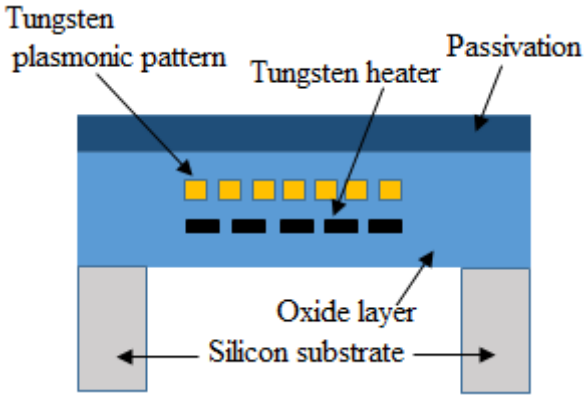

Figure 6.1: Schematic cross-section of the IR micro-emitter (not to scale).

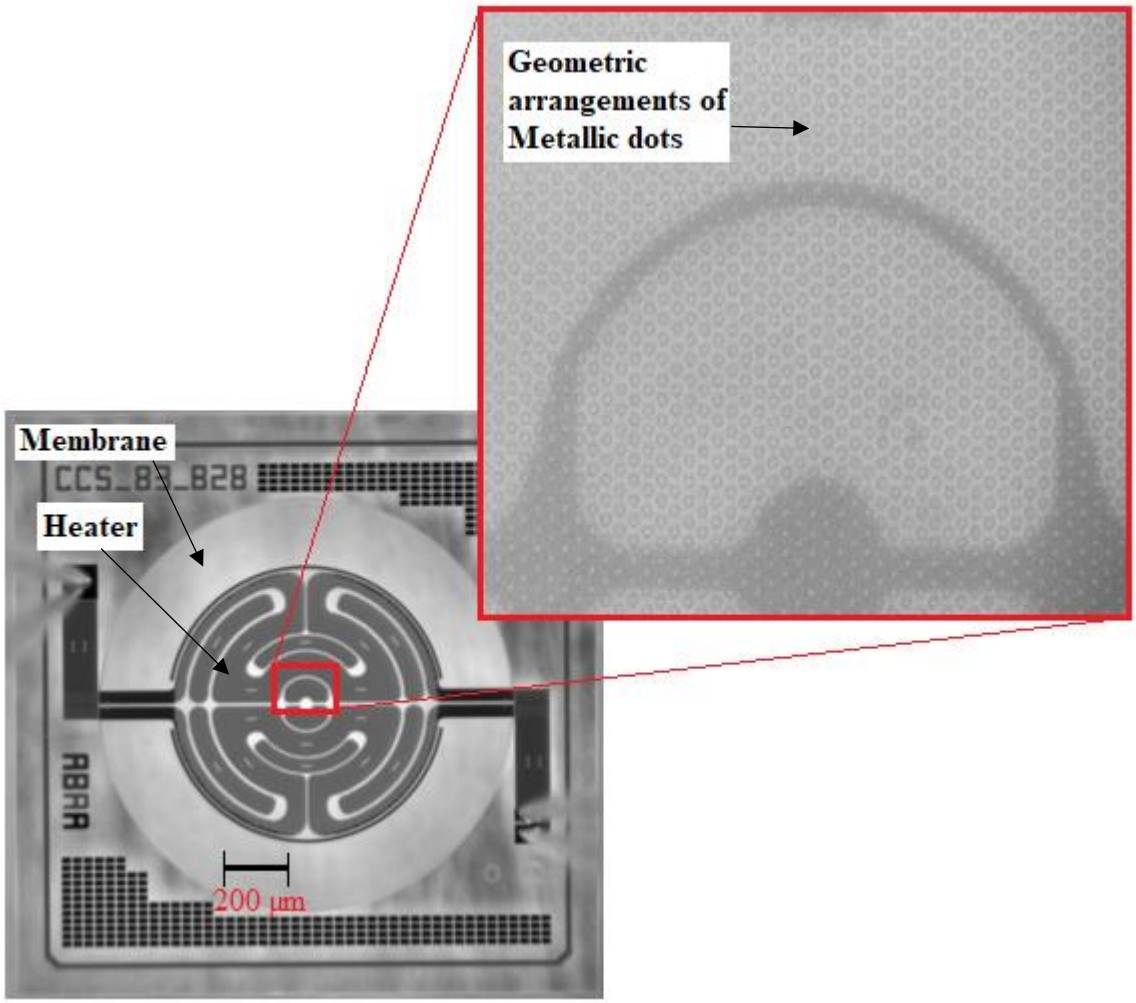

Figure 6.2: An optical image showing the top surface topology of the fabricated IR emitter chip.

oxide layers are used as inter-layer dielectrics. The membrane was formed as a post-CMOS process by the same external foundry, using Deep Reactive Ion Etching (DRIE) of the silicon substrate with the first buried silicon dioxide layer acting as an effective etch stop. The membrane thermally isolates the micro-heater from the substrate, ensuring efficient heating, fast thermal transient response and low power consumption. The emitter utilises a plasmonic

structure to enhance IR emission, which is formed by a geometric arrangement of metallic dots in a metal layer. Two metal layers were used, one to form the plasmonic structure and the other one for the heating element. In operation, electrical power is applied to the micro-heater element which increases its temperature to over 500 °C. The heater element emits IR radiation over a broad spectrum of the mid-IR waveband (2.5µm – 15µm) [3]. Figure 6.1 shows a schematic cross-section of the device and its layered structures and Figure 6.2 shows an optical micrograph and top surface topology of the fabricated chip.

6.3. Electrical burn-in experiment and IV characterisation of IR micro-emitters:

During the initial conventional IR temperature measurement tests on the micro-heaters, it was observed at high DC input power (in excess of 500mW) the operating voltage decreased as current was increased. This suggests the device electrical parameters were changing with temperature as the DC input power was increased. To assess this observation and to stabilise the effect, some electrical burn-in tests were conducted and the IV characteristics of the IR micro-emitters were analysed.

6.3.1. IV Measurement system:

The IV characteristics of the IR micro-emitters were measured using 4-point DC probe (Wentworth Laboratories PVX400) measurement set-up. The probes had a magnetic base to attach them to the anti-vibration table, which is a part of the IR and optical measurement set up (as described in Chapter 3, section **3.2.1** in Figure 3.5). The IV measurement system utilised a DC power supply (PL303QMD-P Quad-mode) from Aim-TTi to supply the voltage across the DUT (the IR micro-emitter). To measure the input voltage more accurately additional voltage sense probes (Wentworth Laboratories PVX400) and a 34005A multi-meter from Agilent was used. To measure the resulting current a DM200 digital multi-meter from Digimess was used. The schematic arrangement of the basic 4-probe IV measurement setup is shown in Figure 6.3.

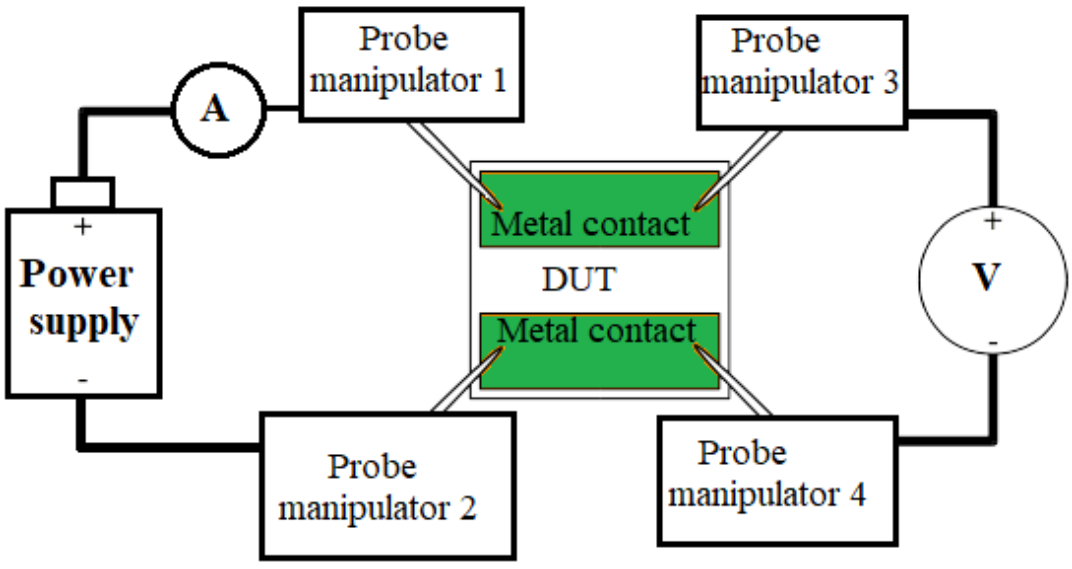

Figure 6.3: Schematic arrangement of basic 4- probe I-V measurement setup.

6.3.2. Electrical burn-in and IV characterisation results:

Initial electrical burn-in tests were undertaken on an untested IR micro-emitter of fabrication batch (device CCS113C-Chip-C7). The device was DC biased to high power, input DC power of ~514.2mW (I= 120mA and the initial voltage was noted as 4.285V). The changes to the IV characteristics with respect to time were monitored and recorded and are shown in Figure 6.4 (the results are also provided in a table in Appendix – 6A). The IV measurements were made at a base-plate temperature of 80 °C.

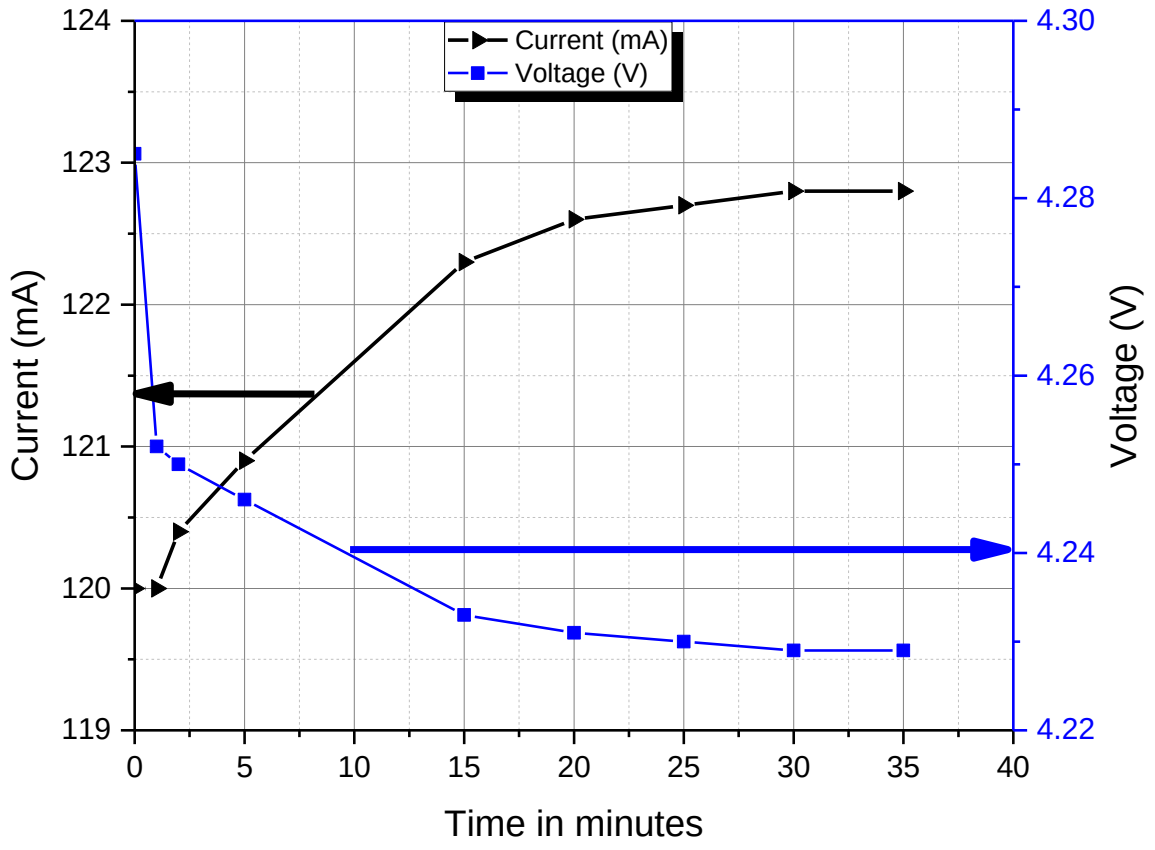

Figure 6.4: Initial IV characteristics of an untested IR micro-emitter (device CCS113C-Chip-C7).

The results indicate the electrical parameters of an IR micro-emitter become more constant with time after 15-20 minutes of electrical burn-in at high DC input power (~514mW). To verify this observation, the device was continuously powered '**ON**' at high power (at ~514mW) for ~35 min and the IV characteristics were measured and recorded. The device was then switched **'OFF'** for ~30 min and the IV measurements repeated for a second time. The comparison between the IV characteristics of an IR micro-emitter chip which were measured after the electrical burn-in at high DC input power is shown in Figure 6.5, and the result showed almost identical IV characteristics between the two sets of measurements.

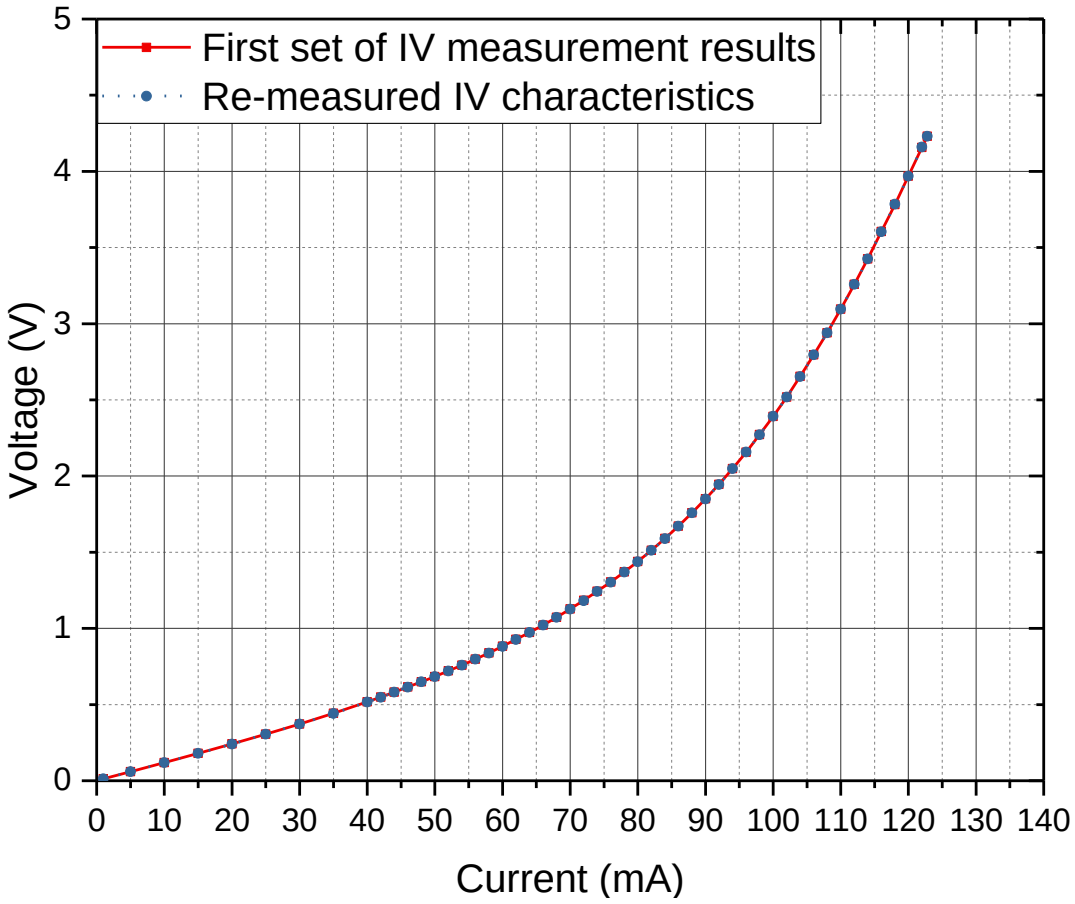

Figure 6.5: Comparison between the IV characteristics after electrical burn-in the device (CCS113C-Chip-C7) at high DC input power (~514mW).

To further verify this observation and to validate the consistency of results, the high power burn-in measurements were repeated on another device (device CCS113C-Chip-C8 from the same fabrication batch as CCS113C-Chip-C7). Initially, the IV measurements were made without an electrical burn-in. Then the device was burnt-in by continuously applying a DC bias at a high DC input power (~539.8mW) for time period of ~35min. The IV measurement was then re-measured before switching the device '**OFF**'. The input DC power to the device remained switched **'OFF'** for ~30min. The IV characteristics were then again measured for a third time. All three IV plots are compared in Figure 6.6. As can be seen from the graph, the results indicate that to obtain a stable IV characteristic with time the devices should be DC burnt-in at a high DC input power and over time period of at least ~30 minutes.

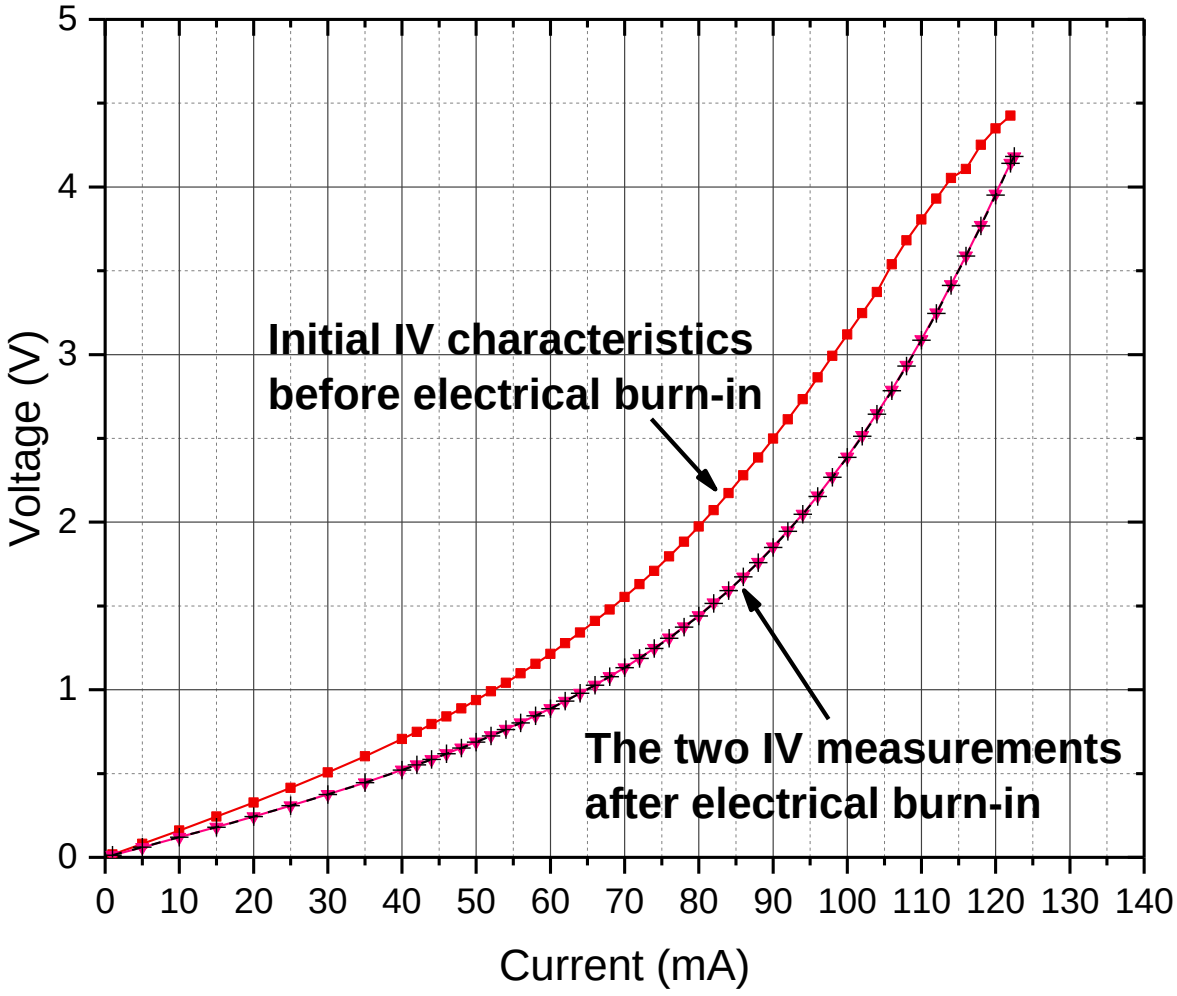

Figure 6.6: Comparison between the IV characteristics of an IR micro-emitter (device CCS113C-Chip-C8) before and after electrical burn-in.

The results show the resistance of these IR emitter devices become more consistent with increased temperature over time. The annealing process at high temperatures on these devices will stabilise the surface chemical composition and the metal contact layers.

6.4. IR thermal measurement procedure:

The IR thermal measurement technique was used to study the temperature distribution across the micro-heater membrane of these low power low cost novel IR micro-emitter chip devices. Initially, the conventional IR thermal microscopy was utilised to obtain the peak operating temperature of the IR micro-emitter. These measured temperature results were then compared to the calculated temperature results obtained using an electrical approach, in which the coefficients of resistance as a function of temperature of the micro-heater are used (will be described in section **6.4.1**). The conventional IR temperature measurements were also compared with the temperature results obtained using the MPIRS technology (a detailed description of this measurement method was described in Chapter 4).

To make the measurements, the IR emitter chip after electrical burn-in was mounted on an aluminium base-plate, which in turn was mounted on a Peltier heater to control the base-plate temperature (ambient temperature). A calibrated K-type thermocouple was embedded in the base-plate to monitor its temperature. The base-plate with the mounted IR emitter chip was positioned underneath in a vertical alignment with the objective lens of the Quantum Focus Instruments (QFI) infra-red microscope (Infrascope II). A schematic of this experimental arrangement is also shown in Figure 3.1, in Chapter 3. The QFI instrument has been modified during this research work, for high temperature detection (>500 °C), with a maximum thermal spatial resolution of ~3μm (using a ×25 lens objective) [6]. A detailed description of the IR thermal microscopy measurement system was described in Chapter 3 (section **3.2**).

As described in Chapter 3, the surface emissivity (ε) characterises the radiative efficiency of a material compared to that emitted by a black body at the same temperature and spectral bandwidth. The surface emissivity mapping of the IR emitter chip, taking into account the background radiation (including reflected radiation from the topology), was measured using the two-temperature emissivity approach which is fully described in Chapter 3 (section **3.1.2.2**).

$$\varepsilon = [R_{T1}(\lambda) - R_{T2}(\lambda)]/[R_{b1}(\lambda) - R_{b2}(\lambda)] \qquad \textbf{(6.1)}$$

Where, $R_{T1}(\lambda)$ and $R_{T2}(\lambda)$ are the IR emission levels (W/m^2.str) from the surface of an IR micro-emitter at two known temperatures T_1 and T_2, and $R_{b1}(\lambda)$and $R_{b2}(\lambda)$ are the respective equivalent black body emission levels (W/m^2.str) at temperatures T_1 and T_2.

The radiance data was then used by the IR system software to calculate the surface emissivity map (at every pixel) across the surface of the micro-heater. During the process of emissivity measurement, there was some sample movement noticed as a result of the thermal expansion of the base-plate. If left uncorrected, the shift in sample location will cause errors in the pixel alignment between the two sets of radiance data taken from the two radiance images captured at two temperatures. This will result in errors in the surface emissivity. This sample movement was corrected by mechanically realigning the objective lens of the IR microscope between the lower and higher temperatures using an alignment mark on the micro-heater. After emissivity mapping, IR temperature measurements were made on the surface of the IR micro-heaters.

To make the temperature measurements on the micro-heater samples, DC probes (using 4-point probe measurement system which is described in section **6.3.1**, to eliminate the effect of contact resistance) were used to make electrical contact to the chip, which was biased with the DC power supply (TTI PL303QMD-P Quad-mode). All of the devices were DC burnt-in at a high DC input power for ~ 30min (as discussed in section **6.3.2**) before making the IR thermal measurements. The electrical burn-in is required on these devices to stabilise the metal contact layers and they become more consistent at increased temperatures over time. All thermal measurements were made at a base-plate temperature of 80 (±0.5) ^{0}C. This temperature was chosen to give an adequate IR detector signal-to-noise ratio.

6.4.1. Conventional IR temperature measurement results and compared with electrical temperature measurement results:

Conventional IR thermal measurements were first made on the micro-heater of the IR emitter chip (device CCS113C-Chip-J1). The IR emitter chip was DC biased over a range of input powers (0 to 240mW) and for each input power, a 2D thermal map of the emitter chip was recorded and the peak temperature was identified, using conventional IR microscopy. The ×5 objective lens which has a field of view 2.3mm × 2.3mm and a thermal spatial resolution of ~5µm [7] was initially used for thermal imaging. The measured temperature profile is plotted as a function of the DC input power and shown in Figure 6.7.

As a direct comparison, the temperature of the heater element of the same IR emitter chip (CCS113C-Chip-J1) was also calculated using an electrical method [2], [8], which will provide the average temperature of the heater membrane. For this method, the temperature dependant resistance of the heater was measured for each input power, taking into account the chip input feed resistance. Knowing the temperature coefficients of the heater resistance, the average temperature of the heater can be calculated using the expression shown in **(6.2)**.

$$R = R_0 [1 + TCR_1 (T - T_0) + TCR_2 (T - T_0)^2] \qquad \textbf{(6.2)}$$

Where, T_0 = ambient temperature,

T = heater temperature,

R = resistance at temperature T

R_0 = resistance at ambient temperature T_0 and

TCR_1 = Linear temperature coefficient of resistance (9.66×10^{-4} for CCS113C-PVD devices)

TCR_2 = Quadratic temperature coefficient of resistance (1.0×10^{-12} for CCS113C-PVD devices)

The two temperature coefficients of resistance for the batch of devices measured were provided by ams Sensors, UK Ltd (DMU was not able to make these measurements as a high temperature (to temperatures approaching 700 °C) chuck was not available).

The calculated average temperature profile as a function of DC input power of the micro-heater using the electrical method, was compared with the peak temperature obtained by the conventional IR measurement method. The comparison of the results is shown in Figure 6.7.

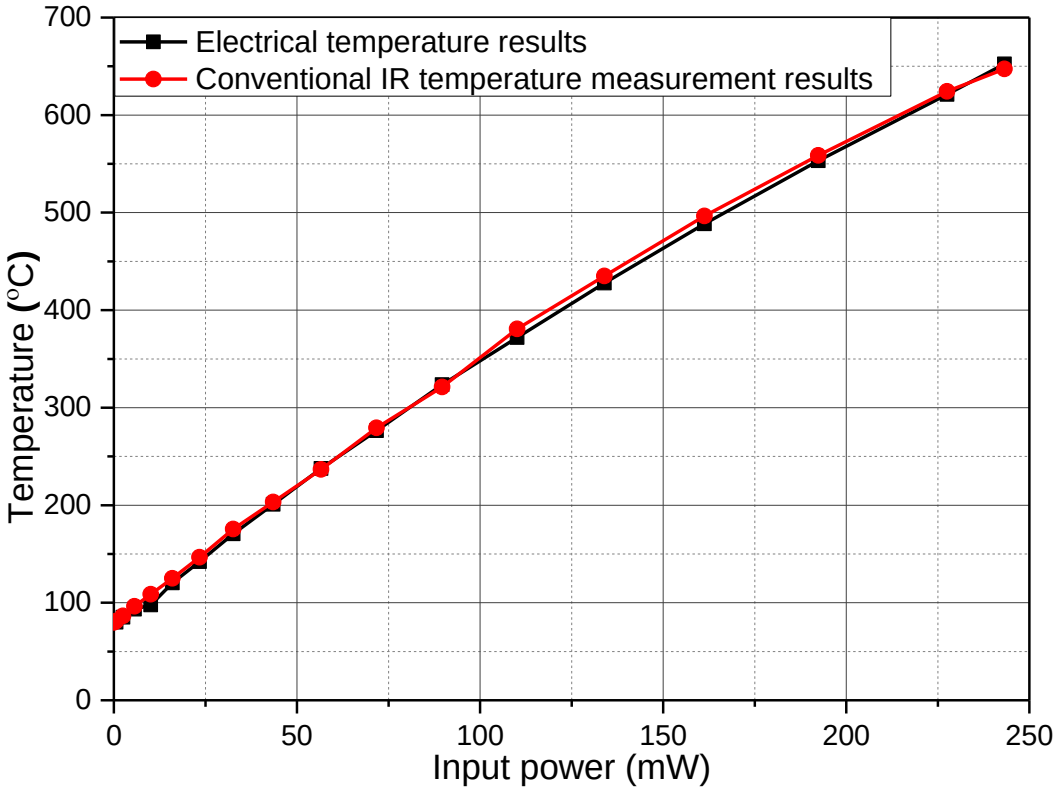

Figure 6.7: The comparison between conventional IR and electrical temperature measurement results measured on IR micro-heater.

As seen in Figure 6.7, both temperature profiles for the IR measurement and electrical method were comparable, showing good agreement over the temperature range. The results indicate the peak temperature obtained from the IR method is very similar in magnitude to the average temperature obtained from the electrical method suggesting that the temperature is uniform across the heater surface.

6.4.2. Temperature uniformity measurement results:

Conventional IR thermal measurements were also utilised to perform quick thermal profiles to show the thermal distribution across the heater structure of the IR emitter chips as well as to identify the location of any hotspots. To measure the temperature uniformity across the whole heater membrane (800µm in diameter size), a ×5 objective lens was used for thermal imaging. To investigate the consistency of the temperature uniformity of the heater, thermal maps of five IR micro-emitter chips from the same fabrication batch (CCS113C-Chips) were measured.

All of the five thermal maps showed reasonably good thermal uniformity across the heater of the IR micro-emitter chip (an example is shown in Figure 6.8 (a)), with a maximum temperature variation across the heater structure of ~3% (at high DC input power level ~240mW). The measurements therefore indicate reasonable uniformity and consistent temperature distribution across the heater membrane on all the emitter chips. These results suggest the average operating temperature obtained using electrical measurement technique will give a good approximation of the device actual operating temperature (i.e. the surface of the device contains very little temperature variation).

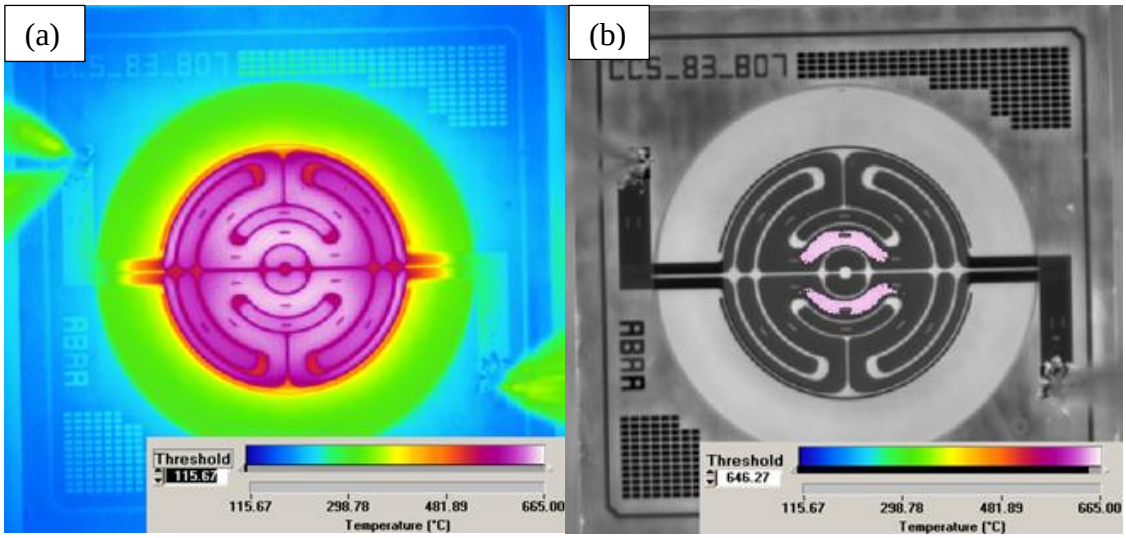

Figure 6.8: Infra-red thermal images of the IR emitter chip measured using ×5 objective lens ***(a)*** *Figure showing the thermal uniformity,* ***(b)*** *Figure showing the hotspots in the central ring of the heater structure.*

A small (~20 °C) elevation in temperature in the central ring of the heater structure was observed (Figure 6.8 (b)), which is more efficiently thermally insulated from the substrate. The uniformity of the observed temperature elevations (hotspots) from device to device of same fabrication batch (CCS113C-Chips) was also analysed and shown in Figure 6.9. The measurement results show that the localised hotspots are broadly similar in location and uniform for the different IR emitter chips of same fabrication process batch.

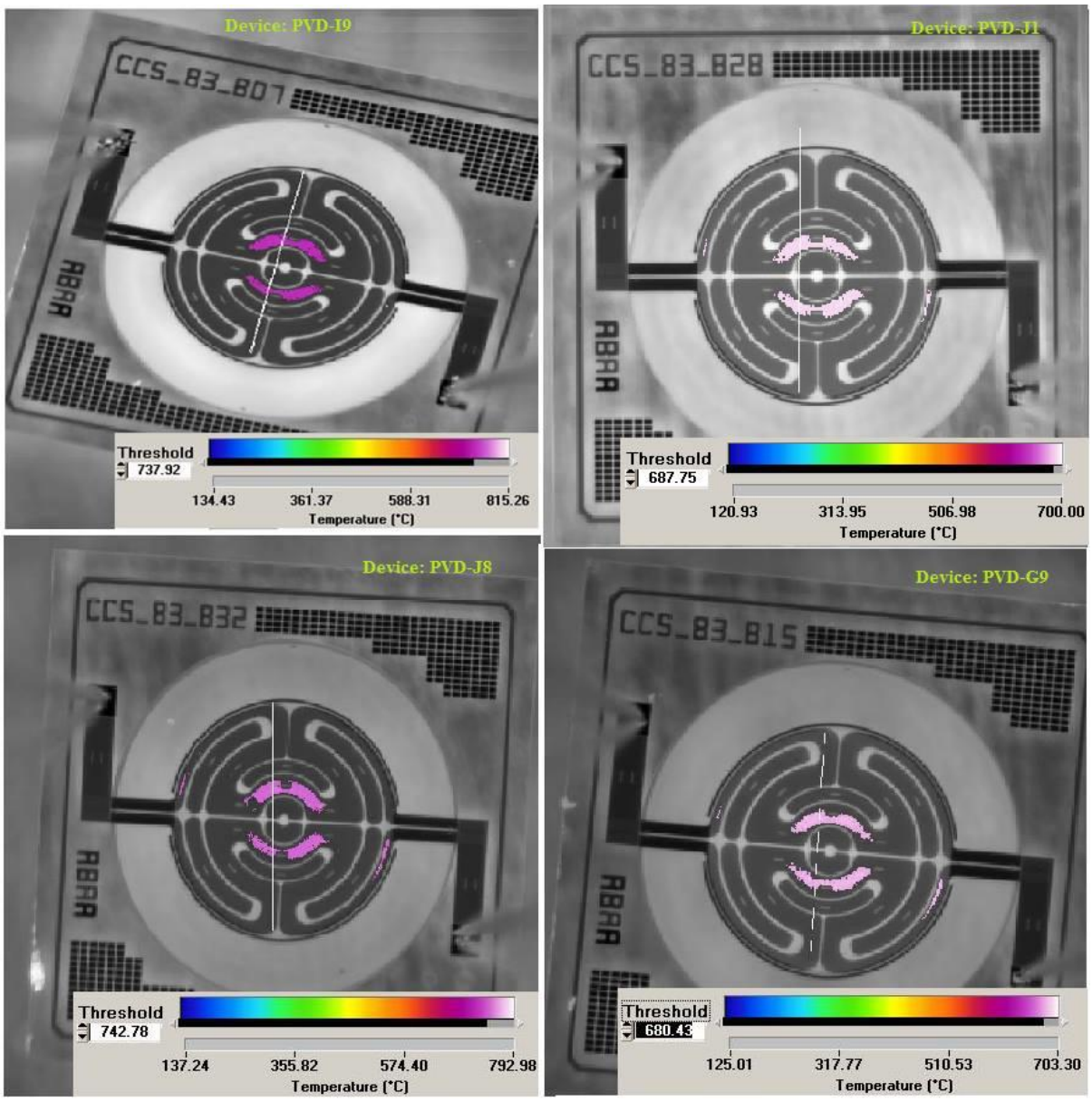

Figure 6.9: Figure showing the uniformity of hotspots on different IR emitter chips.

6.4.3. Consistency of IR peak operating temperature measurement results:

To investigate the slightly hotter areas in the central ring of the heater in more detail, the IR temperature measurements were repeated on the 5 micro-heaters (IR micro-emitter chips from the same fabrication batch CCS113C-Chips). The measurements were made using the ×25 objective lens (giving a field of view 464µm × 464µm and a spatial resolution of ~3µm) which covers the central part of the micro-heater where the temperatures are elevated.

The IR emitter chip was biased under DC operating conditions over a range of input powers (0 to ~260mW) and the peak temperature of the heater membrane was recorded for each bias point. The measured temperatures were plotted as a function of the DC input power. A comparison of the peak temperature profiles of the heater membrane of the 5 micro-emitter chips are shown in Figure 6.10.

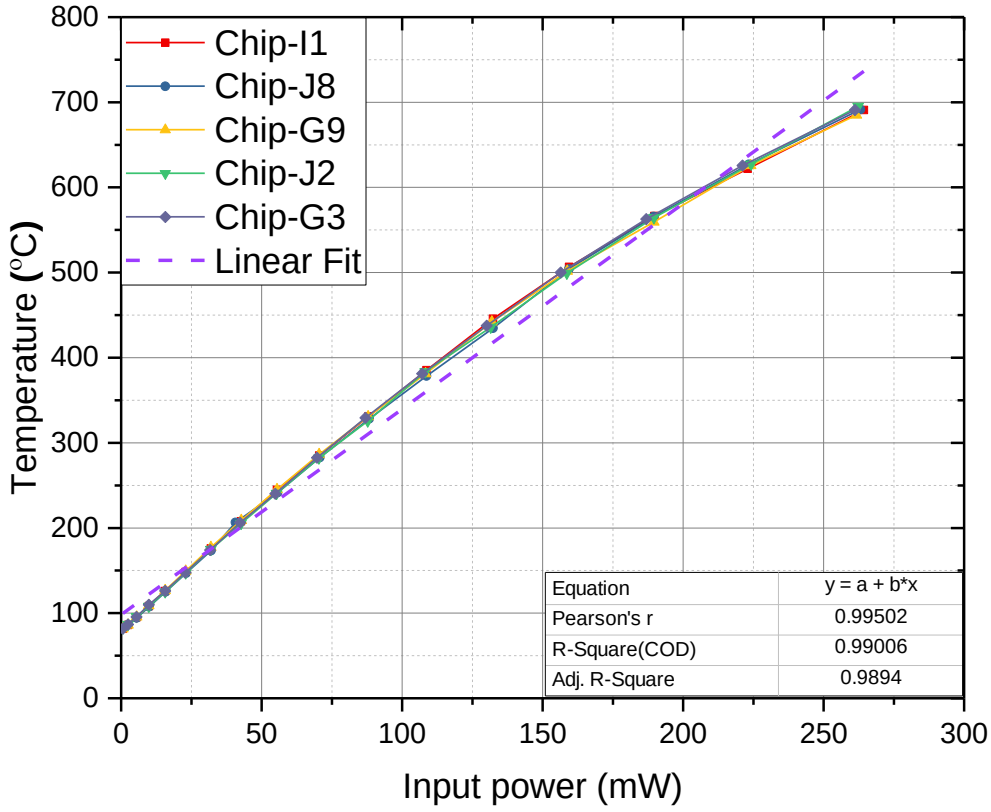

Figure 6.10: IR temperature measurement results measured as a function of the DC input power, and compared in 5 different IR micro-emitters.

As expected, the temperature increases linearly with increased DC power and all 5 chips gave a very similar peak temperature profile over the same range of DC input powers. The consistency of the peak temperature measurement results indicate the fabrication process of the micro-heaters (IR micro-emitter chips) must be reasonably consistent for different chips from the same process batch.

6.5. IR temperature measurements using a microparticle IR sensor:

The accuracy of the temperature measurements made using IR thermal microscopy is dependent on the radiative properties of the device under test (DUT). As discussed (in Chapter 3, section **3.1.3**), if the device has a low surface emissivity or is optically transparent to IR radiation then it will suffer from temperature errors [9]. To overcome these limitations of IR thermal measurement and to improve the temperature accuracy on the thin semiconductor layer of the micro-heater, the MPIRS (discussed in Chapter 4) was used. In this temperature measurement method, the results are not dependent on the surface emissivity of the device being measured, but only on the surface emissivity of the MPIRS, which was calibrated directly against a black body before the thermal measurement.

6.5.1. Temperature measurement results:

A high emissivity MPIRS (amorphous carbon sphere) [10], was used for the first time to make high temperature measurements (approx. 650 °C) on the micro-heaters. In this experiment, a single MPIRS, having a diameter of ~15µm was placed using a Scientifica micro-manipulation probe (the micro-manipulation process was fully described in Chapter 4) in isothermal contact on the surface of the IR micro-emitter.

The measurement was carried out on the same IR emitter chip (CCS113C-Chip-J1), as used for the conventional IR measurement described in section **6.4.1**. The MPIRS was placed at the hotspot identified on the inner ring of the heater membrane by the conventional IR measurement. An optical micrograph showing the MPIRS placed on the surface of the heater membrane at the hotspot is shown in Figure 6.11.

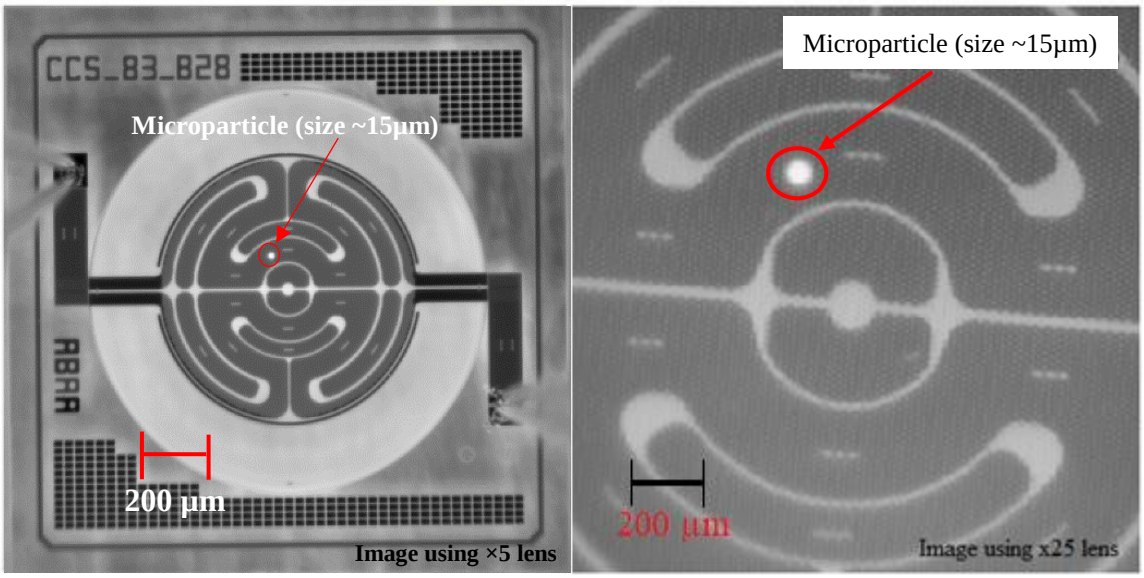

Figure 6.11: IR reference image showing the microparticle sensor placed on the heater of the IR emitter chip.

To make a more accurate temperature measurement at the hot-area of the heater membrane, the surface emissivity of the MPIRS was measured using the two-temperature emissivity approach [9]. The radiance images were taken at two elevated temperatures of $T_1 = 65\ °C$ and $T_2 = 95\ °C$ respectively. The measured surface emissivity of the MPIRS was found to be ~ 0.7 (note this value was used before the improved MPIRS calibration which includes taking into account background radiation as discussed in Chapter 4, section **4.4.7**) and is shown in Figure 6.12. The measured surface emissivity of the semiconductor layers forming the membrane heater was low (~0.3) due to the transparency of the semiconductor layers to IR radiation and high reflectivity of the under-laying metal track.

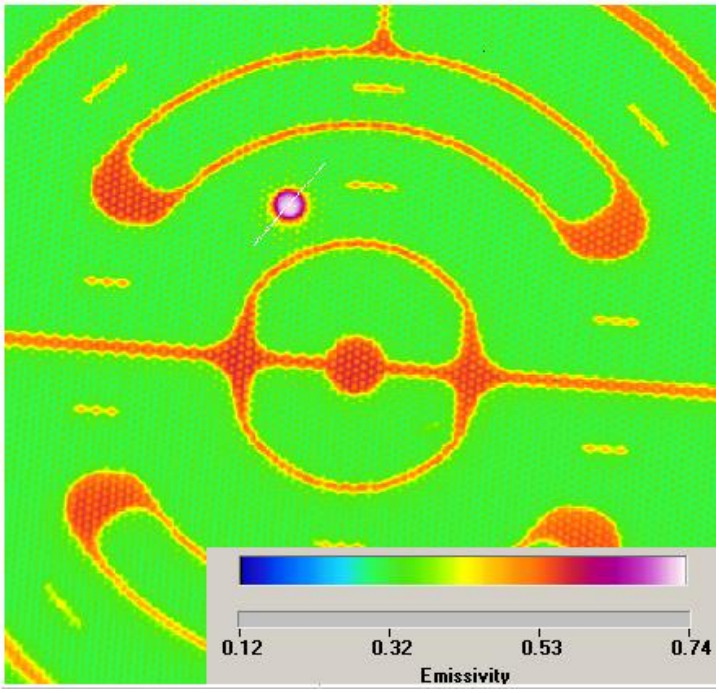

Figure 6.12: An emissivity map of the MPIRS (size ~15 µm in diameter) placed on the surface of the IR micro-emitter.

The DC bias was applied to the micro-heater and the temperature (using the ×25 objective lens of the IR microscope) of the MPIRS was recorded for each bias point. Figure 6.13 shows the temperature of the hotspot measured using the MPIRS and compared with the peak temperature measured using conventional IR at the same x and y coordinate position on the chip. The range of the DC input operating power for both measurements was (0 to 240mW). The temperature difference between the MPIRS and the conventional IR measurement was approximately 15 °C. Conventional IR thermal measurements tend to underestimate the device operating temperatures due to the uncertainty in the surface emissivity as already discussed in Chapter 3 (section **3.1.3)**. The MPIRS technique reduces some of the uncertainty in the surface emissivity, providing a more exact measurement of surface temperature of the micro-heater.

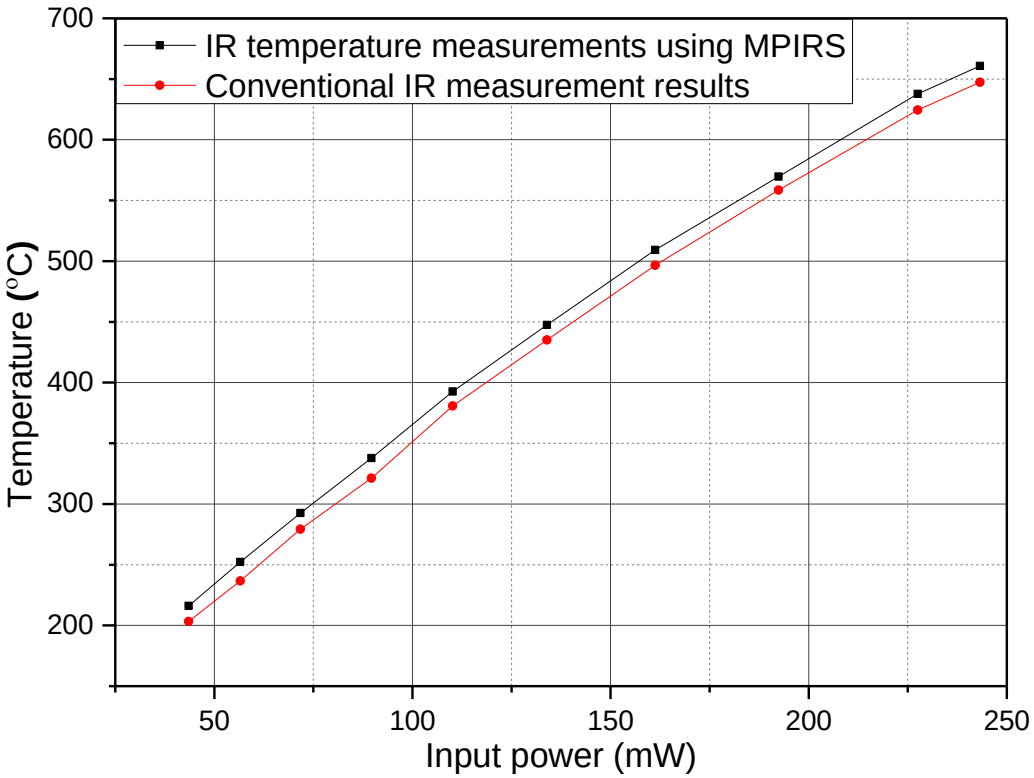

Figure 6.13: Comparison between conventional IR temperature results and measurements made using the MPIRS on the emitter chip.

Figure 6.14 (a) and (b) show IR thermal images of the MPIRS placed on the electrically biased micro-heater (device CCS113C-Chip-J1) membrane and is hotter than the surrounding chip surface temperature which has been computed from the erroneous lower surface emissivity.

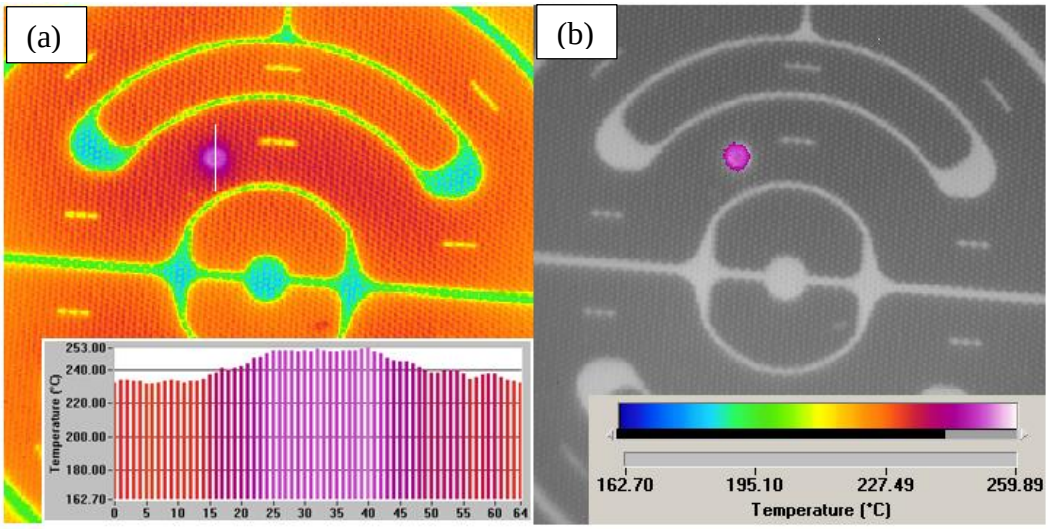

Figure 6.14: Thermal map of the micro-heater (CCS113C-Chip-J1) using MPIRS (bias level; I= 45mA and V=1.26) (a) MPIRS placed on electrically biased heater (b) MPIRS showing the hotter temperature than device surface temperature.

To further show the improved temperature accuracy of the MPIRS technique, the measurement was repeated on the MEMS micro-heater of a non-plasmonic (thermal emitter without plasmonic surface crystal structure [11] and very low surface emissivity ~0.1) semi-packaged (see Figure 6.15) thermal emitter chip (fabrication batch CCS-09-Chip). The author believes that, this is the first time the MPIRS techniques was used to make the temperature measurements on this type of packaged micro-electronic device. The micro-heaters of these thermal emitters have meander-shaped gold interdigitated electrodes and span a circular area of ~250µm in diameter with the gap between the interdigitated electrode fingers of ~10µm. The heating element which is made of tungsten is buried under the gold electrodes within the silicon dioxide membrane which has a diameter of ~640µm and a thickness of about 5µm [12], [13]. The device is ultra-low power and needs only ~33mW to reach 309 °C (See Figure 6.17).

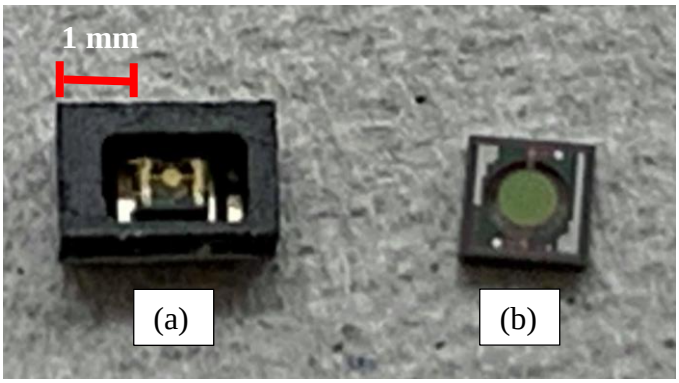

Figure 6.15: Optical photograph of fabricated devices (a) semi-packaged thermal emitter chip (CCS-09-Chip) and (b) previously measured bare die IR emitter chip (CCS113C-Chip).

It is obvious that the high reflectance/low emissivity of the gold electrodes is a problem when performing conventional IR measurements. Therefore, a MPIRS with a diameter size ~15µm was positioned on the surface of the micro-heater (CCS- 09-Chip) at the gold electrode using the micro-manipulator and the emissivity calibration was made using the two-temperature method, where, the two radiance images were captured at two elevated temperatures of $T_1 = 65\ °C$ and $T_2 = 95\ °C$ respectively. An emissivity map where the MPIRS shows the enhancement in emissivity (MPIRS emissivity is ~0.7) compared to gold electrodes (~0.1) is shown in Figure 6.16. The device was then DC biased, 1.47V, 22.6mA (equivalent input power is 33.2mW). An IR thermal image (measured using ×25 objective lens) showing the MPIRS on the gold interdigitated electrode of the electrically biased micro-heater is shown in Figure 6.17. The temperature measurement using the MPIRS gave a significantly higher temperature, ~59 °C greater than when the temperature of the gold electrode is directly measured using conventional IR microscopy.

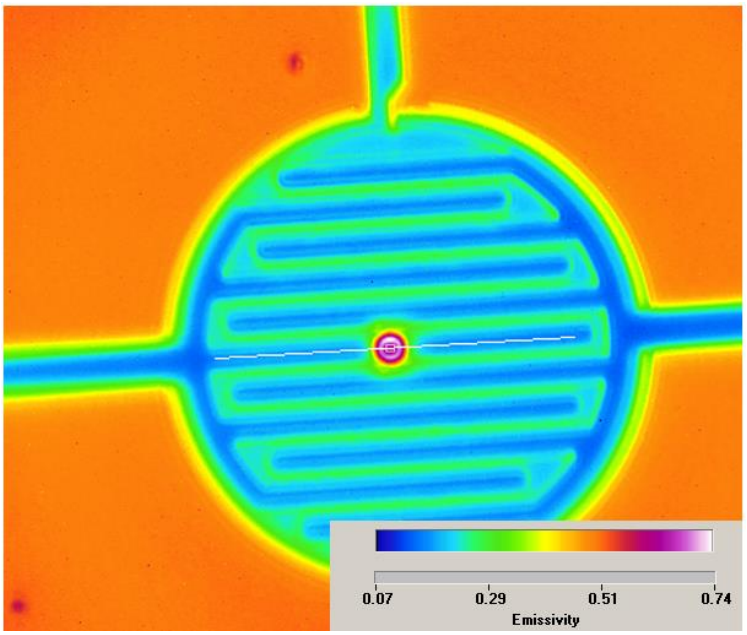

Figure 6.16: Figure showing the emissivity of a MPIRS (size ~15µm) when measured on the surface of a micro-heater with gold electrode of a non-plasmonic thermal emitter chip (CCS-09-Chip).

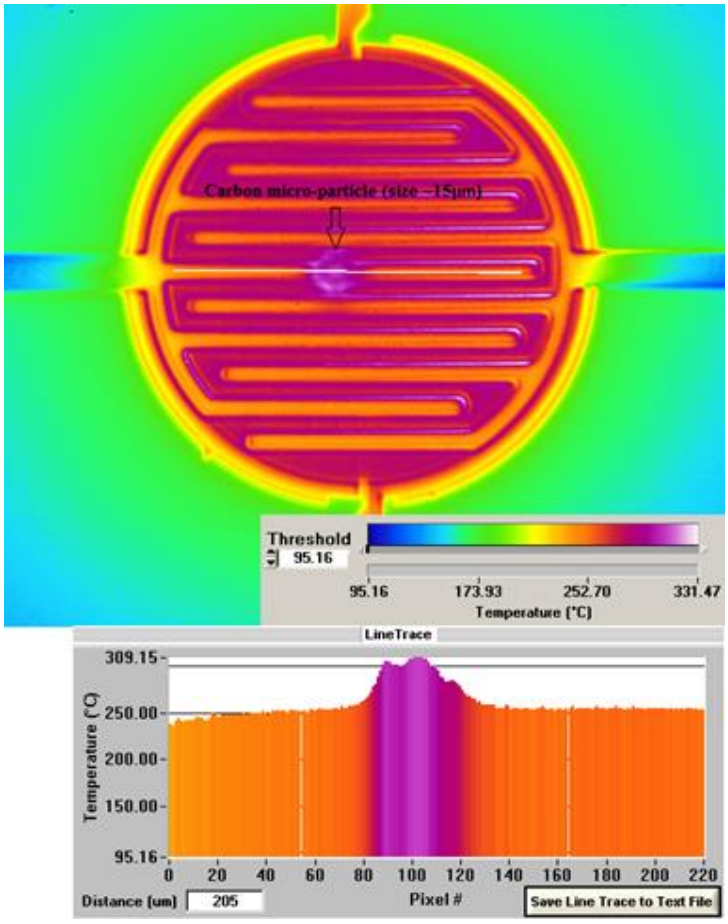

Figure 6.17: Figure showing an improved temperature measurement using a high emissivity MPIRS (size ~15µm) when measured on a low emissivity/ highly reflective gold electrode present on a surface of a micro-heater (CCS-09-Chip).

6.5.2. Effect of the MPIRS diameter size on temperature measurements:

As discussed in Chapter 4, the emitted radiance for sub- 10µm diameter particles is known to be lower than for larger particles (for example, 20µm in diameter) thereby leading to error in measured temperature. To verify the effect of MPIRS diameter on these specific IR temperature measurements, four different MPIRS of diameters ~3µm, ~15µm, ~21µm and ~43µm were used.

A single MPIRS of one of the above diameters was placed in isothermal contact on the surface of the micro-heater (IR micro-emitter device batch CCS113C-Chip-J3) at the hotspot location (discussed in section **6.4.2**), using the Scientifica micro-manipulation probe. The IR microscopy system with the ×25 objective lens was then used to record the temperature of the MPIRS as a function of the DC input power to the micro-heater. The same experiment was then repeated for each of the other three diameters. The results are shown in Figure 6.18.

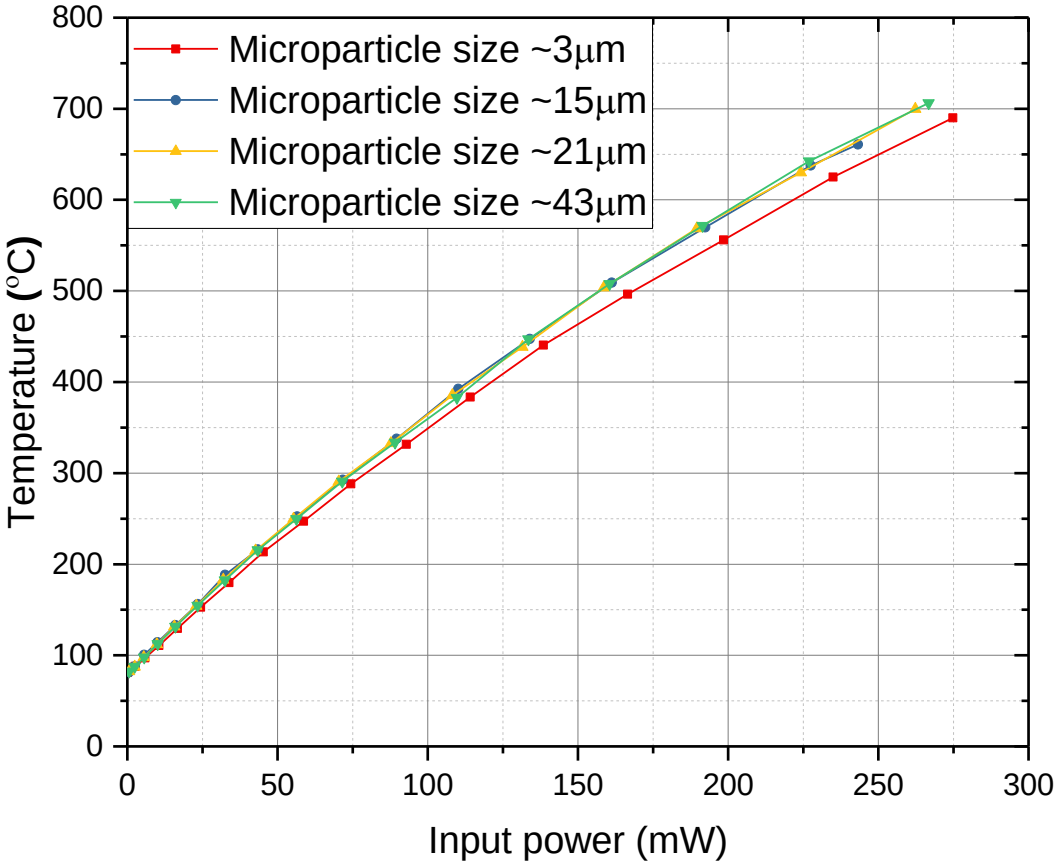

Figure 6.18: Graph showing the effect of MPIRS sizes on IR temperature measurements.

The results show the measured peak surface temperatures using MPIRS of diameters (>10µm) were well behaved and showed a very similar thermal profiles over the range of DC input powers to the micro-heater. However, when making the IR temperature measurement using the MPIRS of diameter ~3µm, the peak surface temperature was under-estimated. The reasons for this have already been fully discussed in Chapter 4 (section **4.4.2**).

6.6. IR thermal measurement results on improved design IR emitters:

6.6.1. Device design details:

An improved IR thermal emitter chip (also supplied by ams sensors Ltd, Cambridge) features an 800µm diameter circular multi-ring structure micro-heater embedded within a ~4.9µm thick, 1200µm diameter circular dielectric membrane, passivated with silicon nitride. The devices were designed to have a higher surface emissivity (when compared with earlier design fabrication batch CCS113C-Chips) and should provide an improved temperature uniformity. The micro-heater and interconnects utilises a high temperature tungsten metal as the resistive material. The IR emitters (chip size 1.7mm × 1.7mm) were fabricated in SOI CMOS technology, in a commercial foundry. The circular membrane was obtained with a post-CMOS DRIE of the silicon handling substrate, with the buried silicon dioxide layer acting as an effective etch stop [4]. Two tungsten metal layers were used; one to form the plasmonic structure to enhance the surface emissivity and the other one to form the high temperature heating element. The inter layer thicknesses of the dielectrics and the plasmonic layer design [4] were changed (compared with CCS113C-Chips), and the optical characteristics were optimised for enhanced IR emission. An optical image of this improved design IR emitter is shown in Figure 6.19.

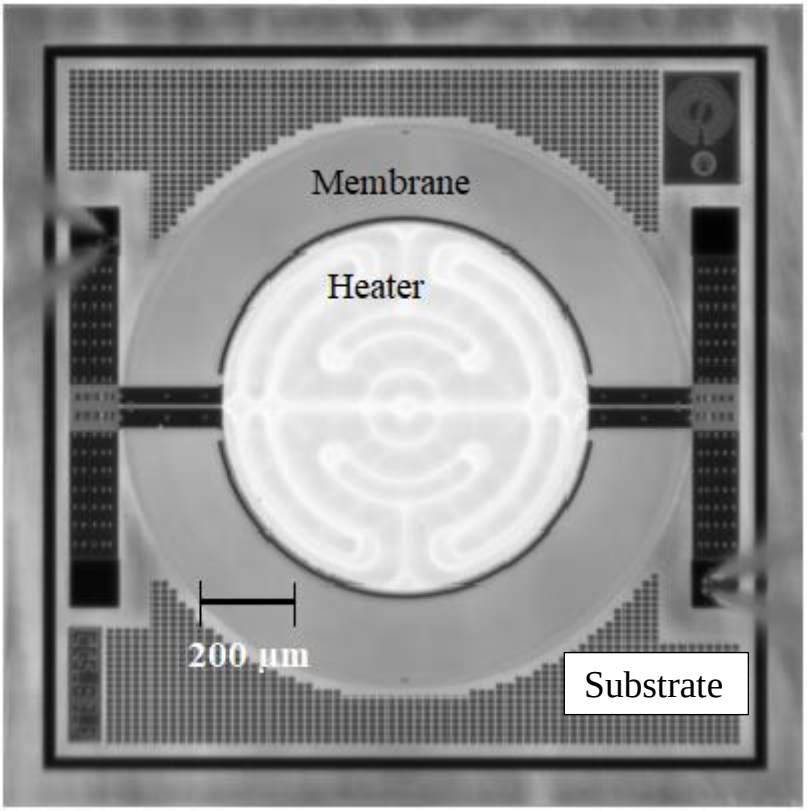

Figure 6.19: An optical image of an inproved design IR micro emitter chip (CCS-83-F-C4).

6.6.2. Temperature measurement results:

Conventional IR thermal microscopy was utilised to obtain the peak operating temperature and to show the thermal distribution across the heater membrane of the improved design IR micro-emitters (CCS-83-F). The surface emissivity of the IR emitter (device CCS-83-F-C4) was first measured using two-temperature emissivity approach, where, two radiance images were recorded at two ambient temperatures of $T_1 = 65\ °C$ and $T_2 = 95\ °C$. The surface emissivity map of the improved design IR micro-emitter chip is shown in Figure 6.20. The measurement result shows the surface emissivity of the redesigned IR micro-emitter is considerably higher (~0.6) when directly compared to the earlier fabrication batch (CCS113C-Chips) IR micro emitters (low surface emissivity ~0.3, see Figure 6.12). The surface emissivity of these devices is comparable to that of the surface emissivity of MPIRS. Therefore, there will be little difference in measured surface temperature using MPIRS method and conventional IR microscopy.

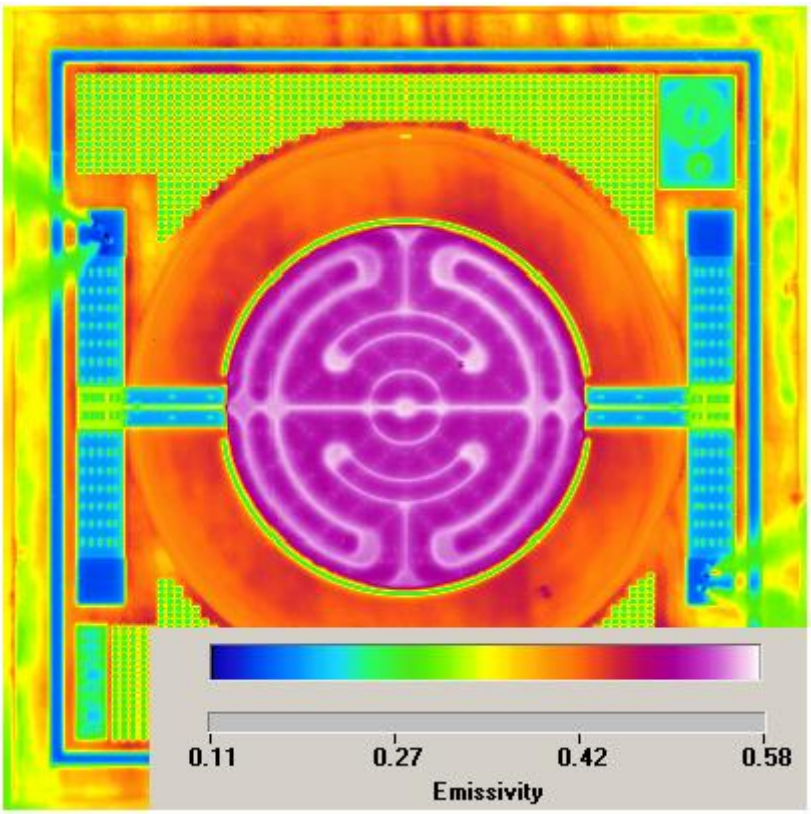

Figure 6.20: An emissivity map of the improved design IR micro-emitter (device CCS-83-F-C4) measured using ×5 objective lens.

The micro-heater was then DC biased over a range of input powers (0 to ~265mW) and for each input power the thermal map of the membrane heater was measured (using ×5 objective lens). An example of a 2D thermal map measured on electrically powered (at DC input power ~203.7mW) micro-heater is shown in Figure 6.21. The IR measurement result suggests an excellent thermal uniformity across the heater membrane from the improved design IR micro-emitter with maximum temperature variation across the heater membrane of less than 2% (at high input power level of ~265mW).

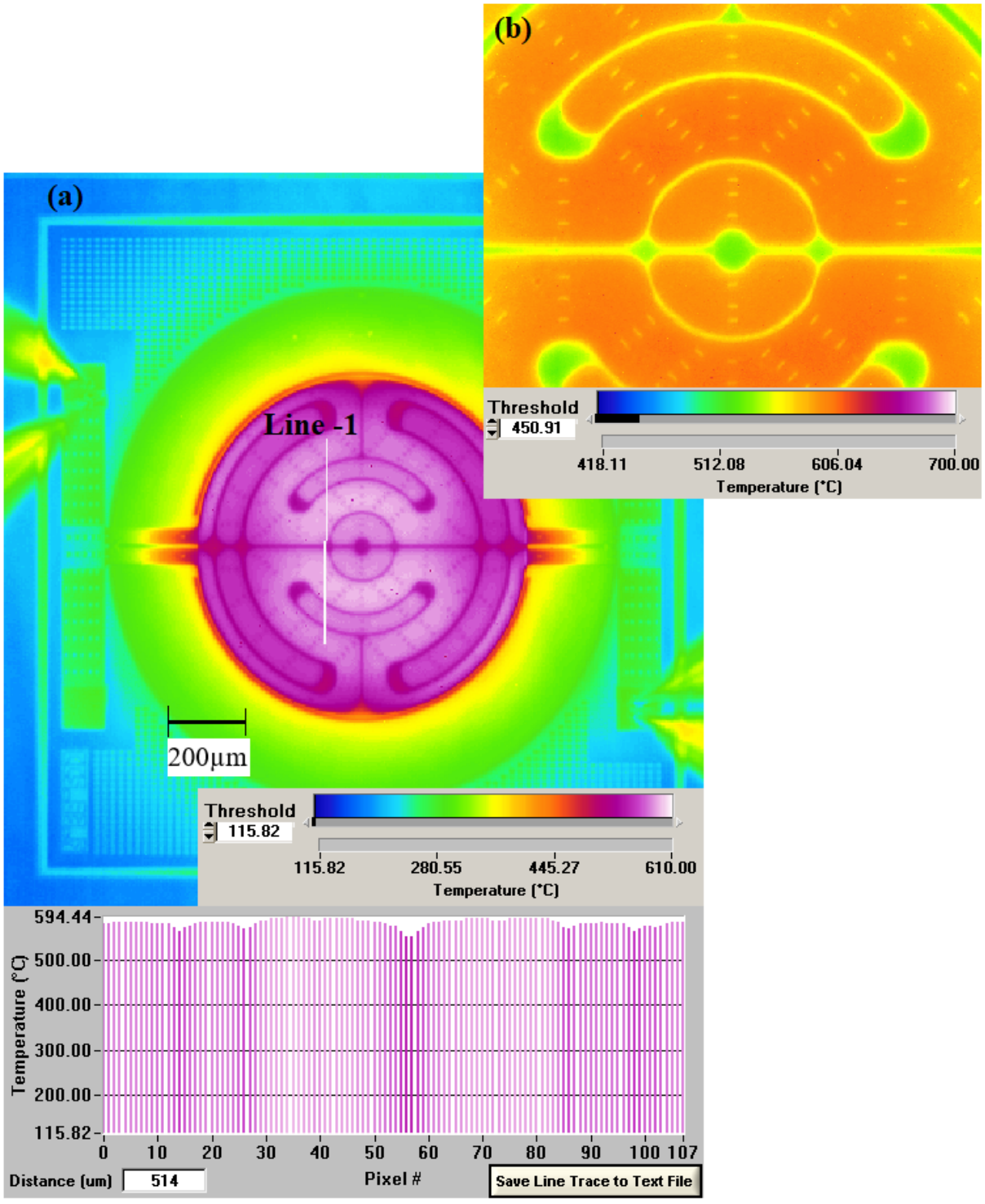

Figure 6.21: An example of conventional IR thermal image showing the temperature uniformity across the heater membrane of the improved design IR micro-emitter (CCS-83-F-C4) biased to ~203.7mW (a) measured using ×5 objective lens (b) measured using ×25 objective lens.

To further verify the temperature uniformity across the heater membrane of the improved design IR micro-emitters, the average temperature of the IR emitter chip (CCS-83-F-C4) was also calculated using the electrical method, by using the equation **(6.2)** and knowing the temperature coefficients of resistance (TCR_1 = 2.05 × 10^{-3} K^{-1} and TCR_2 = 3.0 × 10^{-7} K^{-2} ,provided by ams Sensors UK Ltd). The heater temperature obtained by IR measurement was compared to those obtained from calculated electrical measurement (as a function of input power) and the comparison is shown in Figure 6.22.

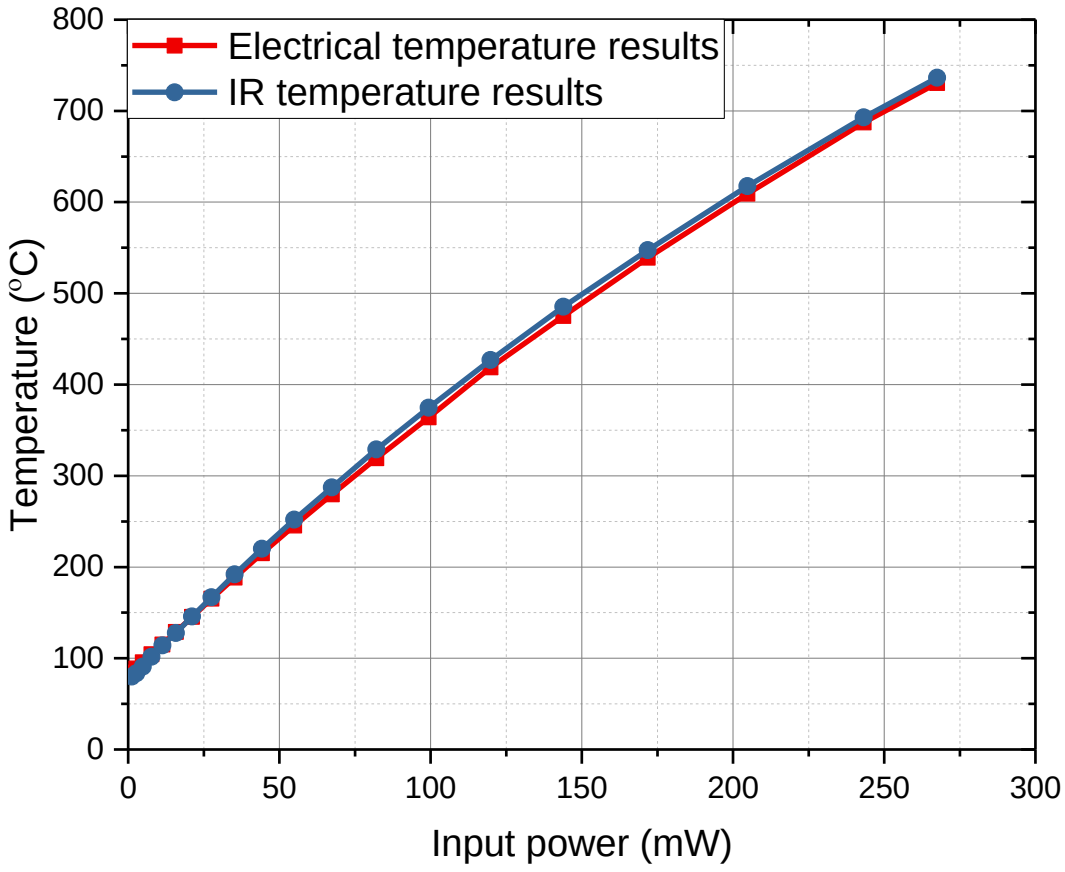

*Figure 6.22: Conventional IR temperature results compared with calculated electrical results on improved design IR micro-emitter (*CCS-83-F-C4).

Figure 6.22 shows the temperature reading obtained by both methods are in very good agreement over the same range of DC operating input power level (0 – 265mW), substantiating that the temperature is very uniform across the heater surface.

To investigate the consistency of the device operating temperature from device to device of the improved designed micro-heaters (IR emitters batch CCS-83-F), the experiment was repeated using the ×25 objective lens on 3 different samples. The measurement was made on an area of the heater membrane which appeared to be slightly hotter than in the surrounding area (the line '1' in Figure 6.21 shows the measured profile location). A comparison of the peak IR temperature profile recorded as a function of the DC input power is shown in Figure 6.23. The results indicate, there is a very good agreement between the peak temperature profiles of the three measured devices, over a range of DC input power (0-270mW); showing the excellent reproducibility from device to device from the same fabrication batch.

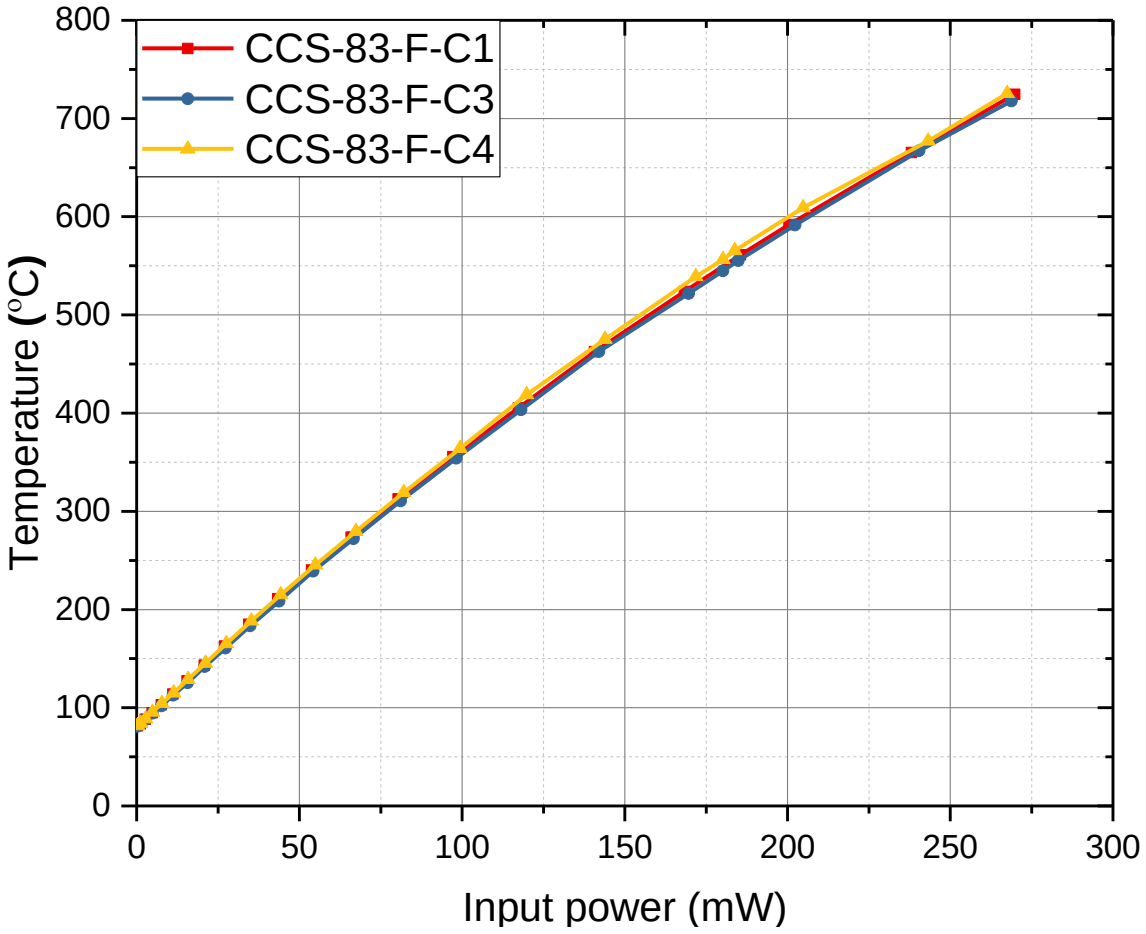

Figure 6.23: A comparison of the peak IR temperature profile measured (using ×25 objective lens) on 3 different chips of an improved design IR micro-emitters as a function of DC input powers.

Preliminary thermal measurements on the micro-heater of the improved IR emitter design (batch CCS-83-F) were also made using a thermo-reflectance technique at the QFI Bristol, UK facility to compare with IR temperature results. The thermo-reflectance measurement technique is explained in Chapter 2, section **2.3.2.2** of this thesis. Thermo-reflectance thermal imaging is dependent on the accurate measurement of the relative change in the device surface reflectivity as a function of the surface temperature of the sample [14]. The accuracy of the technique depends on the level of noise contribution from the detector, electronics and quantisation processes [15]. The thermo-reflectance measurement was not practical on these devices due to the multiple internal reflections from rough surface topology and the small fluctuation of heater membrane (the tension of the membrane changing with temperature). Therefore to-date no temperature profile results have been obtained for the heater membrane using the thermo-reflectance measurement technique.

6.7. Conclusion:

IR thermal microscopy was used to thermally profile the micro-heater of novel MEMS IR micro-emitter chips based on tungsten CMOS technology. During the preliminary IR measurements, the IV characteristics of these emitters were found to change due to temperature hysteresis effects when the chips were biased with a high input DC power. To verify this observation, electrical burn-in experiments were carried out and the results show the devices will require burn-in (for at least 30 min). Subsequently all the micro-emitters were electrically burnt-in at high DC input power (>500mW for ~30mins) prior to the IR temperature measurements.

IR imaging results indicate that the micro-heater of the IR emitter chip has good thermal uniformity and the conventional IR measurements are in reasonable agreement with calculated electrical average temperature results. Conventional IR thermal measurements underestimate the surface temperature of semiconductor layers due to uncertainties in their surface emissivity. It was shown the use of MPIRS measurement approach can reduce the uncertainties in the surface emissivity leading to improved temperature determination.

A high emissivity carbon based MPIRS was used to obtain an improved IR surface temperature measurement of the low surface emissivity micro-heaters. In the research presented in this chapter, the use of the MPIRS has been demonstrated, for the first time, to make an improved IR surface temperature measurements on high temperature micro heaters, to temperatures approaching 700 °C. The research work also demonstrated the first use of a single MPIRS for improved accuracy of temperature measurements on very low surface emissivity (<0.1) MEMS micro-heater in semi-packaging geometries. The results indicate that the conventional IR technique underestimates the device peak operating temperature and such underestimation can affect any predictions made on the device operating life-time.

The effect of the MPIRS diameter size on IR temperature measurement has been investigated. The result showed the smaller size (<10µm diameter) MPIRS has an effect on the level of IR radiation emitted from its surface (fully discussed in Chapter 4), leading to errors in the measured surface temperature of the device under test. Therefore, the MPIRS of diameter size >10µm should be used to obtain a more accurate measurement of the IR peak surface temperatures on low emissivity micro-heater membranes.

To obtain further improvements in the temperature uniformity across the heater membrane, the IR emitter chip was re-designed (by ams Sensors Ltd.), leading to a higher surface emissivity (~0.6). The emissivity of these IR micro-emitters is comparable to the emissivity of the MPIRS. Therefore, using the MPIRS technique will give little improvement to the conventional IR microscopy measurements. Conventional IR thermal microscopy was used to thermally characterise the heater membrane of the improved design IR micro-emitters. IR imaging results show the micro-heater of the chip has very good thermal uniformity with a maximum temperature variation across the heater structure of < 2% (at high input power ~265mW) and IR temperature results are in very good agreement with calculated electrical results as a function of DC input power. These heaters show an improved temperature uniformity over the original micro-heaters discussed in section **6.2** of this chapter.

6.8. References:

[1] P. Pandey, C. Oxley, R. Hopper, Z. Ali, and A. Duffy, "Infra-red thermal measurement on a low-power infra-red emitter in CMOS technology," *IET Science, Measurement & Technology*, vol. 13, no. 1, pp. 25–28, Aug. 2018, doi: 10.1049/iet-smt.2018.5427.

[2] S. Z. Ali, F. Udrea, W. I. Milne, and J. W. Gardner, "Tungsten-Based SOI Microhotplates for Smart Gas Sensors," *Journal of Microelectromechanical Systems*, vol. 17, no. 6, pp. 1408–1417, Dec. 2008, doi: 10.1109/JMEMS.2008.2007228.

[3] S. Z. Ali, A. D. Luca, R. Hopper, S. Boual, J. Gardner, and F. Udrea, "A Low-Power, Low-Cost Infra-Red Emitter in CMOS Technology," *IEEE Sensors Journal*, vol. 15, no. 12, pp. 6775–6782, Dec. 2015, doi: 10.1109/JSEN.2015.2464693.

[4] A. Pusch *et al.*, "A highly efficient CMOS nanoplasmonic crystal enhanced slow-wave thermal emitter improves infrared gas-sensing devices," *Scientific Reports*, vol. 5, p. 17451, Dec. 2015, doi: 10.1038/srep17451.

[5] A. De Luca *et al.*, "SOI CMOS MEMS Infra-red Thermal Source with Carbon Nanotubes Coating," *Procedia Engineering*, vol. 87, pp. 839–842, Jan. 2014, doi: 10.1016/j.proeng.2014.11.284.

[6] C. H. Oxley, R. H. Hopper, and G. A. Evans, "Improved infrared (IR) microscope measurements for the micro-electronics industry," in *2008 2nd Electronics System-Integration Technology Conference*, 2008, pp. 215–218, doi: 10.1109/ESTC.2008.4684352.

[7] R. Hopper, "Accurate temperature measurements on semiconductor devices," Ph.D., De Montfort University, 2010.

[8] S. Z. Ali, "Electro-thermo-mechanical study of membrane devices for smart IC technologies," Ph.D., University of Cambridge, 2008.

[9] P. W. Webb, "Thermal imaging of electronic devices with low surface emissivity," *IEE Proceedings G - Circuits, Devices and Systems*, vol. 138, no. 3, pp. 390–400, Jun. 1991, doi: 10.1049/ip-g-2.1991.0065.

[10] O. Stenzel, B. Rau, and G. Schaarschmidt, "Optical properties of amorphous carbon, deposited by an ion-plating technique," *physica status solidi (a)*, vol. 115, no. 2, pp. K247–K250, 1989, doi: 10.1002/pssa.2211150259.

[11] F. Morisot *et al.*, "ZnO based nanowire network for gas sensing applications," *Mater. Res. Express*, vol. 6, no. 8, p. 084004, May 2019, doi: 10.1088/2053-1591/ab1f60.

[12] F. Shao *et al.*, "NH3 sensing with self-assembled ZnO-nanowire μHP sensors in isothermal and temperature-pulsed mode," *Sensors and Actuators B: Chemical*, vol. 226, pp. 110–117, Apr. 2016, doi: 10.1016/j.snb.2015.11.109.

[13] S. Santra *et al.*, "Mask-less deposition of Au–SnO2 nanocomposites on CMOS MEMS platform for ethanol detection," *Nanotechnology*, vol. 27, no. 12, p. 125502, 2016, doi: 10.1088/0957-4484/27/12/125502.

[14] D. Kendig, A. Tay, and A. Shakouri, "Thermal analysis of advanced microelectronic devices using thermoreflectance thermography," in *2016 22nd International Workshop on Thermal Investigations of ICs and Systems (THERMINIC)*, 2016, pp. 115–120, doi: 10.1109/THERMINIC.2016.7749037.

[15] P. E. Raad, P. L. Komarov, and M. A. Bettiati, "Thermoreflectance measurements for optically emitting devices," in *18th International Workshop on THERMal INvestigation of ICs and Systems*, 2012, pp. 1–3.

Chapter 7

High temperature measurements on MEMS micro-heaters using thermal-incandescence microscopy:

Work will be presented in this chapter on a high temperature characterisation (to approximately 1200 °C) of the micro-electro-mechanical-systems (MEMS) micro heater used in IR thermal emitter chips, using a novel non-contact optical approach based on thermo-incandescence microscopy

7.1. Introduction:

As discussed in Chapter 6, the miniature micro-heater is embedded within a very thin semiconductor membrane (typically <10µm), and therefore it is very difficult to make the temperature measurements using contact thermal measurement techniques. The operating temperature of the miniature micro-heaters was measured to approximately 700 °C using the Quantum Focus Instrument (QFI) infra-red (IR) thermal microscope. There is a requirement to operate the IR emitter at very high temperatures (>800 °C) for spectral sensing applications in the short wave (1.4µm - 2.5µm) region of the IR spectrum where many gas molecules shows strong absorption properties [1], [2]. As part of this research work, a new temperature measurement technique was developed to enable thermal characterisation of the IR emitter chip at elevated temperatures (>700 °C) [3]. The new technique is a passive optical approach based on measuring the thermally emitted incandescent radiation as a function of operating temperature [3]. The thermal-optical calibration was achieved by utilising the known melting point (MP) of different metal microparticles. The technique potentially would enable spot measurements to be made and therefore could be used to identify hotspots.

Incandescence is the emission of the light from a hot object as a result of its high temperature (exothermic process). At elevated temperatures, the spectral distribution of thermally emitted optical radiation shifts towards shorter wavelengths (as described by Wien's law, which is explained in Chapter 3, Figure 3.3) [3], [4]. If the temperature of an object is sufficiently high, optical radiation can be visibly detected. This effect is noticeable when hot objects start to visibly glow at temperatures approaching 798 K (known as the Draper point) [5]. At lower temperatures, optical emission due to thermal-incandescence is too weak to be easily detected but thermally emitted radiation in the mid-IR waveband can be detected, for example, using IR microscopy [6]. Figure 7.1 shows the magnitude of the emitted incandescent radiance (optical wavelength of approximately 0.6 microns) of a black body significantly increases as the temperature is raised from 798 K (the Draper Point) to 1148 K.

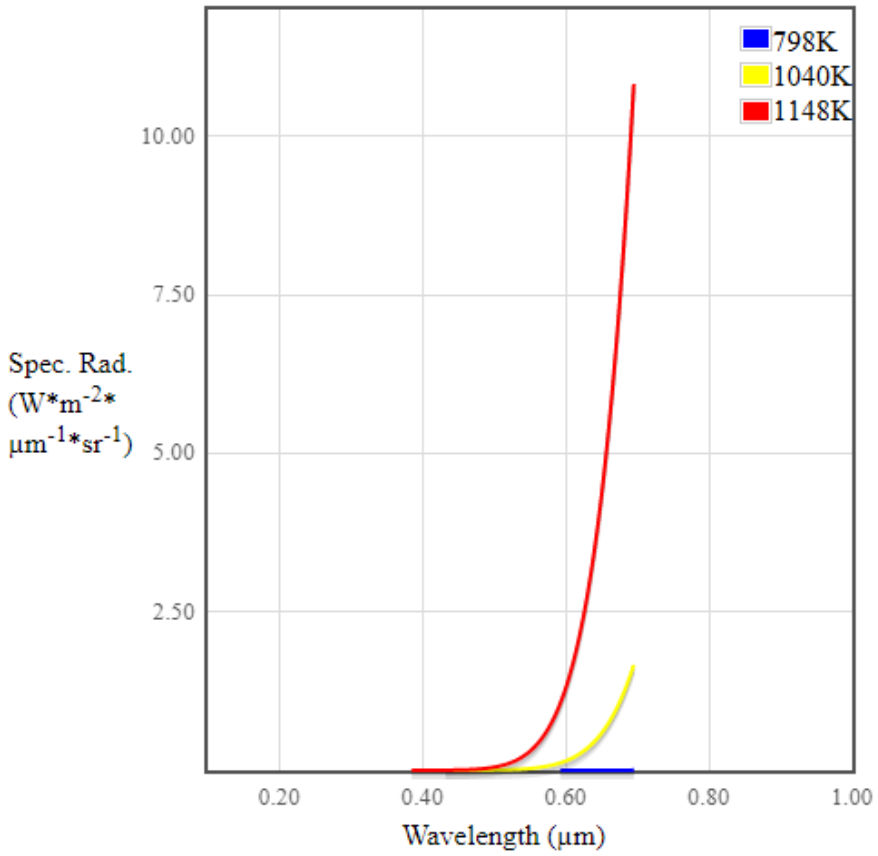

Figure 7.1: Figure showing the spectral radiance emitted by a black body at Draper point in the visible spectrum [7].

7.2. Thermo-optical measurement theory:

This section outlines the theory behind the thermo-optical measurement approach described in this research work. As discussed in Chapter 3, section **3.1.1**, the spectral radiance emitted by a black body is given by Planck's radiation law [8], which can be expressed as;

$$R_\lambda(T) = \frac{2hc^2}{\lambda^5}\left[\exp\left(\frac{hc}{\lambda\, k_B T}\right) - 1\right]^{-1} Wm^{-2}.Sr^{-1}.\mu m^{-1} \qquad \textbf{(7.1)}$$

Where, h is Planck's constant, c is speed of light in a vacuum, k_B is Boltzmann's constant, λ is the wavelength, and T is the absolute temperature of the radiating surface. The equation **(7.1)** can be simplified by introducing two constants K and K'.
If;

$$K = 2hc^2 \;\; and \;\; K' = \frac{hc}{k_B}$$

Therefore,

$$R_\lambda(T) = \frac{K}{\lambda^5}\left[\exp\left(\frac{K'}{\lambda\, T}\right) - 1\right]^{-1} \qquad \textbf{(7.2)}$$

The spectral radiance of a grey-body object will be dependent on its surface emissivity (ε) (fully described in Chapter 3). Therefore equation **(7.2)** becomes;

$$R'_{\lambda}(T) = \varepsilon(\lambda)\frac{K}{\lambda^5}\left[\exp\left(\frac{K'}{\lambda T}\right) - 1\right]^{-1} \quad \textbf{(7.3)}$$

From the equation **(7.3)** we can see that the emitted radiation is exponentially dependent on temperature T.

To measure radiation emitted by thermal incandescence, the longer wave IR contribution needs to be minimised by including an IR rejection filter. The calculation assumes the spectral response of the IR filter is $F_{IR}(\lambda)$ and the spectral response of the microscope's objective lens is, $F_{optical}(\lambda)$.

To simplify the calculation, the following assumptions can be made, at temperatures above the Draper point, the IR contribution to the radiation intensity (in 0.4μm – 0.7μm waveband) will be significantly smaller than the intensity of the optical (incandescence) radiation [8], and the surface emissivity is invariant with temperature [9].

The emitted incandescent radiation over a bandwidth (in the visible spectrum) as a function of temperature is therefore given by equation **(7.4)**;

$$R\,(T,\lambda) = \int_{\lambda_1}^{\lambda_2} R'_{\lambda}(T)\,F_{IR}(\lambda)\,F_{optical}(\lambda)\,d\lambda \quad \textbf{(7.4)}$$

Where,

$\lambda_2 - \lambda_1$ is the bandwidth of the visible spectrum.

Using equation **(7.4)**, the spectral intensity for the blue, green and red parts of the visible spectrum (spectral response of the optical camera for different regions in the optical spectrum) can be normalised and then converted to grey scale intensity as a function with temperature [10].

Assume that, the spectral response of the camera for the blue, green and red components are given as follows:

$f_B(\lambda)$ = Spectral response of the camera for blue component.

$f_G(\lambda)$ = Spectral response of the camera for green component.

$f_R(\lambda)$ = Spectral response of the camera for red component.

Therefore,

$$R_B\ (T,\lambda) = \varepsilon \int_{\lambda_1}^{\lambda_2} R'_\lambda(T)\ F_{IR}(\lambda)\, F_{optical}(\lambda)\ f_B(\lambda)\ d\lambda \quad \textbf{(7.5)}$$

$$R_G\ (T,\lambda) = \varepsilon \int_{\lambda_1}^{\lambda_2} R'_\lambda(T)\ F_{IR}(\lambda)\, F_{optical}(\lambda)\ f_G(\lambda)\ d\lambda \quad \textbf{(7.6)}$$

$$R_R\ (T,\lambda) = \varepsilon \int_{\lambda_1}^{\lambda_2} R'_\lambda(T)\ F_{IR}(\lambda)\, F_{optical}(\lambda)\ f_R(\lambda)\ d\lambda \quad \textbf{(7.7)}$$

Hence, the equations **(7.5)** to **(7.7)** can be rewritten as equations **(7.8)** to **(7.10)** respectively,

$$R_B\ (T,\lambda) = \varepsilon\ R_{B\Delta f}(T) \quad \textbf{(7.8)}$$

$$R_G\ (T,\lambda) = \varepsilon\ R_{G\Delta f}(T) \quad \textbf{(7.9)}$$

$$R_R\ (T,\lambda) = \varepsilon\ R_{R\Delta f}(T) \quad \textbf{(7.10)}$$

Each component is a function of temperature. Then, these expression can be normalised as follows;

$$\overline{R}_{B\Delta f}\ (T,\lambda) = \frac{R_{B\Delta f}\ (T)}{R_{B\Delta f}\ (T) + R_{G\Delta f}\ (T) + R_{R\Delta f}\ (T)} \quad \textbf{(7.11)}$$

$$\overline{R}_{G\Delta f}\ (T,\lambda) = \frac{R_{G\Delta f}\ (T)}{R_{B\Delta f}\ (T) + R_{G\Delta f}\ (T) + R_{R\Delta f}\ (T)} \quad \textbf{(7.12)}$$

$$\overline{R}_{R\Delta f}\ (T,\lambda) = \frac{R_{R\Delta f}\ (T)}{R_{B\Delta f}\ (T) + R_{G\Delta f}\ (T) + R_{R\Delta f}\ (T)} \quad \textbf{(7.13)}$$

The grey scale luminosity is given as, $L(T)$ [10];

$$L(T) = 0.21\, R_{R\Delta f}(T) + \ 0.72\, R_{G\Delta f}(T) + \ 0.07\, R_{B\Delta f}(T) \qquad \textbf{(7.14)}$$

Hence, the grey scale intensity, $L(T)$ is a direct function of surface temperature T

It is interesting to note the grey scale intensity is no longer a function of the surface emissivity, provided we assume the surface emissivity is independent of temperature.

7.2.1. Thermal-incandescence microscopy measurement approach:

To enable thermal-incandescence measurements in the visible spectrum the Quantum Focus Instrument (QFI) IR microscope (Infrascope-II) (introduced in Chapter 3, section **3.2.1**) was modified to include an optical camera (Stingray-F146C from Allied Vision Technologies), and an IR rejection filter (Figure 7.2). A mirror system (part of the QFI assembly) was used to switch between the IR detector and the optical camera. An optical lens was included in the lens turret, enabling switching between IR and visible objectives.

For this measurement the emitted incandescence radiation needs to be calibrated against known temperature points. To make these calibration measurements the micro-heater of the IR emitter chip (CCS113C-Chips, discussed in Chapter 6, section **6.2**) was used as a high temperature thermal platform. As mentioned, the CMOS based MEMS micro-heater is based on the tungsten metallisation technology, and is capable of operating to very high temperatures (>800 °C). The IR thermal microscopy has been used to thermally characterise the temperature distribution on the MEMS micro-heater (the results are discussed in Chapter 6), which showed excellent thermal uniformity to temperatures approaching 700 °C [6]. To substantially extend the temperature measurement range of the thermal microscope and to obtain the thermal profiles at higher operating temperatures (>800 °C), optical incandescence radiation as a function of temperature was used.

A schematic of the experimental arrangement to make the thermal-incandescence measurements on the micro-heater is shown in Figure 7.2. The IR emitter was first mounted on an aluminium base-plate (containing a calibrated K-type thermocouple), which in turn was mounted on a Peltier heater to control the base-plate temperature. The base-plate with the mounted sample was positioned underneath the objective of the IR microscope. All other supporting equipment used for incandescent temperature measurement was the same as for the IR thermal measurement technique, which was described in Chapter 3**.** The experimental setup enabled radiation from the IR emitter chip sample to be detected both in the IR and optical regions of the spectrum without any realignment of the IR emitter chip.

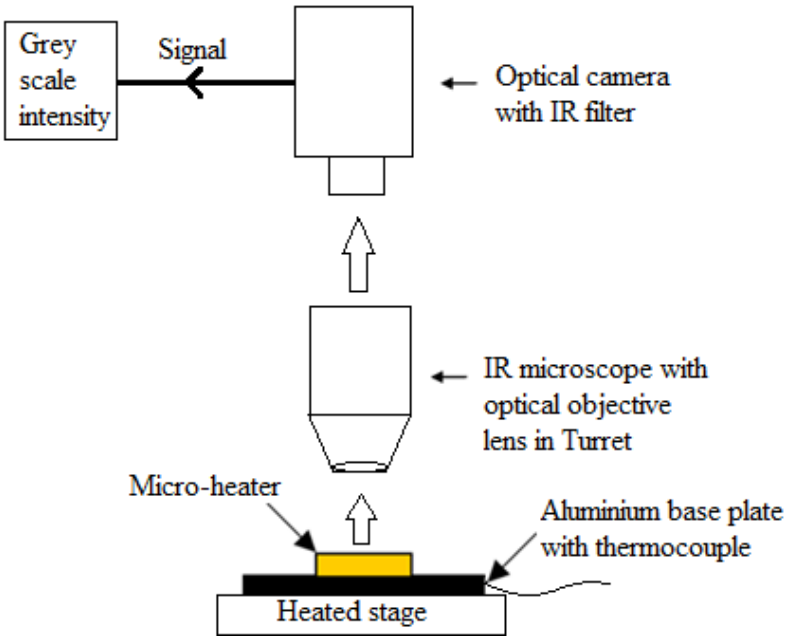

Figure 7.2: A schematic diagram showing the experimental setup used for the thermal-incandescence measurements.

To make electrical contact to the electrodes of the micro-heater, DC probes (Wentworth Laboratories PVX400) were used, which were connected to a DC power supply (TTI PL303QMD-P). The voltage applied across the micro-heater was measured using a second pair of DC micro-probes (Wentworth Laboratories PVX400). This is a 4-point probe system (discussed in Chapter 6, section **6.3.1**) and enabled more accurate measurement of the applied voltage across the heater [11]. The micro-heater was biased to DC input powers in excess of 350mW to provide heater temperatures greater than the Draper temperature. Figure 7.3 shows the incandescent radiation emitted by the micro-heater above the Draper temperature.

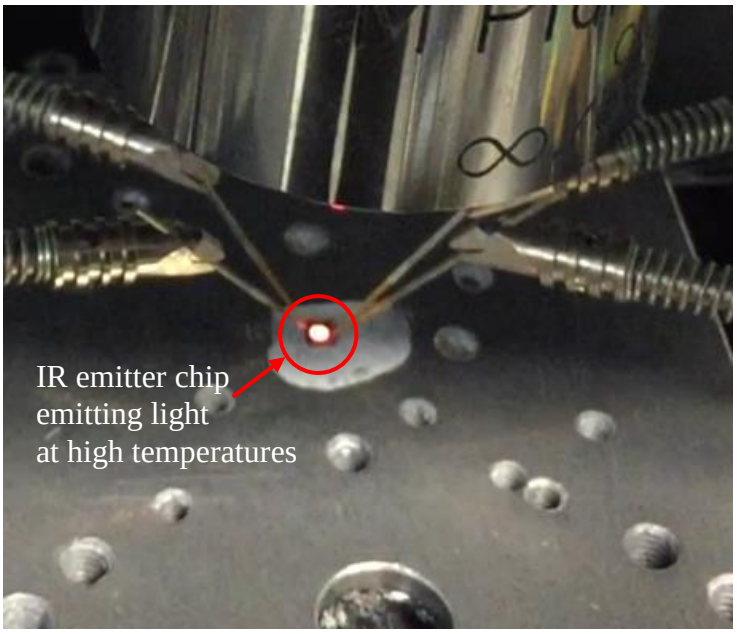

Figure 7.3: An optical image of the experimental setup showing the micro-heater of the IR emitter chip incandescing at very high operating temperatures (>700 °C).

The optical camera with an IR rejection filter was used to capture the incandescence image in the form of an 8-bit grey scale image, an example is shown in Figure 7.4. Image analysing software (known as ImageJ), which is an image processing program [12], was used to compute the intensity of optical incandescent radiation in the form of an 8-bit grey scale value in arbitrary units (a.u.).

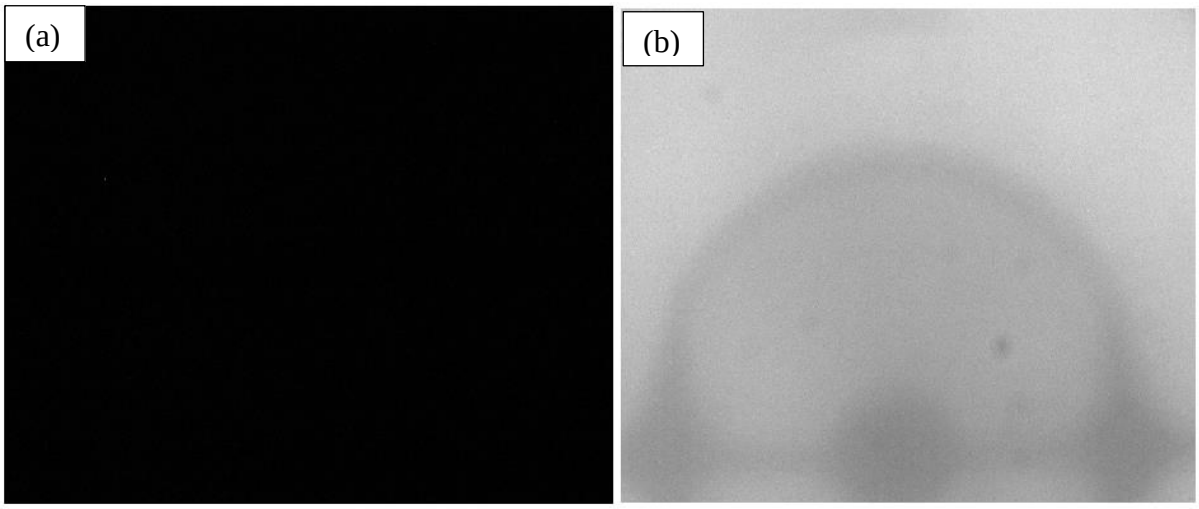

Figure 7.4: An image showing the optical incandescence radiation emitted (in the form of an 8-bit grey-scale image) from the surface of the MEMS micro-heater (a) unpowered (b) powered at ~868mW).

7.2.2. Thermal-incandescence calibration:

Initially, the thermal measurements on the MEMS micro-heater (CCS113C–Chip–D8) were obtained using the conventional IR microscope. The micro-heater was biased over a range of DC electrical powers (0 – 362mW). The DC bias of ~362mW correspond to the micro-heater being at approximately the maximum temperature, the QFI IR microscope can measure. Standard IR measurements were made (using the ×25 lens objective), and for each DC input power, a 2D thermal map of the emitter chip was generated (an example is shown in Figure 7.5). The peak temperature was identified and plotted as a function of the electrical power and shown in Figure 7.6. These measurements were made at a base-plate temperature of ~80 °C and the maximum temperature measured by the IR microscope was ~854 °C (774 °C + base-plate temperature) corresponding to an input DC electrical power of 362mW. At this temperature, the low-level of incandescent radiation intensity emitted from the surface of the micro-heater was measured by the optical camera and recorded as a greyscale value (a.u.). To obtain further thermal-incandescence calibration points, the DC input power was kept constant at 362mW, and the base-plate temperature was increased from 80 °C to 130 °C in steps of 10°C and the intensity of the incandescent radiation emitted from the surface of micro-heater was measured.

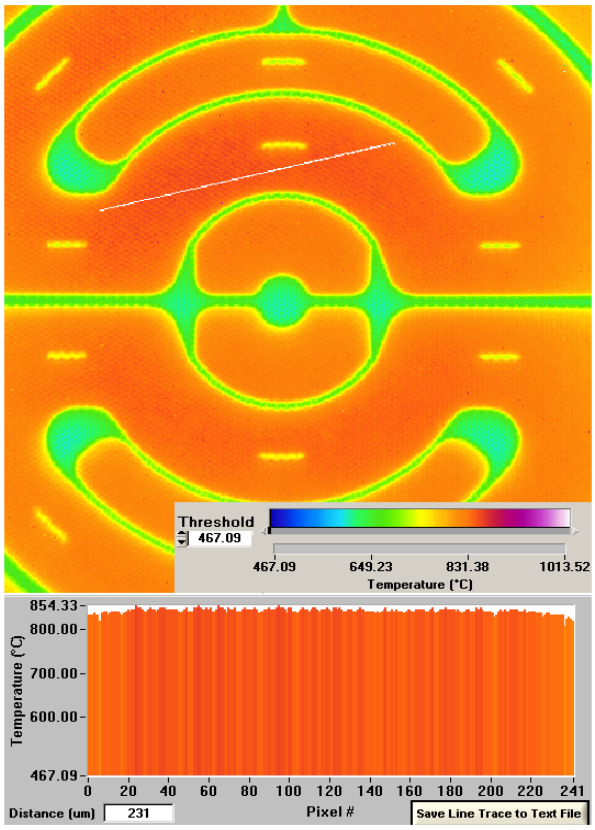

Figure 7.5: The maximum IR temperature (measured at an ambient of 80 °C using ×25 lens) recorded on micro-heater (corresponding input power was ~362.3mW). The white line in the thermal image represents the measured temperature profile location.

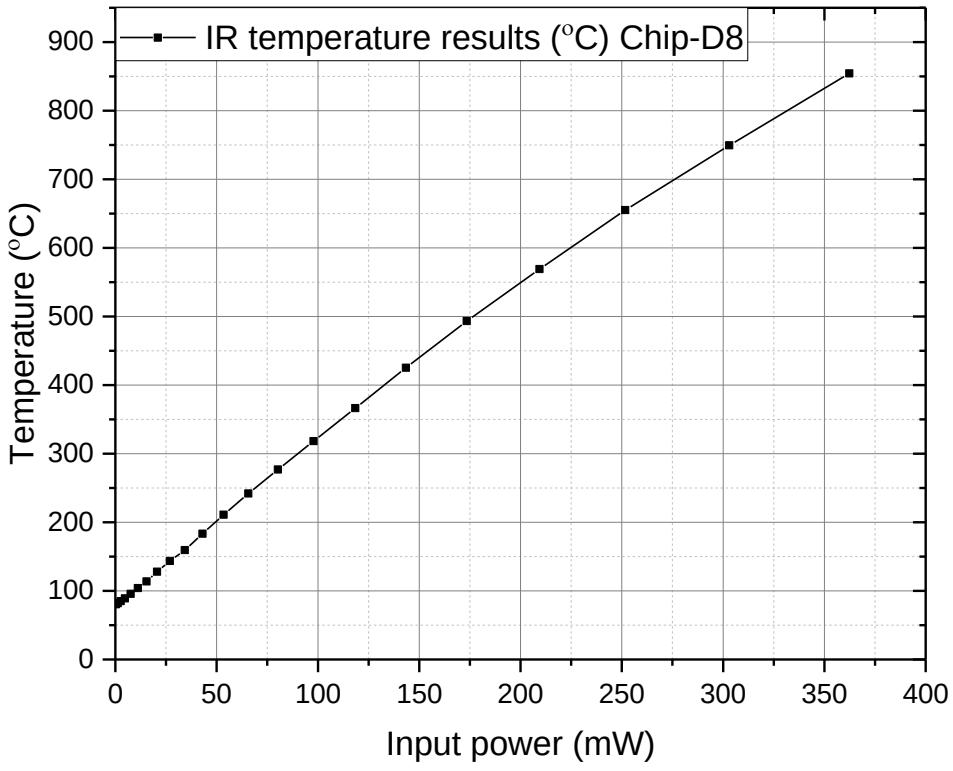

Figure 7.6: IR temperature measurement results for the micro-heater (CCS113C-Chip-D8) as a function of electrical power.

To make quantitative thermal-incandescence measurements, the optical radiation emitted from the surface of the micro-heater in the optical spectral range was calibrated as a function of temperature using different metal microparticles with known melting points. The microparticles diameters were in the range of 15µm – 20µm, and therefore small enough not to present any significant thermal loading. Table 7.1 shows a range of microparticles manufactured from different materials and their corresponding MP temperature.

Table 7.1: Different metal microparticles used for thermal-incandescence calibration with their melting points.

Microparticle	Diameter size	Melting-point temperature
Aluminium [(Al) (Sigma Aldrich, 265497)]	~15µm	660.3 °C [13]
Silver [(Ag) (Sigma Aldrich, 327107)]	~20µm	961.8 °C [14]
Copper [(Cu) (Sigma Aldrich, 326453)]	~15µm	1083.4 °C [15]
Manganese [(Mn) (Strategic Elements, 20160060)]	~15µm	1245.8 °C [13]

The metal microparticles were placed in isothermal contact with the surface of the miniature micro-heater (as shown in Figure 7.7) using a Scientifica micro-manipulation probe (the process is fully described in Chapter 4, section **4.2.1**). Naturally occurring electrostatic and Van-der-Waals forces help to adhere the metal microparticle to the micro-manipulation probe, enabling the single microparticle to be transferred to the measurement point on the surface of the micro-heater [6]. It is also possible to remove the microparticle from the surface of the device using the manipulator without causing damage to the delicate heater membrane.

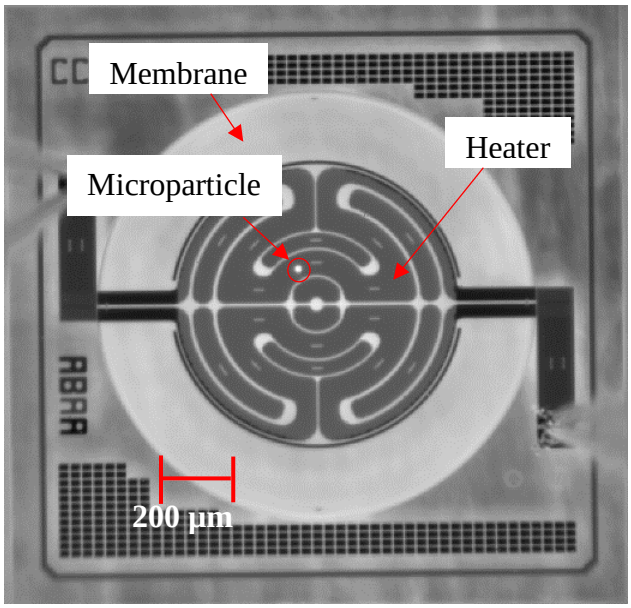

Figure 7.7: Image showing the metal microparticle placed in isothermal contact with the heater surface of the IR emitter chip.

The DC bias voltage applied to the micro-heater was slowly increased, thereby increasing the dissipated power and operating temperature, until the melting point of a metal microparticle was recorded by optically detecting the change in phase state from solid to liquid. An optical image showing the metal microparticle placed on the surface of the micro-heater membrane is shown in Figure 7.8 (a), and when the microparticle has reached the melting point is shown in Figure 7.8 (b). The intensity of optical radiation emitted from the surface of the heater due to incandescence was recorded at the melting point. This was repeated for the range of metal microparticles with different melting points to obtain a temperature calibration.

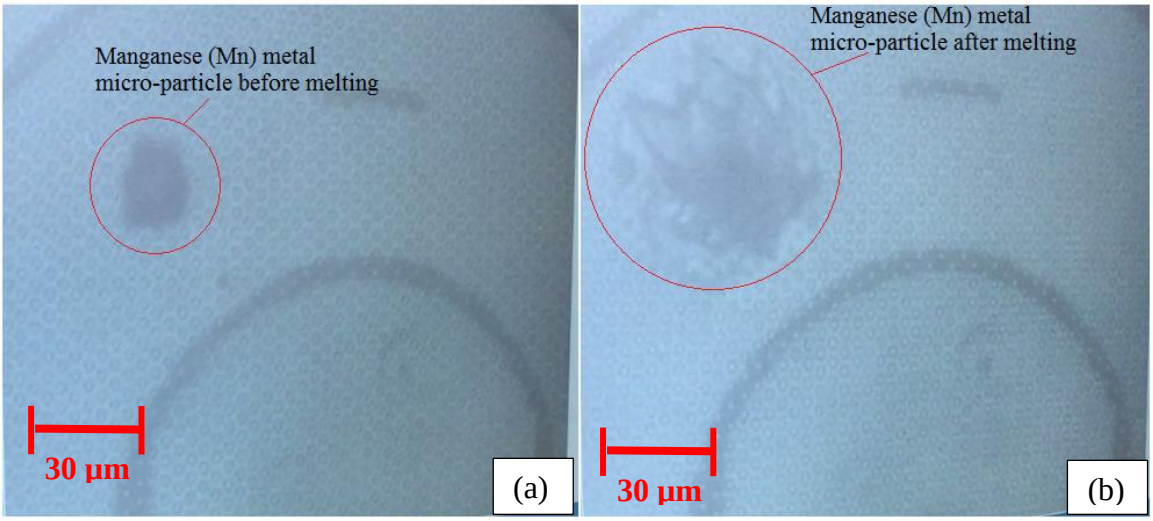

Figure 7.8: An optical image of a Mn microparticle placed on the surface of micro-heater (a) before melting and (b) after melting.

For temperatures above the Draper point the experimental points were found to be best described by an exponential curve which is shown in Figure 7.9. A summary of the experimentally measured intensity of optical emission as a function of higher temperatures is shown in Table 7.2.

Table 7.2: Optical incandescence radiation measured at the melting point of known metal microparticles.

Temperature (°C)	Optical intensity (a.u.)
660.3 (Al melting point)	1.614
854.33 (IR + base-plate temperature)	1.978
864.33	1.991
874.33	2.038
884.33	2.061
894.33	2.1
904.33	2.237
961.8 (Ag melting point)	6.683
1083.4 (Cu melting Point)	18.257
1245.8 (Mn melting point)	96.507

The exponential curve follows the intensity of incandescent radiation as a function of temperature, as described by Planck's radiation curve, and discussed in section **7.2** of this chapter. The exponential curve provides, to a first order, a calibration of incandescent radiation intensity as a function of temperature and will enable an estimation of the surface temperature of a miniature micro-heater, by measuring the intensity of the emitted optical incandescent radiation.

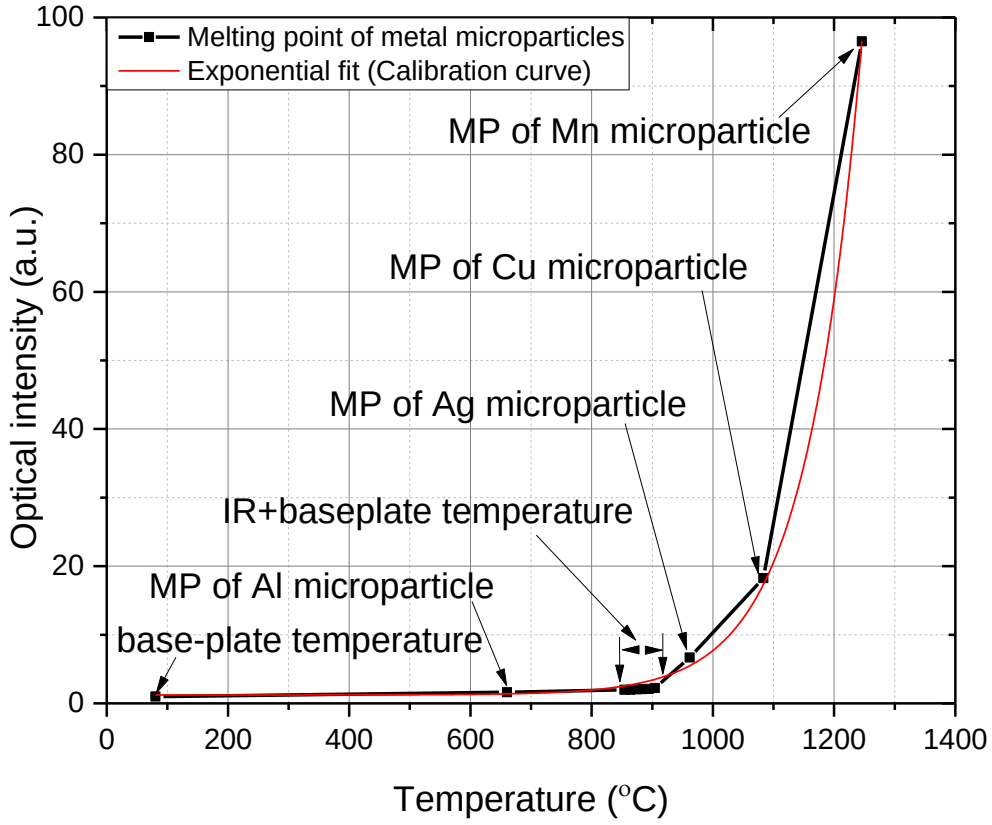

Figure 7.9: Calibration curve showing the detected incandescent radiation intensity against temperature using the melting point of metal microparticles.

7.3. Optical incandescence uniformity results:

The consistency of the magnitude of the incandescent radiation emitted by the micro-heater at high bias voltages (i.e. at high input power) was also investigated. This was undertaken by measuring the optical incandescence intensity of three IR emitter chip samples from the same fabrication batch (CCS113C-Chips). The chips were biased over an identical range of DC input powers (0 to ~760mW) and at the same ambient base-plate temperature of 80 °C. The hottest area on the miniature micro-heater was identified by conventional IR measurement and the optical camera was focused on that point. Figure 7.10 shows the intensity of optical incandescent radiation measured (a.u.) as a function of DC bias for the three devices, which all showed very similar characteristics indicating good chip-to-chip reproducibility. Therefore, it is reasonable to assume the miniature micro-heater will provide a consistent thermal platform.

However, it is interesting to note that the incandescence radiation curve does start to deviate at the very high DC input power (>800mW) (see Figure 7.10), perhaps indicating hot areas were appearing on the micro-heater, which could be future sites for device failure. Therefore, at high DC input power levels the micro-heater temperature uniformity may no longer be as consistent. At the very high DC input power levels (in excess of 800mW), where device failures occurred, the scanning electron microscope (SEM) was used to image the failure modes which will be discussed later in the chapter (section **7.5**).

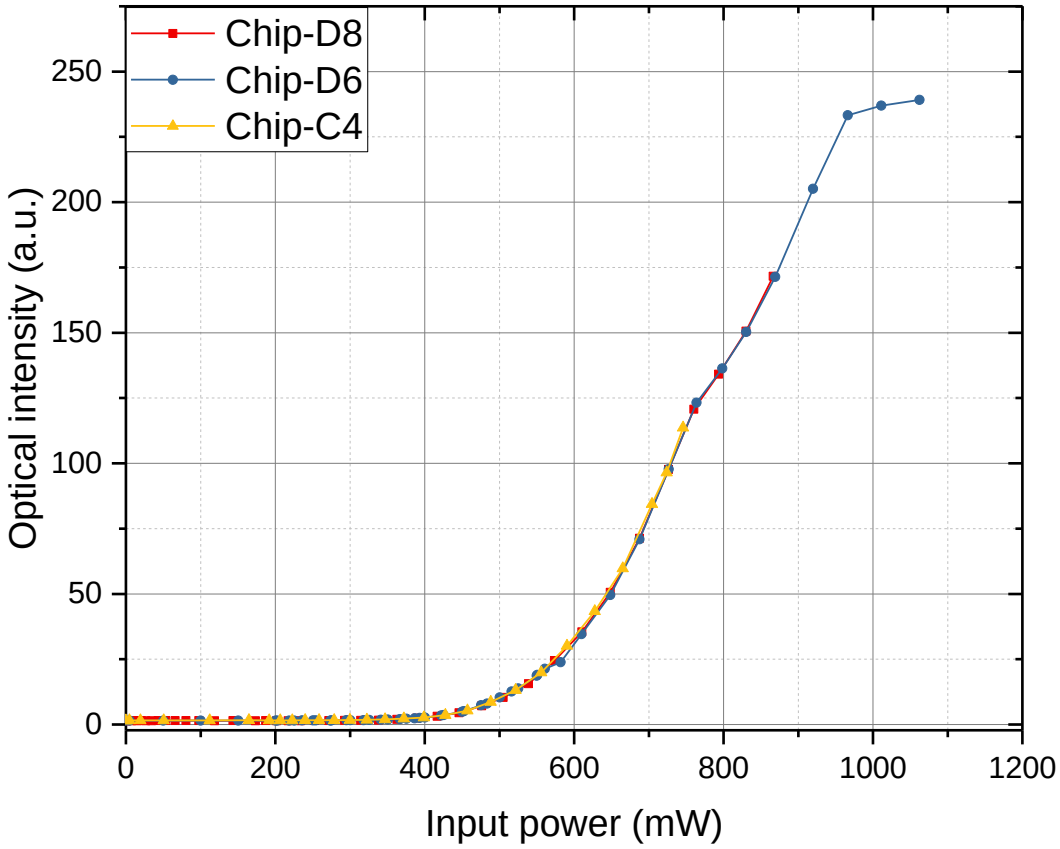

Figure 7.10: Optical incandescence results measured (a.u.) as a function of DC bias on micro-heaters (CCS113C-Chips) and measured at an ambient of 80 °C.

To further investigate the repeatability and consistency of the optical incandescent radiation emitted from the surface of different micro-heaters from the same fabrication batch (CCS113C-Chips) the experiment was repeated on a further three IR emitter chip samples but this time at different base-plate temperatures. The base-plate temperatures chosen were 25 °C and 115 °C. The incandescent radiation results which were measured as a function of input power (0 to ~560mW) and at the two base-plate temperatures are shown in Figure 7.11.

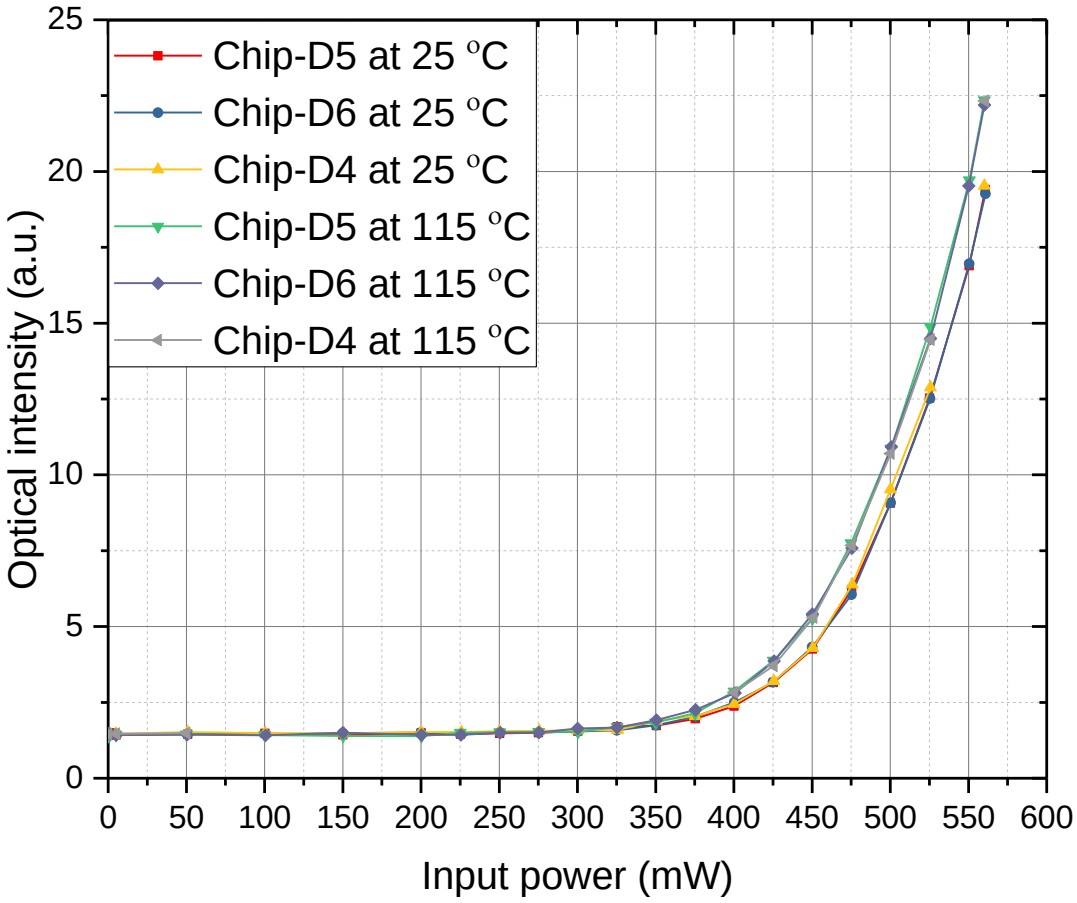

Figure 7.11: Optical incandescent radiation intensity (a.u.) measured as a function of micro-heater electrical power at two different ambient temperatures (at 25 °C and 115 °C).

The results show the optical incandescence radiation emitted from the surface of the different micro-heaters at any particular ambient base-plate temperature were very similar and consistent for different DC bias settings. This justifies the premise of using the micro-heater as a thermal platform to measure the intensity of incandescence radiation against points of calibrated temperature to give a continuous calibration curve of intensity of incandescence radiation as a function of temperature.

7.4. High temperature measurement results using thermal-incandescence method and compared with electrical temperature results:

The thermal-incandescence technique was used to estimate the surface temperature of two IR emitter chip samples (CVD-Chip-C4 and CVD-Chip-C6) biased at high DC input power levels (300mW to 727mW). These devices are similar to the micro-heater used to obtain the calibration curve (Figure 7.9) of incandescent radiation intensity as a function of temperature. For each DC input power, the optical incandescent radiation intensity was recorded, and the corresponding temperature interpolated using the calibration curve shown in Figure 7.9. The method enabled the surface temperature of the IR emitter chip to be characterised to very high temperatures, approaching 1245 °C. The experimental results are shown in Figure 7.12.

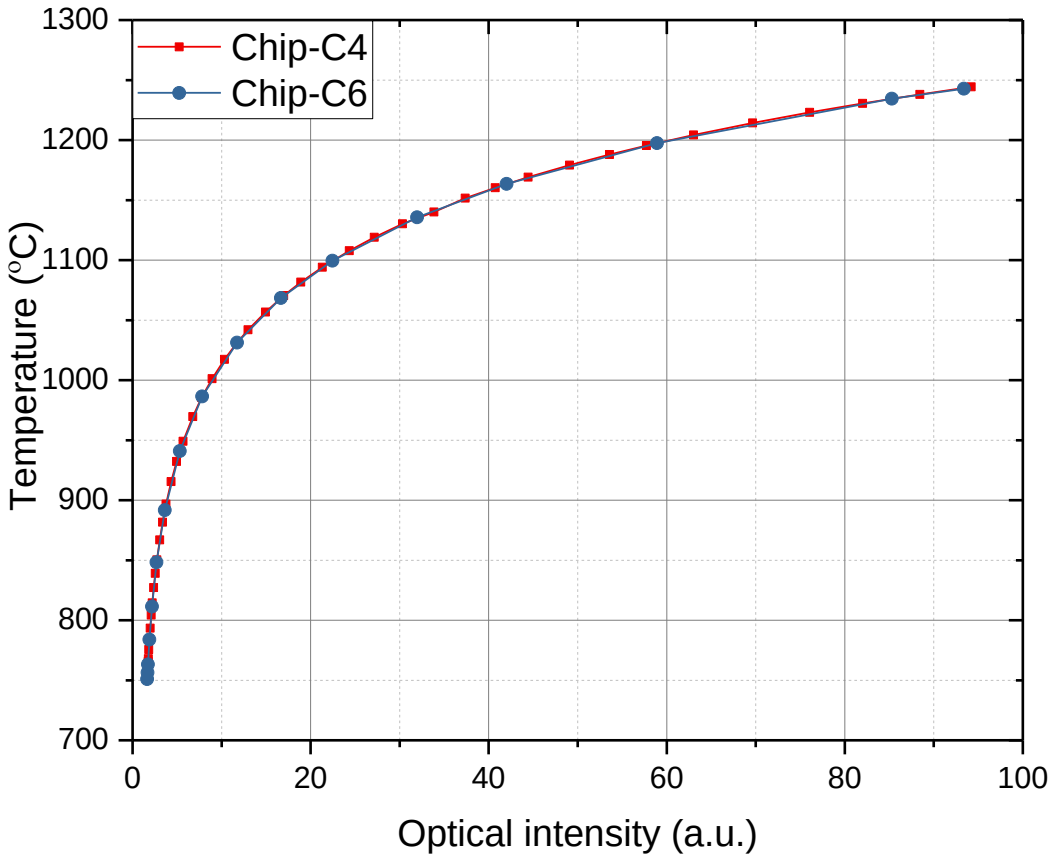

Figure 7.12: High temperature measurement results on the micro-heaters obtained from thermal-incandescence measurements and plotted as a function of incandescent radiation intensity.

The average temperature of the IR emitter chip was also calculated using an electrical method (described in section **6.4.1**, Chapter 6) [6], [16], knowing the temperature coefficients of resistance ($TCR_1 = 1.88 \times 10^{-3}$ K^{-1} and $TCR_2 = 4.6 \times 10^{-7}$ K^{-2}, provided by ams Sensors UK Ltd.).

The IR emitter chip average temperature determined using the electrical method (as a function of DC input power), was compared with temperature measurements obtained by conventional IR measurement for low DC input powers (up to 300mW) and with the temperatures obtained by the optical incandescence approach for high DC input powers (>300mW). The comparison is shown in Figure 7.13. A maximum surface temperature of ~1245 °C was recorded at an input power of 735mW. There was reasonable agreement between the temperature results of the optical and electrical methods (within a ± 3.5 % margin of error), as a function of DC input power to the IR emitter chip. The electrical method provides the lumped average surface temperature of the IR micro-heaters and as there was good agreement with the IR and optical incandescence spot measurements, it was concluded there was good uniformity of temperature across the surface of the micro-heater.

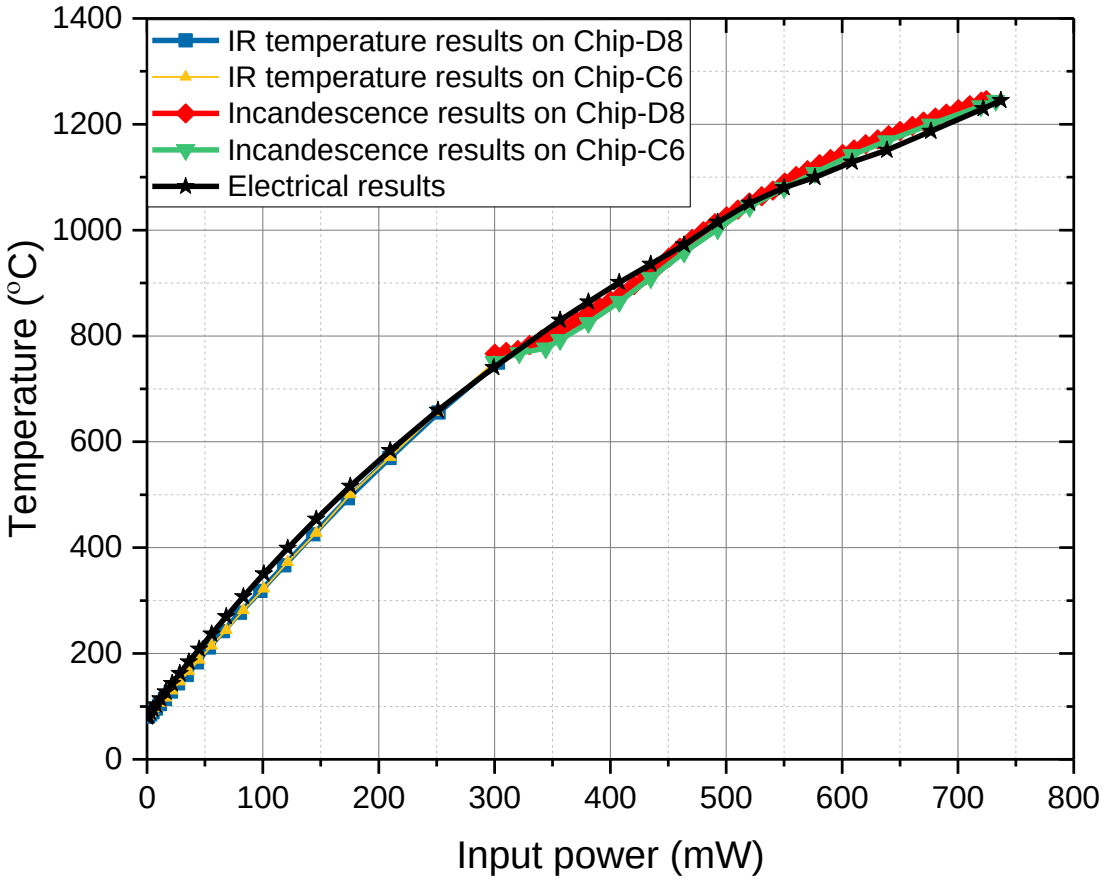

Figure 7.13: Comparison between conventional IR, incandescence and electrical temperature measurement results.

7.5. High power electrical characterisation and failure analysis:

The high power (>800mW) electrical characterisation (IV measurements) were made on two IR emitter chip samples from the same fabrication batch (CCS113C-Chips) to investigate the device failure point. This was done by using the 4-probe IV measurement system (as discussed in Chapter 6, section **6.3.1**) to measure the IV characteristics to the point where the device failed or burnt-out (see Figure 7.14). The device burnt-out at a DC input power of approximately 1035mW. The occurrence of the burn-out always occurred after there was a noticeably glitch in the IV characteristics, see Figure 7.14. The IV measurement was made at a base-plate temperature of ~80 °C.

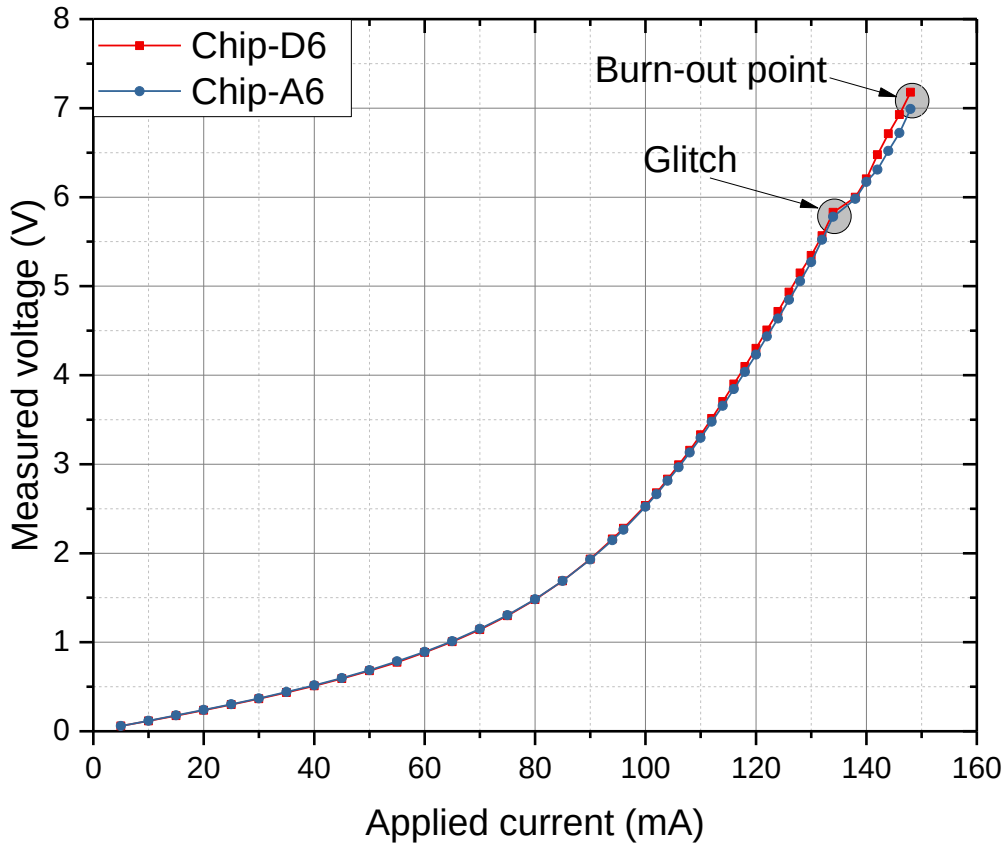

Figure 7.14: High power electrical characterisation on the IR emitter chips (CCS113C-Chips) and failure analysis.

The results in Figure 7.14 show the IV characteristics of the two devices were very similar where the operating voltage uniformly increased as the current was increased until the device reached a DC input power of ~800mW. At this point the IV curves started to deviate indicating the device failure, and the micro-heater membrane of the IR emitter chips burnt-out at DC input power level of ~1035mW. The high electrical DC input power to the micro-heater indicates the device maximum operating temperature has to be under 1300 °C to ensure the device is not burnt-out.

Scanning electron microscope (SEM-Leica S430) was used for imaging the burnt-out devices and it was found for both devices the micro-heater membrane had failed. The SEM images of the failed IR emitter chips are shown in Figure 7.15 and Figure 7.16.

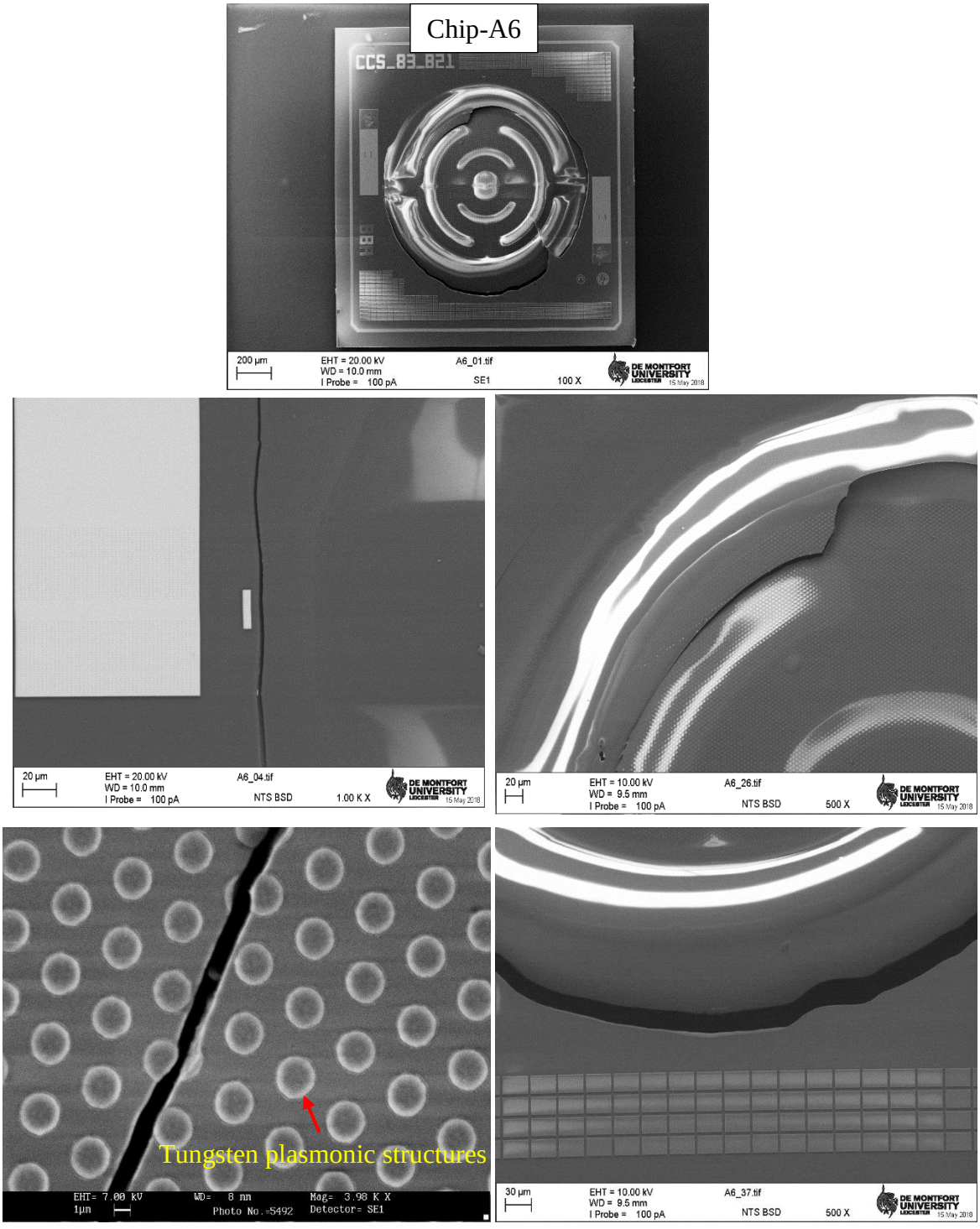

Figure 7.15: SEM images of the failed IR emitter chip (CCS113C-Chip-A6) showing the broken micro-heater membrane.

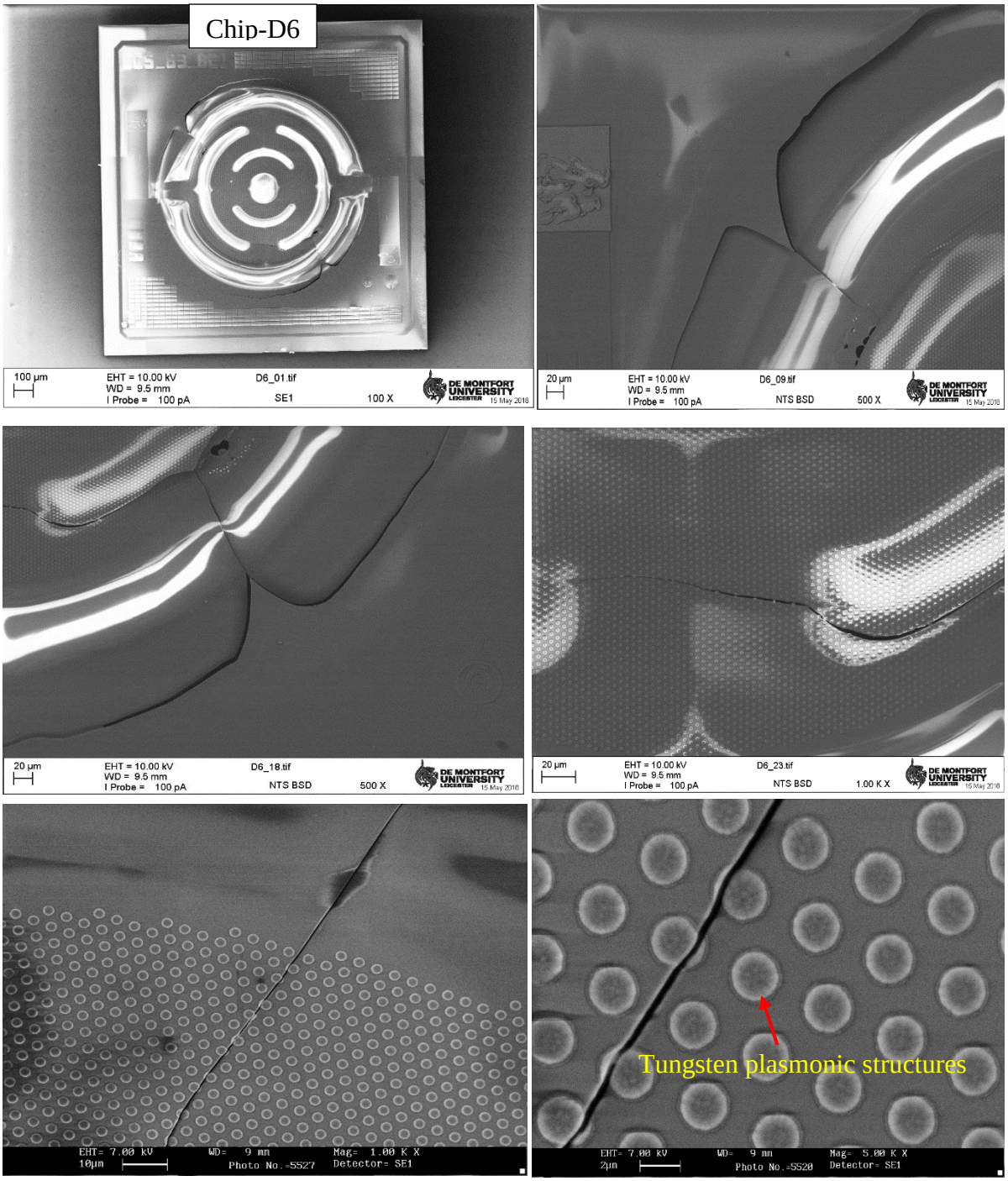

Figure 7.16: SEM images of the failed IR emitter chip (CCS113C-Chip-D6) showing the broken micro-heater membrane.

7.6. Conclusion:

High temperature thermal characterisation of MEMS IR micro-emitter chips, fabricated on a SiO_2 membrane using tungsten metallisation, has been undertaken for the first time using a combination of IR microscopy and thermal-incandescence microscopy. Conventional IR imaging was used to thermally characterise the micro-heater embedded in the IR emitter chip to temperatures ~700 °C and optical incandescence to elevated temperature in excess of 1200°C. The known melting points of metal microparticles were used to calibrate the thermal-incandescence radiation intensity as a function of temperature.

The temperature results obtained from the thermo-optical measurements, were compared to those obtained using an electrical method. There was reasonable (max error ± 3.5 %) agreement between the optical and electrical temperature measurements suggesting uniformity of temperature across the micro-heater of the IR emitter chip to a maximum temperature of approximately 1245 °C (to the equivalent DC input power of 735mW).

The thermal-incandescence microscopy measurement technique shows potential for increasing the temperature range of an IR microscope by integrating an optical camera for high temperature characterisation of electronic devices.

High power IV measurements (in excess of 1000mW) were also made on the IR micro emitter chips to investigate the device failure point. The high DC input electrical power results showed the MEMS micro-heater failed at around ~800mW (glitch in the IV characteristics) indicating the maximum safe operating temperature of the device is less than ~1300 °C. Further increase in the DC input power (approx. 1035mW) resulted in the device being burnt out which was attributed by SEM analysis to the failure of the micro-heater membrane.

7.7. References:

[1] I. E. Gordon *et al.*, "The HITRAN2016 molecular spectroscopic database," *Journal of Quantitative Spectroscopy and Radiative Transfer*, vol. 203, pp. 3–69, Dec. 2017, doi: 10.1016/j.jqsrt.2017.06.038.

[2] M. Yu, Y. Okawachi, A. G. Griffith, N. Picqué, M. Lipson, and A. L. Gaeta, "Silicon-chip-based mid-infrared dual-comb spectroscopy," *Nature Communications*, vol. 9, no. 1, p. 1869, May 2018, doi: 10.1038/s41467-018-04350-1.

[3] P. Pandey, C. Oxley, R. H. Hopper, F. Udrea, and S. Z. Ali, "High temperature characterization of a CMOS based infra-red source using thermal-incandescence microscopy," *Solid-State Electronics*, vol. 166, p. 107773, Apr. 2020, doi: 10.1016/j.sse.2020.107773.

[4] A. E. Dubinov and I. N. Kitaev, "Generalized Wien's displacement law and Stefan-Boltzmann law for thermal radiation with a nonzero chemical potential," *J. Opt. Technol., JOT*, vol. 85, no. 6, pp. 314–316, Jun. 2018, doi: 10.1364/JOT.85.000314.

[5] J. R. Mahan, *Radiation Heat Transfer: A Statistical Approach*. New York: John Wiley & Sons, 2002.

[6] P. Pandey, C. Oxley, R. Hopper, Z. Ali, and A. Duffy, "Infra-red thermal measurement on a low-power infra-red emitter in CMOS technology," *IET Science, Measurement & Technology*, vol. 13, no. 1, pp. 25–28, Aug. 2018, doi: 10.1049/iet-smt.2018.5427.

[7] "Radiance Calculator," *NASA Astrology Science Centre*. [Online]. Available: https://astrogeology.usgs.gov/tools/thermal-radiance-calculator/. [Accessed: 22-Nov-2018].

[8] J. R. Howell, M. P. Menguc, and R. Siegel, *Thermal radiation heat transfer*, Sixth edition. New York: CRC press, 2015.

[9] E. Brodu, M. Balat-Pichelin, J.-L. Sans, and J. C. Kasper, "Evolution of the emissivity of tungsten at high temperature with and without proton bombardment," *Acta Materialia*, vol. 84, pp. 305–316, Feb. 2015, doi: 10.1016/j.actamat.2014.10.050.

[10] R. C. González and R. E. Woods, *Digital Image Processing*, Third Edition. New Jersey: Pearson Education, Inc, 2008.

[11] J. Glover, "The design and thermal measurement of III-V integrated micro-coolers for thermal management of microwave devices," Ph.D., De Montfort University, 2016.

[12] C. T. Rueden *et al.*, "ImageJ2: ImageJ for the next generation of scientific image data," *BMC Bioinformatics*, vol. 18, no. 1, p. 529, Nov. 2017, doi: 10.1186/s12859-017-1934-z.

[13] "Metals and Alloys-Melting Temperatures," *The Engineering ToolBox*. [Online]. Available: https://www.engineeringtoolbox.com/melting-temperature-metals-d_860.html. [Accessed: 11-Dec-2018].

[14] "Silver - Melting Point - Boiling Point," *Nuclear Power*, 17-May-2018. [Online]. Available: https://www.nuclear-power.net/silver-melting-point-boiling-point/. [Accessed: 11-Dec-2018].

[15] "Copper GF52483664," *Sigma-Aldrich: Analytical, Biology, Chemistry & Materials*. [Online]. Available: https://www.sigmaaldrich.com/catalog/product/aldrich/gf52483664. [Accessed: 11-Dec-2018].

[16] S. Z. Ali, "Electro-thermo-mechanical study of membrane devices for smart IC technologies," Ph.D., University of Cambridge, 2008.

Chapter 8

Conclusions and Future work:

8.1. Conclusions:

Gas sensors are becoming an integral part of our everyday lives for applications in various fields, such as agriculture (e.g., monitoring methane emission from agricultural dairy farming) [1], [2], industrial, medical, scientific [3], automotive, domestic, and environmental monitoring [4], [5]. Micro-Electro-Mechanical Systems (MEMS) technology is crucial to the design and fabrication of miniaturised gas sensors offering low power consumption, low cost, high sensitivity and high selectivity. The MEMS micro-heater is a key element for most of the modern gas sensors [6] and a promising technology for a number of other applications. Knowledge about the thermal uniformity and accurate maximum operating temperature of the micro-heater is crucial to investigate the sensing performance and reliability of these gas sensing devices. This research has described high temperature thermal characterisation of novel micro-heaters used in infra-red (IR) micro-emitter chips (for gas sensing applications), based on tungsten CMOS technology [7].

8.1.1. Infra-red thermal measurements:

IR thermal microscopy has been widely used to characterise the thermal behaviour of micro-scale biased electronic devices, because it offers major benefits including non-contact and non-invasive measurements. It utilises naturally emitted IR radiation from the surface of the sample, resulting in a real-time two-dimensional (2D) thermal images [7]. The technique has been shown to be a useful tool for high temperature thermal characterisation (to temperatures approaching 700 °C) of MEMS based IR emitter chips, which were fabricated using tungsten CMOS technology, as discussed in Chapter 6.

The research in this thesis has reported the use of IR microscopy to form 2D real-time thermal maps of miniature micro-heaters, primarily for IR micro-emitter chips for use in mid-IR spectroscopy applications including non-dispersive IR (NDIR) gas sensing (as discussed in Chapter 5, section **5.3.3**). The thermal maps have been used to understand information regarding the safe operating power limits, temperature uniformity across the micro-heater and to identify hotspots. It is important to assess the thermal uniformity across the micro-heater to ensure consistent IR emission and to minimise the localised hotspots, which could induce thermal stress leading to premature failure of the devices. The IR measured temperature profiles of the IR emitter chip showed the micro-heater had good thermal uniformity, with a maximum temperature variation across the heater surface of ~3%. This was further emphasised as the conventional IR measurements were in reasonable agreement with calculated electrical average temperature results in which the coefficients of resistance as a function of temperature of the micro-heater were used.

A factor limiting the accuracy of temperature measurements using conventional IR thermal microscopy is, uncertainty in the determination of the surface emissivity of the device being measured. This is mainly a concern for measurements made on low emissivity, and

optically transparent semiconductor materials, which allow the IR radiation from the subsurface layers to be collected by the microscope, leading to errors in measuring the surface emissivity. To overcome this limitation, a novel technique has been developed that employs a carbon based microparticle infra-red sensor (MPIRS) with a known, and high, surface emissivity [8]. The technique eliminates the need for a conventional high emissivity coating of black paint, which can average the temperature of hotspots across the surface (heat spreading) and can damage the device. Throughout this research further understanding has contributed to the novel MPIRS measurement technique, utilising IR thermal microscopy, and was discussed in Chapter 4 and Chapter 6. These contributions include showing a glass substrate is a convenient surface to pick a single MPIRS using the manipulation probe (also made of glass) and then effectively transfer it to the point on the surface of the device under test (DUT) where the temperature is to be measured (Chapter 4). In addition, it was shown the background material surface emissivity will have an effect on the emitted radiance of the MPIRS, which is also a function of temperature. The work indicated that the MPIRS technique would be best adopted on materials with very low emissivity (for example gold) where the surface background radiation is a minimum. To make temperature measurements on semiconductor materials (for example, Si & GaAs) which are transparent to IR radiation, the actual surface emissivity value of the MPIRS needs to be established first (at least $\geq$0.6 as suggested in Chapter 4). A revised base-plate heater technique was developed, and for the first time the MPIRS radiance has been measured as a function of temperature to high operating temperatures (>300 °C). For these measurements the MPIRS was placed on a polished surface enabling a more accurate estimate of its surface emissivity to temperatures approaching 300 °C, by subtracting the residue background surface radiance from the total measured radiance.

The research has reported the use of the MPIRS for IR thermal microscopy measurement, can reduce the uncertainties in the temperature measurement of samples with poor surface emissivity. The MPIRS technique has been used for improved high temperature thermal profiling of the MEMS micro-heaters to temperatures approaching 700 °C. Additionally, the first use of a single MPIRS for improved IR surface temperature measurements on MEMS micro-heater (with very low surface emissivity, <0.1) fabricated on semi-packaging geometry has also been demonstrated. The emitted radiance for sub-10µm diameter particles was shown to be lower than for larger particles, for example 20µm diameter (Chapter 4), and therefore can lead to an error in the temperature measurements. The effect of the MPIRS diameter size has on the IR temperature measurements was investigated. The results showed that the measured temperature profile using smaller particles (for example 3µm diameter) will underestimate the surface temperature by approximately 5% compared to temperature measurements made using larger size microparticles (15µm, 21µm or 43µm). The larger diameter particles were shown to give very similar measured temperature values. Therefore, the research suggests the MPIRS of diameter size (> 10µm) should be used to obtain more accurate temperature profiles on low emissivity devices.

8.1.2. Thermo-incandescence measurements:

The CMOS based IR emitter chip is required to operate to temperatures in excess of 800 °C for spectral sensing applications in the short-wave region of the IR spectrum (1.4µm – 2.5µm) where many molecules have their absorption lines [9]. In this research work, a novel thermal measurement approach for high temperature characterisation (>800 °C) on electronic devices, using optical incandescence radiation thermography was demonstrated [10]. For this method, the QFI IR microscope facility at DMU was modified to include an optical camera, fitted with an IR rejection filter. The miniature micro-heater based on tungsten metallisation technology which was capable of operating to very high temperatures was shown to provide a consistent incandescence radiation and therefore could be successfully used as a thermal platform. To obtain the thermal profile at elevated temperatures (>800 °C), the intensity of the optical incandesce radiation as a function of operating temperature was used. Thermal-optical calibration was achieved by utilising the known melting point (MP) of different metal microparticles.

The method has been used for the high temperature characterisation of the MEMS micro-heaters to approximately 1245 °C [10]. The estimated surface temperature obtained from the thermo-incandescence measurements were compared with the temperature results determined using electrical method. There was reasonable agreement between the optical and electrical temperature measurements (max error ± 3.5%) suggesting high temperature uniformity across the micro-heater of the IR emitter chip. The measurement technique can be utilised for increasing the temperature measurement range of an IR microscope by integrating an optical camera for high temperature characterisation of electronic devices.

8.2. Future work:

Many areas of this research work could be expanded into further research programmes to improve the accuracy of temperature measurements using infra-red and thermal-incandescence microscopy. As discussed, the spatial thermal resolution of IR microscopy is dependent on the wavelength and therefore cannot be improved much further than approximately 2 microns. However, the thermal spatial resolution of the thermal-incandescence microscopy has not been explored in this research. Other areas of continued research are;

- The accuracy of the temperature measurements using the IR microscopy could be further improved by developing new methods of measuring or computing the surface emissivity of the device under test (DUT). This research work has shown the potential of using a MPIRS to obtain improved surface emissivity measurement on DUT. However, more work is required to calibrate the MPIRS surface emissivity more accurately, particularly taking into account the background radiation and the diameter of the MPIRS.

- In this research work, the MPIRS radiance was calibrated to higher temperatures approaching 300 °C when it was placed on a uniform known low emissivity surface. In this approach the radiance emitted by the background could be taken into account when

calculating the surface emissivity of the MPIRS. This is often an unreal situation and further work is required to develop of an algorithm which would take into account the background radiation for different background surfaces where the MPIRS may be placed on. This research work also suggests the MPIRS may have a limiting diameter of 10µm which would reduce the thermal spatial resolution of the MPIRS measurement technique. This certainly requires further investigation and research.

- The manipulation of the MPIRS requires further work. A single MPIRS which can be easily and quickly manipulated across the surface of DUT would improve the accuracy of temperature profiling across the metal and semiconductor surfaces of a device. This will require to develop a more precise and reliable single microparticle computer stepped manipulation process, which include more precise control of the electrostatic force between the microparticle and manipulation probe tip. It would then be possible to release and/or reposition of a microparticle sensor without the risk of manipulation probe touching the surface of delicate devices and also not requiring the removal of the bias probes.

- To further develop the MPIRS technique for measuring the temperature of packaged devices in particular the temperature of bond wires which are often high grade gold with a low surface emissivity.

- Part of this research work was to investigate the temperature uniformity and maximum operating temperature of the MEMS micro-heaters which can be used as the mid and short-wave IR sources, for use in non-dispersive infra-red (NDIR) gas sensing and absorption spectroscopy applications. This could be a large topic for future development of smart gas sensors with a range of application in medicine, personnel detection of gas agents using mobile phones etc. This will require the integration of the MEMS micro-heaters with other technologies, and the construction of the MEMS micro-heater to operate at very high temperature greater than 1200 °C. The high temperatures will require new thermal measurement techniques, not only to measure the temperature accurately, but also to determine the uniformity across the surface of the micro-heater.

This research has opened a new approach for measuring high temperatures by integrating IR and optical incandescent thermal microscopy. The work has shown it is possible to measure seamlessly over a temperature range from approximately from 40 °C to 1200 °C. The optical incandescent measurement technique with further development may show potential of high thermal spatial resolution, enabling the identification of hotspots which could be potential failure points when the heater is operated to temperatures in excess of 1000 °C.

8.3. References:

[1] "Monitoring Methane Emissions from Agriculture and Dairy Farming," *AWE International*, 02-Feb-2017. [Online]. Available: https://www.aweimagazine.com/press-release/monitoring-methane-emissions-from-agriculture-and-dairy-farming/. [Accessed: 13-Jan-2020].

[2] A. Ghosh, C. Zhang, S. Q. Shi, and H. Zhang, "High-Temperature Gas Sensors for Harsh Environment Applications: A Review," *CLEAN-Soil, air, water*, vol. 47, no. 9, Sep. 2019, doi: 10.1002/clen.201800491.

[3] J. P. Dakin and P. Chambers, "Review of Methods of Optical Gas Detection by Direct Optical Spectroscopy, with Emphasis on Correlation Spectroscopy," in *Optical Chemical Sensors*, 2006, pp. 457–477.

[4] K. Wetchakun *et al.*, "Semiconducting metal oxides as sensors for environmentally hazardous gases," *Sensors and Actuators B: Chemical*, vol. 160, no. 1, pp. 580–591, Dec. 2011, doi: 10.1016/j.snb.2011.08.032.

[5] H. Liu, L. Zhang, K. H. H. Li, and O. K. Tan, "Microhotplates for Metal Oxide Semiconductor Gas Sensor Applications—Towards the CMOS-MEMS Monolithic Approach," *Micromachines*, vol. 9, no. 11, p. 557, Nov. 2018, doi: 10.3390/mi9110557.

[6] W.-J. Hwang, K.-S. Shin, J.-H. Roh, D.-S. Lee, and S.-H. Choa, "Development of Micro-Heaters with Optimized Temperature Compensation Design for Gas Sensors," *Sensors*, vol. 11, no. 3, pp. 2580–2591, Mar. 2011, doi: 10.3390/s110302580.

[7] P. Pandey, C. Oxley, R. Hopper, Z. Ali, and A. Duffy, "Infra-red thermal measurement on a low-power infra-red emitter in CMOS technology," *IET Science, Measurement & Technology*, vol. 13, no. 1, pp. 25–28, Aug. 2018, doi: 10.1049/iet-smt.2018.5427.

[8] R. Hopper, D. Prime, G. Evans, K. Lee, and C. Oxley, "Improved infrared temperature measurement of RF devices," 2013, Accessed: Aug. 29, 2018. [Online]. Available: http://www.armms.org/media/uploads/1326110849.pdf.

[9] M. Yu, Y. Okawachi, A. G. Griffith, N. Picqué, M. Lipson, and A. L. Gaeta, "Silicon-chip-based mid-infrared dual-comb spectroscopy," *Nature Communications*, vol. 9, no. 1, p. 1869, May 2018, doi: 10.1038/s41467-018-04350-1.

[10] P. Pandey, C. Oxley, R. H. Hopper, F. Udrea, and S. Z. Ali, "High temperature characterization of a CMOS based infra-red source using thermal-incandescence microscopy," *Solid-State Electronics*, vol. 166, p. 107773, Apr. 2020, doi: 10.1016/j.sse.2020.107773.

APPENDIX – 4A

Table: 8.1: Emissivity measurement results (two-temperature emissivity) on a black tape measured using ×25 lens.

Temperature range (ºC)	Emissivity (ε)	
	Aluminium background	Black tape background
R_a = 70 ºC and R_b = 100 ºC	0.97	1.19
R_a = 75 ºC and R_b = 105 ºC	0.94	1.17
R_a = 80 ºC and R_b = 110 ºC	0.96	1.13
R_a = 85 ºC and R_b = 115 ºC	0.94	1.14
R_a = 90 ºC and R_b = 120 ºC	0.95	1.15
Average	**0.952**	1.16

APPENDIX – 4B

Table: 8.2: Comparison between the temperature results measured using MPIRS when deposited on aluminium base-plate and using thermocouple.

Temperature (°C)	
Thermocouple results	Carbon MPIRS sensor results
49.9	49.6
59.9	59.92
70	69.83
80.1	80.1
90	90.02
100	100
109.9	109.93
120	120.4
130	130.1

APPENDIX – 4C

Table: 8.3: IR radiance level measured from the surface of MPIRS at high temperatures.

Temperature (°C)	MPIRS - 1 (size ~ 20 µm) radiance ($mw/cm^2.str$)	MPIRS - 2 (size ~21µm) radiance ($mw/cm^2.str$)	MPIRS - 3 (size ~20µm) radiance ($mw/cm^2.str$)	MPIRS - 4 (size ~23µm) radiance ($mw/cm^2.str$)
140	2.026	2.01	2.001	2.057
150	2.535	2.522	2.54	2.593
160	3.148	3.151	3.154	3.276
170	3.93	3.919	3.934	4.057
180	4.779	4.853	4.853	4.919
190	5.858	5.867	5.94	6.111
200	7.214	7.115	7.108	7.264
210	8.637	8.683	8.577	8.872
220	10.293	10.144	10.214	10.5
230	12.164	12.09	11.935	12.162
240	14.101	13.849	14.144	14.343
250	16.226	16.173	16.495	17
260	18.955	19.017	19.201	19.43
270	21.743	21.816	22.218	22.4
280	25.091	24.874	25.207	25.676
290	29.032	28.83	29.036	29.396
300	32.522	32.333	32.696	33.473
310	37.119	36.846	37.27	38.1

APPENDIX – 6A

Table 8.1: Initial IV characteristics of an untested IR micro-emitter (device CCS113C-chip-C7).

Power (mW)	**Applied current (mA)**	**Measured voltage (V)**	**Wait Time**
514.2	120mA	4.285V	*0 min*
510.24	120mA	4.252V	*after 1 min,*
511.7	120.4mA	4.250V	*after 2 min,*
513.34	120.9mA	4.246V	*after 5 min,*
517.696	122.3mA	4.233V	*after 15 min,*
518.721	122.6mA	4.231V	*after 20 min,*
519.02	122.7mA	4.230V	*after 25 min,*
519.32	122.8mA	4.229V	*after 30 min,*
519.32	122.8mA	4.229V	*after 35 min,*